Spoof surface plasmon photonics

Francisco J. Garcia-Vidal[*]

Departamento de Física Teórica de la Materia Condensada and Condensed Matter Physics Center (IFIMAC), Universidad Autónoma de Madrid, Madrid 28049, Spain and Donostia International Physics Center (DIPC), Donostia/San Sebastián 20018, Spain

Antonio I. Fernández-Domínguez

Departamento de Física Teórica de la Materia Condensada and Condensed Matter Physics Center (IFIMAC), Universidad Autónoma de Madrid, Madrid 28049, Spain

Luis Martin-Moreno

Instituto de Nanociencia y Materiales de Aragón (INMA), CSIC-Universidad de Zaragoza, Zaragoza 50009, Spain and Departamento de Física de la Materia Condensada, Universidad de Zaragoza, Zaragoza 50009, Spain

Hao Chi Zhang and Wenxuan Tang

State Key Laboratory of Millimeter Waves, Southeast University, Nanjing 210096, China

Ruwen Peng

National Laboratory of Solid State Microstructures, School of Physics, and Collaborative Innovation Center of Advanced Microstructures, Nanjing University, Nanjing 210093, China

Tie Jun Cui[†]

State Key Laboratory of Millimeter Waves, Southeast University, Nanjing 210096, China

(published 20 May 2022)

In undergraduate courses on classical electromagnetism, it is taught that a perfect conductor expels the electromagnetic (EM) field, and hence its surface is not able to support the propagation of bound EM waves. However, when the surface of a perfect conductor is structured at a length scale much smaller than the operating wavelength, geometrically induced surface EM modes can be supported. Owing to their similarities with the surface plasmon polaritons (SPPs) in the optical regime, these surface EM modes were named *spoof* surface plasmons. The concept of spoof surface plasmons has opened up a new line of research within plasmonics with the aim of transferring all the potentialities of SPPs in the optical regime to lower frequencies (microwave, terahertz, and midinfrared regimes) in which a metal behaves as a quasiperfect conductor. In recent years, several research groups have extended this concept from planar surfaces to waveguides, and eventually to resonators, covering the entire range of structures studied in standard plasmonics. This review provides a detailed perspective on the recent developments in spoof surface plasmon photonics from both the fundamental and applied sides.

CONTENTS

[*]fj.garcia@uam.es
[†]tjcui@seu.edu.cn

I. INTRODUCTION AND HISTORICAL PERSPECTIVE

The interface between a metal and a dielectric material supports electromagnetic (EM) modes, exponentially bound to both sides of the interface, known as surface plasmon polaritons (SPPs) (Ritchie, 1957; Raether, 1988b; Pitarke *et al.*, 2007). SPPs have been widely studied for their possible use in modifying light-matter interactions in general and, in particular, for their associated field enhancement, their capability to concentrate light, and their sensitivity to the dielectric environment, which allows the sensing of minute quantities of materials (Zayats, Smolyaninov, and Maradudin, 2005; Maier, 2007).

The physical origin of SPPs resides in the conduction electrons that govern the optical response of metals. These quasifree electrons present a natural plasma frequency that sets the speed at which they can oscillate resonantly. Plasma frequencies of metals are spectrally located in the petahertz range, in the ultraviolet part of the EM spectrum. This makes metals behave as perfect conductors for low-frequency radiation. In the gigahertz and terahertz regimes, conduction electrons respond fast enough to efficiently screen out any external EM stimuli, expelling them completely from the volume of the metal. However, at higher frequencies approaching the optical and visible regimes ($\sim$500 THz), conduction electrons can no longer shield EM fields as efficiently. As a result, EM fields penetrate into the metal bulk, with an exponential decay dictated by the so-called skin depth (δ). This depends on the frequency-dependent metal permittivity ϵ_m as $1/\sqrt{|\epsilon_m|}$. Notice that in the perfect conductor limit ($\epsilon_m \to -\infty$) δ tends to zero, implying complete screening of the EM fields, as previously commented.

When analyzing the existence of bound EM modes propagating at metal-dielectric interfaces, a finite metal skin depth also plays a decisive role. As is shown in more detail in Sec. II, the parallel component of the magnetic field associated with these EM modes must be continuous along the interface. Using Maxwell's equations, it can be shown that this can occur only when the polarization of the EM field is transversal magnetic (TM) and $\epsilon L_d = -\epsilon_m \delta$, with ϵ the permittivity of the dielectric material and L_d the decay length of the bound EM mode in that medium. This equation implies that the confinement of the bound EM modes in the dielectric side scales as $\sqrt{|\epsilon_m|}$, and thus is inversely proportional to their confinement in the metal (the skin depth). Therefore, in the perfect conductor limit no bound EM modes (i.e., SPPs) can be supported, as their corresponding decay length in the dielectric side would be infinite.

This reasoning also explains why, although SPPs nominally exist in all frequency regimes, their useful characteristics typically only occur in the optical and near infrared regimes. In the optical regime, SPPs supported by good plasmonic metals (like gold or silver) have a skin depth of the order of 25–30 nm and, accordingly, a subwavelength confinement inside the dielectric. But, since the ratio between skin depth and wavelength decreases rapidly as the frequency decreases, SPPs in the terahertz regime are already so delocalized in the dielectric region that they are useless for most applications. The skin depth and, correspondingly, the confinement of SPPs in the dielectric side, can be enlarged by reducing the screening of EM fields by the metal, i.e., by reducing its electron density. This is not possible in bulk metals, due to the large initial electron density of 1 to 2 electrons per atom. But it can be achieved by using doped semiconductors as metallic systems, as then the plasma frequency (and thus ϵ_m) can be tuned via the doping density, which is several orders of magnitude smaller than the electron density in a metal (Agranovich and Mills, 1982).

Another route to increasing SPP confinement is to keep using metals, but with patterned apertures on their surfaces. The idea is that the EM field penetration inside the apertures will, on average, correspond to that of a metal with a larger skin depth (Pendry, Martín-Moreno, and García-Vidal, 2004). This initial idea was backed by a simple model showing that aperture-induced EM bound modes appear when a periodic array of small apertures is perforated on a semi-infinite perfect electrical conductor (Pendry, Martín-Moreno, and García-Vidal, 2004; García-Vidal, Martín-Moreno, and Pendry, 2005). Moreover, via a homogenization procedure it was shown that the corrugated surface can be considered a *metamaterial* with an effective dielectric function of the Drude type. Notably in a perforated perfect conductor the effective plasma frequency is determined by the cutoff wavelength of the apertures and not by the electron density. As we discuss in Sec. II, in a corrugated real metal the effective permittivity in general has both dielectric and geometric contributions. Notice also that periodicity is an important ingredient. In a periodic system radiation is prevented when the free-space wavelength is larger than 2 times the period, while in a nonperiodic system the bound EM mode couples to radiative waves.

To summarize the previous idea in an informal way, one could say that, even for a perfect conductor, the penetration inside the apertures has "fooled" the EM field into "believing" that it is encountering a metal with a finite skin depth, i.e., a finite permittivity. Correspondingly, the associated bound EM modes were termed spoof surface plasmons, or spoof SPs. As a historical note, the term "spoof surface plasmons" did not appear in the original publication (Pendry, Martín-Moreno, and García-Vidal, 2004), as the authors complied with an editorial suggestion to refrain from using it. In fact, the first experimental verification used the alternative name "designer surface plasmons (Hibbins, Evans, and Sambles, 2005)." The term spoof surface plasmons was, however, used in presentations in conferences and eventually made its way into the scientific literature.

The fact that spoof SPs can be created simply by geometrical means has allowed their emergence in a broad range of frequencies, ranging from the microwave to the midinfrared regimes, those in which a metal behaves as a quasiperfect conductor. This broadband capability, which differentiates them from standard SPPs and gives them many potentialities, as we later show, presents some similarities with the Bloch

surface waves supported by truncated dielectric photonic band gap structures (Joannopoulos *et al.*, 2008). In this type of dielectric structure, for frequencies within the photonic band gap of the system only surface EM modes can be excited, as bulk modes are forbidden.

Notice that planar metal grids have been extensively studied in the past, especially by the radio and microwave engineering communities. The main focus of these studies was to modify the radar cross section of antennas (using a proper design of radomes), and in general to create filters for modifying the properties of *radiative* waves (Munk, 2000). The structures were known as aperture arrays and frequency-selective surfaces in the radio and microwave communities, respectively. The considered metal grids were thicker than the skin depth but much thinner than the wavelength, so they are usually modeled as current sheets (Agranovich and Mills, 1982). Thus, these structures are more akin to transition layers than to metal films supporting surface EM waves. Bound EM modes exist in frequency-selective surfaces (Ulrich and Tacke, 1973), but they are used mainly in leaky-wave antennas and phased arrays (Mailloux, 2017), which are usually designed not to propagate EM fields in the plane but instead to radiate them into free space.

The EM fields in frequency-selective surfaces and the planar metal grids considered for developing the concept of spoof SPs share many similarities, despite the differences both in the range of geometrical parameters and in the applications sought after. Still, the spoof SP idea brought the novel physical insight that the penetration of the EM field in apertures in a perfect conductor is akin to the penetration in a real metal. Additionally, the similarity of the effective permittivity of the corrugated surface to that of a Drude metal immediately suggested that many of the geometries and concepts in the field of plasmonics (Maier, 2007) could be transferable from the optical regime to longer wavelengths. This insight has been useful to "spoof" not only SPPs but also localized surface plasmons and different plasmonic waveguides, like wedge and channel plasmons, and to discover new types of confined EM waves such as the so-called domino plasmons and their two-dimensional (2D) counterpart, the conformal surface plasmons. Overall, spoof plasmon structures added to the known beam shaping capabilities of metal grids are those of field concentration and field enhancement.

Because of their merits, spoof SPs are also valuable in engineering applications. In the early stages of spoof SP research, the bulkiness of the devices and the low excitation efficiency of structures supporting spoof SPs seriously restricted the development of functionalities based on them. Conformal surface plasmons propagating in ultrathin metal films were devised (Shen *et al.*, 2013), and their efficient excitation technology has laid a solid foundation for a wide range of applications of spoof SPs in the microwave engineering community. Thus far spoof SPs have been used as a mature solution to solve many practical problems. With their adjustable wave vector, spoof SPs currently play an important role in the miniaturization of circuit devices. Their unique dispersion characteristics make them possess a larger wave vector than those EM modes supported by traditional transmission lines and, more importantly, their wave vector can be controlled at will by simply changing the geometrical

parameters. The miniaturization techniques based on spoof SPs have been applied in antennas, filters, sensors, and other microwave and millimeter-wave devices. In addition, the tight EM field concentration associated with propagating spoof SPs allows one to suppress cross talk between adjacent waveguides that can even present a deep-subwavelength separation without noticeable coupling. Currently the demand for high-density circuits is increasing, and spoof SPs may provide a way to solve the EM compatibility problem in the physics layer. Along these lines, this technology has been used recently in the development of new architecture wireless communication systems (Zhang, Zhang, He *et al.*, 2020). Finally, since the concept of spoof SPs has been also transplanted to localized SPs, this powerful approach has enabled the realization of various resonators that are widely used in sensing and imaging. Recently a wireless body sensor network that is based entirely on the spoof SP components was designed and implemented (Tian *et al.*, 2019).

In not many research areas is it possible to find such a short delay between the first fundamental studies and such cutting-edge applications as spoof surface plasmon photonics. In less than 20 years, we have seen how this field of investigation has evolved from basic studies on 2D hole arrays in 2004 to the development of different waveguiding schemes and resonators that have led to a feasible implementation of both passive and active devices. These devices have recently been incorporated into wireless telecommunication systems and body sensor technology. This is why we envisage that this area of research will focus in the coming years on the applied front, thereby exploring new functionalities for spoof SPs in different areas. Flexible circuits are urgently demanded in wearable equipment and implantable medical devices. By constructing ultrathin spoof SP structures on flexible films, conformal surface plasmon modes are able to confine fields on arbitrarily curved surfaces. Considering the fact that the deformation of circuits may lead to signal leakage and cross talk, conformal surface plasmons are one of the most promising candidates to be used in flexible circuits, thanks to their tight EM confinement. The maximum capacity of integrated circuits is limited by problems with signal cross talk in high-density channel arrangements, which hinder its miniaturization. In fact, this is the intrinsic shortcoming of loose modes in traditional microstrips and coplanar waveguides. Spoof SPs provide a physical-layer route to resolve these challenges. By concentrating signals tightly around the transmission media, the coupling between channels can be effectively suppressed. Finally, in modern electronic systems, signal processing is intensively carried out in digital modules, which has been an area of great progress in information technology. Meanwhile, this rule limits the prospect of digitalization because their operation is still purely analogic. By introducing tunable elements into spoof SP structures, one can achieve digital operations within the physical layer. In this way, an intelligent design of subwavelength spoof SPs can then provide a significantly increase in the manipulation of both signal processing and system reconfiguration.

Today research in metasurfaces in general, and spoof SPs in particular, is an active area. There have already been noteworthy reviews on the former (Chen, Taylor, and Yu, 2016; Glybovski *et al.*, 2016). In what follows we review the

research on spoof surface plasmon structures, with an emphasis on both fundamental physical ideas and applications. The structure of this review is as follows. In Sec. II, we consider planar surfaces textured by one- and two-dimensional aperture arrangements, which are the original geometries where the emergence of spoof SPs was predicted. We discuss the material and geometrical contributions to the mode binding and the first experimental verifications of spoof SPs in the microwave and terahertz regimes. In Sec. III, we review various spoof SP waveguides with decreasing effective mode volumes, from freestanding cylindrical geometries to domino plasmons and, finally, to conformal surface plasmons. In Sec. IV, we analyze the emergence of spoof localized SPs in structured metallic resonators, of superwavelength and sub-wavelength dimensions. We also report on the near-field coupling between spoof SP modes in neighboring structures. Technological applications of the spoof SP concept are presented in Sec. V, which reviews various active and passive devices that have been realized in recent years. Finally, a summary and outlook are presented in Sec. VI.

II. PLANAR SURFACES

In this section we consider corrugated planar metal surfaces, which are the simplest systems that support geometrically induced bound EM modes, i.e., spoof SPs. We focus particularly on the two periodic configurations sketched in Fig. 1: a one-dimensional (1D) array of grooves [Fig. 1(a)] and a 2D array of dimples [Fig. 1(b)], both of which are perforated on a flat surface. The three geometric parameters characterizing these systems are the period d, the corrugation width a, and the depth h.

A. Theoretical framework

Before considering the effect of corrugations, it is convenient to start revisiting the conditions for the existence of bound EM modes in a planar interface between two homogeneous semi-infinite and nonmagnetic media. For this analysis, the choice of axes is shown in Fig. 1. The bottom semi-infinite medium is metallic, with permittivity $\epsilon_m(\omega)$, and the top one is a dielectric, with constant permittivity ϵ (which we set to 1 for simplicity).

Finding the EM bound modes in the uncorrugated configuration is a textbook example of EM field matching (Botten and McPhedran, 1985). In each homogeneous region, the fields can be expanded in a basis characterized by the in-plane wave vector and the polarization. We reserve $\vec{k} = k_x \vec{u}_x + k_y \vec{u}_y = (k_x, k_y)$ for the in-plane momentum so that the three-dimensional (3D) momentum $\vec{k}_{3D} = \vec{k} + k_z \vec{u}_z = (\vec{k}, k_z)$, with[1] $k_z = \sqrt{\epsilon k_0^2 - k^2}$, where $k_0 = \omega/c$ and c is the speed of light. The polarization can be set to be either transverse electric (TE) (or s polarization) or transverse magnetic (TM) (or p polarization), depending on whether the electric or the magnetic field is perpendicular to the selected reference

---

[1]As a technical point, the sign of the square root must be taken such that $\lim_{\eta \to 0} \mathrm{Im}[k_z(\omega + \iota\eta)] \geq 0$. With this, EM fields do not explode at infinity and can thus be normalized.
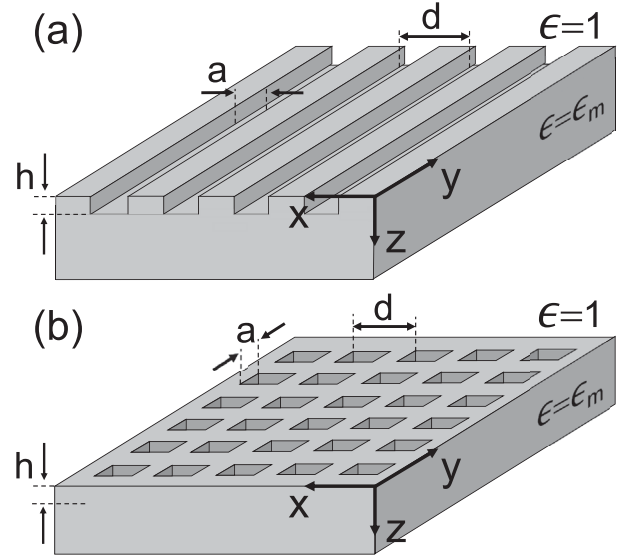

FIG. 1. The periodically corrugated planar geometries considered in Sec. II, which mimic a planar interface between air and a semi-infinite metal. (a) 1D array of rectangular grooves. (b) 2D array of square dimples. In both geometries, d stands for the periodic lattice and a and h represent the lateral size and depth of the indentations, respectively.

direction. Choosing this direction to be the normal to the interface z and using Maxwell equations to express the magnetic field $\vec{H}$ in terms of the electric field $\vec{E}$, we have

$$\vec{E}_{\vec{k},\sigma}(\vec{r}) = A e^{\iota \vec{k}_\parallel \cdot \vec{r}_\parallel} e^{\pm \iota k_z z} \vec{u}_{\vec{k},\sigma}, \tag{1}$$

$$-\vec{u}_z \times \vec{H}_{\vec{k},\sigma}(\vec{r}) = \pm Y_{\vec{k},\sigma} \vec{E}_{\vec{k},\sigma}(\vec{r}), \tag{2}$$

with $\vec{u}_{\vec{k},s} = (1/k)(-k_y, k_x)^T$ and $\vec{u}_{\vec{k},p} = (1/k)(k_x, k_y)^T$, and admittances $Y_{\vec{k},s} = k_z$ and $Y_{\vec{k},p} = \epsilon/k_z$. In Eq. (2) the plus-minus sign has to be chosen such that the field propagates (or decays) in the direction pointing to infinity. A is a normalization constant, which in a periodic system can be chosen as $A = 1/\sqrt{A_{\mathrm{WS}}}$, where A_{WS} is the area of the Wigner-Seitz unit cell.

For a flat interface, the continuity of the parallel components of both electric and magnetic fields leads to the following condition for the existence of an EM bound mode with polarization σ:

$$Y_{\vec{k},\sigma}^{(\mathrm{I})} = -Y_{\vec{k},\sigma}^{(\mathrm{II})}. \tag{3}$$

If absorption is negligible in both media, Eq. (3) can be fulfilled only for TM polarization and only if one medium is a dielectric ($\epsilon > 0$) and the other one is a metal ($\epsilon_m < 0$). In that case, the bound EM modes are called SPPs (Raether, 1988a) and present an in-plane wave vector

$$k = k_0 \sqrt{\frac{\epsilon \epsilon_m}{\epsilon + \epsilon_m}} \tag{4}$$

and out-of plane wave vector $k_z = k_0\sqrt{\epsilon^2/(\epsilon + \epsilon_m)}$ in the dielectric medium. Recall that in these expressions both k_0 and ϵ_m are frequency dependent.

Bound EM modes, i.e., SPPs, occur for $\text{Re}\{-\epsilon_m\} > \epsilon$. In the case in which $k > \sqrt{\epsilon}k_0$, the dispersion relation falls outside the light cone and the associated EM fields decay exponentially away from the interface. The field confinement can be characterized by $L_z^{\text{SPP}} \equiv 1/\text{Im}(k_z)$ or, in units of the wavelength in vacuum λ, $L_z^{\text{SPP}}/\lambda = \text{Im}\{\sqrt{\epsilon + \epsilon_m}\}/2\pi\epsilon$. This quantity is small for $\epsilon_m \approx -\epsilon$ (for metals this typically occurs in the optical regime), which describes the strong EM field confinement that is one of the main drivers in the field of plasmonics (Maier, 2007). On the contrary, for larger wavelengths (in the microwave or terahertz regimes) $|\epsilon_m| \gg 1$ and the field is extremely delocalized. In fact, in the limit $\epsilon_m = -\infty$ (perfect conductor limit) the EM fields do not penetrate inside the metal. As a result, flat surfaces of perfect electrical conductors do not support SPPs, as previously discussed.

As stated in the Introduction, the close link between EM field penetration on the metal side and the existence of EM modes bound to metal-dielectric interfaces is the key idea behind the concept of spoof surface plasmons (Pendry, Martín-Moreno, and García-Vidal, 2004): periodic indentations in the interface allow the EM field to penetrate in what would otherwise be a metallic region. This effectively creates a metamaterial (García-Vidal, Martín-Moreno, and Pendry, 2005) that, on average, resembles a flat metal-dielectric interface, leading to the formation of bound EM modes, the so-called spoof SPs. This is a geometrical effect that operates even at frequency ranges where metals behave as quasiperfect conductors. This intuitive idea can be backed up by calculations. EM properties of spoof SPs in complex geometries have been characterized by means of accurate numerical methods. Numerical solutions of Maxwell's equations are obtained in this review using three different tools, implemented in homemade codes or commercial software: the finite-difference time-domain method,[2] the finite-integration technique,[3] and the finite-element method.[4] These are different in nature and present pros and cons depending on the geometry (waveguides or resonators), underlying materials (real metals or perfect conductors), and mode of operation (time or frequency domain) of the spoof SP structure under study.

For illustrative purposes, here we mainly use the coupled mode method (de León-Pérez *et al.*, 2008; Garcia-Vidal *et al.*, 2010), which, although a simple approximation, is able to capture the physics of the problem and provides the main dependences on all parameters. The ingredients of the simple coupled mode description of spoof SPs are as follows: (i) EM fields in the dielectric region are expanded in terms of the all possible diffracted (Bragg) plane waves, (ii) the surface corrugation is described as truncated waveguides and the field inside the indentations is expanded in terms of the corresponding waveguide modes, and (iii) the modal amplitudes are obtained through the matching of fields at the interfaces according to the dictate of Maxwell equations. A simplification occurs when the field penetration inside the metal

is much smaller than any other length scale in the problem: the period d, the dimensions of the indentations a and h, the operating wavelength λ, etc. As the skin depth is of the order of 30 nm in the optical regime and 30–120 nm in the terahertz range (Ordal *et al.*, 1983), this condition usually holds for infrared frequencies and below. In that case, the existence of metal boundaries can, to a good approximation, be taken into account using the so-called surface-impedance boundary condition $\vec{E} - z_s\vec{u}_n \times \vec{H} = 0$, where $\vec{E}$ and $\vec{H}$ are fields in the dielectric, $z_s = 1/\sqrt{\epsilon_m}$ is the surface impedance, and $\vec{u}_n$ is a unitary vector normal to the interface pointing toward the dielectric (Landau *et al.*, 2013). Even within this approximation the computation of waveguide modes for arbitrary geometries is far from straightforward. Therefore, for the description of the spoof SPs sustained by the corrugated surfaces in Fig. 1, we describe the vertical metallic walls of the indentations as perfectly conducting and use the surface-impedance boundary condition only for the horizontal interfaces at $z = 0, -h$. This is a valid approximation for both structures because horizontal metallic surfaces cover a larger area than the vertical ones.

With all the previously introduced ingredients, the EM eigenmode calculation for the structures in Fig. 1 can be cast into a homogeneous set of linear equations for the modal amplitudes of the electric field at the indentation openings ($z = 0$). These have the form

$$\sum_m G_{nm}E_m - \Sigma_n E_n = 0, \tag{5}$$

where indices n and m run over the different waveguide modes at the indentations, with amplitudes E_n. The interpretation of the two previous terms can be done considering the Huygens principle, where each opening acts as a source of EM fields. G_{nm} accounts for the radiative coupling between modes n and m, as part of the EM field that is radiated by mode m illuminates mode n. On the other hand, Σ_n originates from the EM fields that travel down the indentation, bounces at the bottom interface ($z = -h$), and returns to the opening. The explicit expressions for G_{nm} and Σ_n were given by de León-Pérez *et al.* (2008) and Garcia-Vidal *et al.* (2010). Note that the spoof SP dispersion relation (modal frequency versus propagating wave vector) is given by the vanishing condition for the determinant of the matrix of the coefficients in Eq. (5).

As anticipated, the coupled mode method is a suitable theoretical tool for the description of spoof SPs in corrugated planar surfaces. It provides deep insight into the frequency-dependent properties of these geometrically induced EM modes through a simple approximation. Taking advantage of the subwavelength character of the indentations (typically $a, h \ll \lambda$), the EM fields inside the corrugations can be described by only the fundamental waveguide mode ($n = 0$). In that case, the spoof SP dispersion relation is given simply as

$$G_{00} - \Sigma_0 = 0, \tag{6}$$

which is now a single homogeneous equation with

$$G_{00} = \sum_{\vec{G},\sigma} \frac{Y_{\vec{k}+\vec{G},\sigma}}{1 + z_s Y_{\vec{k}+\vec{G},\sigma}} S_{\vec{k}+\vec{G},\sigma}^2, \tag{7}$$

[2]See https://www.lumerical.com.
[3]See http://www.cst.com.
[4]See http://www.comsol.com.

$$\Sigma_0 = -Y_0 \frac{f_0^- e^{\imath k_z^0 h} + f_0^+ e^{-\imath k_z^0 h}}{f_0^- f_0^+ (e^{\imath k_z^0 h} - e^{-\imath k_z^0 h})}, \tag{8}$$

where

$$S_{\vec{k},\sigma} = \int [\vec{u}_{\vec{k}\sigma} \cdot \vec{E}_\parallel^0(\vec{r}_\parallel)] e^{-\imath \vec{k} \vec{r}_\parallel} d\vec{r}_\parallel \tag{9}$$

and $f_{\vec{k},\sigma}^\pm = 1 \pm z_s Y_{k,\sigma}$. The fundamental waveguide mode is characterized by k_z^0, Y_0, and $\vec{E}_\parallel^0(\vec{r}_\parallel)$, which are its propagation constant, admittance, and in-plane electric field, respectively, and $f_0^\pm = 1 \pm z_s Y_0$. The summation in Eq. (7) is over all reciprocal lattice vectors $\vec{G}$ of the periodic system.

Further insight into the spoof SP dispersion relation can be obtained by treating the surface as a metamaterial, via a homogenization procedure consisting of neglecting the diffraction orders in G_{00}. The condition for the existence of a bound surface mode with wave vector $\vec{k}$ in Eq. (6) then becomes $S_{\vec{k},\sigma}^2/(Y_{\vec{k},\sigma}^{-1} + z_s) - \Sigma_0 = 0$. Note that if diffraction is disregarded, modes can be characterized by the polarization index σ. For $\sigma = \mathrm{TM}$, Eq. (6) reads

$$Y_{\vec{k},\mathrm{TM}}^{-1} = k_z = -z_s - z_s^{\mathrm{geom}}, \tag{10}$$

with $z_s^{\mathrm{geom}} \equiv -S_{\vec{k},\mathrm{TM}}^2/\Sigma_0$. Equation (10) can be used to estimate whether the dielectric z_s or the geometrical z_s^{geom} impedance dominates in a given structure within a given spectral range.

Recall that Eq. (6) takes care of the complex self-consistent process of the propagation of EM fields at the surface and their mixing via scattering at the indentations. Intuitively, indentations have a dual role: they act as primary sources of scattering and the EM fields also spend some time inside them, thus affecting the effective speed of propagation of the bound EM mode. In particular, even in the optical regime a corrugated metal surface supports the propagation of a modified SPP, composed mainly of SPP fields in the flat interface that scatter and are delayed by the corrugations (Nesterov *et al.*, 2010). The link between indentation-modified SPPs and flat-surface SPPs can be understood through perturbation of the original bound EM mode. The emergence of spoof SPs in a corrugated perfect conductor surface is less intuitive from this point of view, as they appear even though there is no bound EM mode to be perturbed in the absence of indentations. The intuition provided by Eq. (10) on the existence of a purely geometric impedance is useful when utilizing this picture to go deep into the physical origin of spoof SPs.

In Secs. II.B and II.C, we consider both 1D and 2D arrays and show how the spoof SP complex band structure [computed using Eq. (6)] and the related physical magnitudes of vertical confinement of the bound EM mode and its propagation length depend on the geometrical parameters.

B. 1D gratings: Groove arrays

We first explore spoof SPs in groove arrays; see Fig. 1(a). Taking advantage of the translational symmetry of this structure in the y direction, we can focus on EM modes with $k_y = 0$. Thus, the fundamental waveguide mode inside the

slits is a propagating transverse-electromagnetic (TEM) mode[5] (now defined with respect to the x-z plane) with $\vec{E}_\parallel^0(\vec{r}_\parallel) = a^{-1/2}\vec{u}_x$ and $k_z^0 = k_0$. This mode couples to TM-polarized modes only in the dielectric region, with overlap $S_k = \sqrt{a/d}\,\mathrm{sinc}(ka/2)$ (Porto, García-Vidal, and Pendry, 1999; Collin *et al.*, 2001).

Intuition on the conditions for the existence of bound EM modes can be obtained by analyzing Eq. (10). Under the perfect conductor approximation for the metallic regions ($\epsilon_m = -\infty$ and $z_s \to 0$) and assuming that $\lambda \gg d$ and $S_k \approx \sqrt{a/d}$, the geometric impedance becomes $z_s^{\mathrm{geom}} = -\imath(a/d)\tan(k_0 h)$. Thus, for $\tan(k_0 h) > 0$ (in particular, for $\lambda > h/4$) the groove array behaves as an effective metal, supporting spoof SPs with the dispersion relation

$$k = k_0 \sqrt{1 + \left(\frac{a}{d}\right)^2 \tan^2(k_0 h)}. \tag{11}$$

The corrugated surface does not support spoof SP modes for $\tan(k_0 h) < 0$. However, in that case, the structure sustains TE-polarized bound modes that are reminiscent of the waveguide modes in a planar dielectric slab (Shen, Catrysse, and Fan, 2005). Note that in the perfect conductor limit spoof SP bands are scalable: increasing all length scales in Eq. (11) by a factor F yields the same dispersion relation, but with both k and k_0 multiplied by $1/F$. Taking advantage of this result, in the following we consistently present band structures normalized to the frequency and wave vector of the smallest reciprocal lattice vector $\vec{G} = (2\pi/d)\vec{u}_x$. To compare spoof SPs with SPPs, we use this normalization even for cases when we consider a finite z_s.

Note that Eq. (11) is exactly the same dispersion relation that is obtained when the indentations are replaced by a *homogeneous* and *anisotropic* medium layer of thickness h. The effective permittivity tensor for this medium can be derived by considering that the electric field inside the grooves points only along the x direction, yielding $\epsilon_{yy} = \epsilon_{zz} = \infty$. Moreover, by imposing continuity on the spatial average of the displacement vector at $z = 0$, one obtains $\epsilon_{xx} = a/d$. Its effective magnetic permeability can be found by forcing the EM fields to penetrate in the anisotropic layer with the same propagation constant as they have in the metal corrugations, leading to $\mu_{xx} = 1, \mu_{yy} = \mu_{zz} = 1/\epsilon_{xx} = d/a$.[6]

---

[5]A TEM mode is characterized by both electric and magnetic fields being perpendicular to the direction of propagation, as in an EM plane wave. Depending on the boundary conditions, it can propagate only in specific geometries like infinitely long slits, as in this case, or in coaxial waveguides, among other possibilities.

[6]Technically, we consider here whether the bound modes in the corrugated structure are more akin to Dyakonov waves (D'yakonov, 1988), EM modes bound at the interface between an isotropic dielectric and a uniaxial dielectric with the optical axis in an in-plane direction, than to SPPs. This is not the case, as spoof SPs are longitudinal waves (as bona fide SPPs are; Dyakonov waves are not), and because the conditions for existence of Dyakonov waves ($\epsilon_{xx} > \epsilon > \epsilon_{zz}$) are not fulfilled by the effective dielectric tensor of the corrugated surface, which, unlike in the case considered by Dyakonov, also presents a uniaxial effective magnetic permeability tensor.
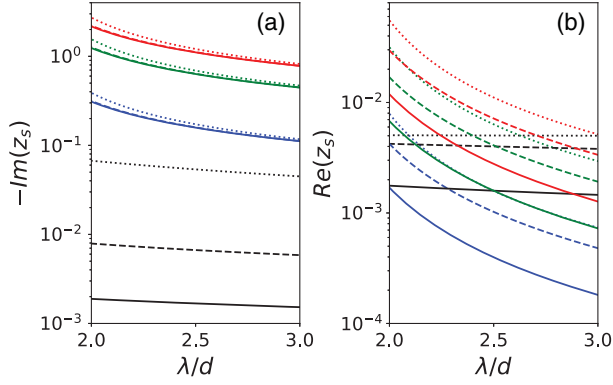
FIG. 2. Spectral dependence of both material impedance z_s (black curves) and geometrical impedances z_s^{geom} (color curves) in a groove array. (a),(b) The imaginary and real parts, respectively. The geometrical parameters are $h/d = 0.4$ and $a/d = 0.1$ (blue lines), 0.4 (green lines), and 0.7 (red lines). The line types represent different periods and spectral ranges: $d = 1\ \mu$m (dotted lines), $d = 10\ \mu$m (dashed lines), and $d = 100\ \mu$m (continuous lines). Note that $\text{Im}(z_s^{\text{geom}})$ virtually coincide for $d = 10$ and $100\ \mu$m.

FIG. 3. Spoof SP bands for the groove arrays in Fig. 2 ($h/d = 0.4$). The mode frequency normalized to the array period d/λ is plotted against the propagating wave vector in units of the smallest reciprocal lattice vector, $|\vec{G}| = 2\pi/d$. Three groove widths, $a/d = 0.1$, 0.4, and 0.7 (blue, green, and red lines, respectively), and three periods, $d = 1$, 10, and 100 μm (dotted, dashed, and solid lines, respectively), are shown. The black lines render the dispersion relation of the corresponding SPP. The open squares render simplified, metamaterial predictions given by Eq. (11).

Although approximate, this metamaterial approach highlights that the dispersion relation of spoof SPs and the effective material parameters can be tailored through geometry (Pendry, Martín-Moreno, and García-Vidal, 2004; García-Vidal, Martín-Moreno, and Pendry, 2005).

In what follows, we go beyond the effective medium approach by accounting for both the diffraction and the finite permittivity of metals. We focus on the dependence on the different geometrical parameters of spoof SP characteristics and highlight the impact of the metal response in different spectral ranges. We consider a Drude dielectric constant $\epsilon_m = 1 - \omega_p^2/\omega/(\omega + \iota\gamma)$, with $\omega_p = 9$ eV and $\gamma = 0.01\omega_p$, which is a good approximation for silver at frequencies below the optical regime. Figure 2 shows the wavelength dependence of the imaginary [Fig. 2(a)] and real [Fig. 2(b)] parts of both material and geometric impedances in Eq. (10) for a groove array with $h/d = 0.4$. The line style indicates the spectral regime (set through the array period), ranging from the infrared to the terahertz. Black lines plot the material impedance, which depends on the frequency but not the corrugation geometry. Blue, green, and red lines correspond to geometric impedances for different groove widths a/d. The imaginary part of the impedance (reactance) is larger than the real part (resistance) in all cases. The geometric reactance is virtually independent of the material properties (and thus of the wavelength range), but, as expected, it strongly depends on a/d. By contrast, the material reactance depends on λ, decreasing for larger d. We can observe that the geometric impedance always dominates, except for the narrowest slits and the shortest wavelengths considered. Figure 2(b) shows that the resistance also increases with smaller λ and, in contrast to the reactance, its geometrical contribution strongly depends on the groove width.

Figure 3 shows the spoof SP dispersion bands for the groove arrays and spectral ranges ($2d < \lambda < 3d$) that were analyzed in Fig. 2. Again colors code the corrugation width,
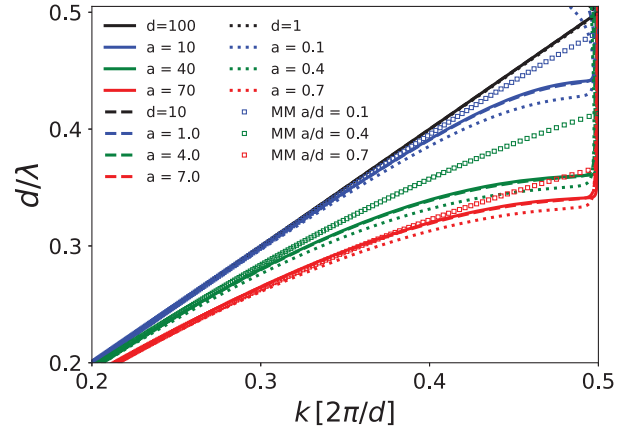
while line styles indicate the corrugation period. The dispersion relation of conventional SPPs for a flat silver surface is rendered in black lines, but its deviation from the light cone is not appreciable. We can observe that the effect of the corrugation is apparent in all frequency ranges, and that bands for $d = 10$ (dashed lines) and $100\ \mu$m (solid lines) coincide, meaning that the spoof SP characteristics are independent of the metal permittivity in these cases. As the groove width increases, the modal frequency d/λ deviates more and more from the light cone. Therefore, spoof SPs become more bounded, especially as the wave vector approaches $k = \pi/d$, the boundary of the first Brillouin zone, where bands flatten and a gap opens in the dispersion relation. The dotted lines ($d = 10\ \mu$m) reveal that the mode binding increases at shorter wavelengths thanks to the material impedance. Figure 3 also shows the dispersion relation predicted by the metamaterial approach in Eq. (11). While this simple analytical expression is qualitatively correct, the neglect of diffraction fails to capture the opening of a band gap at $k = \pi/d$ and underestimates the modal binding to the surface.

Surface EM modes can be characterized by two quantities. First, as previously introduced for conventional SPPs, their extension along the direction perpendicular to the surface is $L_z \equiv 1/\text{Im}\{k_z\}$. Second, the figure of merit (FOM), defined as the number of modal periods that the bound mode propagates before its amplitude decays in a factor $1/e$, is $\text{FOM} \equiv \text{Re}\{k\}/2\pi\text{Im}\{k\}$. Figure 4 shows L_z/λ [Fig. 4(a)] and FOM [Fig. 4(b)] for the groove arrays studied in the previous figures. For all frequency ranges, the corrugation supports spoof SPs (colored lines) that are significantly more bound to the metal surface, and therefore propagate for a shorter distance, than their conventional SPP counterparts (black lines). In the infrared regime [$d = 1\ \mu$m (blue lines)],
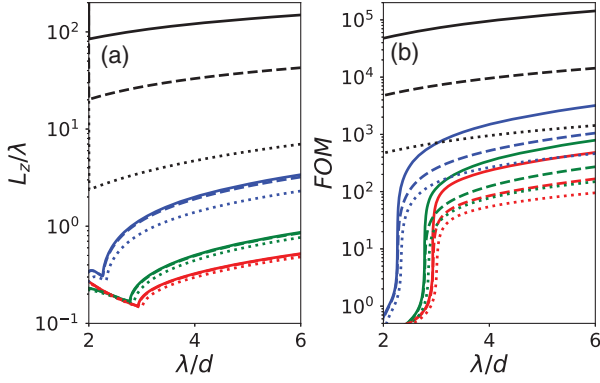
FIG. 4. (a) Vertical confinement and figure of merit (FOM), as defined in the text, (b) for the spoof SPs sustained by the groove arrays analyzed in Figs. 2 and 3. The grooves have a fixed depth, $h/d = 0.4$, three different groove widths $a/d = 0.1, 0.4,$ and 0.7 (blue, green, and red lines, respectively), and three periods $d = 1$, 10, and 100 μm (dotted, dashed, and solid lines, respectively). The black lines render the two quantities evaluated for conventional SPPs.

the indentation geometry allows one to tune the trade-off between propagation and confinement (Nesterov *et al.*, 2010). The wider the grooves, the larger the vertical, out-of-plane confinement and the lower the FOM. At longer wavelengths [$d = 10$ (green lines) and 100 μm (red lines)], the character of the bound EM modes on the corrugated surfaces is qualitatively different from those on the flat ones, with a reduction of up to 3 orders of magnitude for both quantities. Figure 4 also reveals points of minimum FOM and cusps in L_z/λ. These points correspond to spoof SPs entering the band gap region, where the propagating wave vector picks up a large imaginary component. In general, the normalized vertical confinement is less sensitive to the material properties than the FOM. Note that within the perfect conductor approximation the latter tends to infinity in all cases.

C. Two-dimensional gratings: Dimple arrays

Spoof SPs also appear in 2D arrays of dimples. Following the spirit of Sec. II.B, which focused on fundamental aspects, we restrict our attention here to a square lattice of square apertures. This geometry is depicted in Fig. 1(b), and again is defined by the lattice period d and the dimple side and depth a and h, respectively. A general description of the band structure of spoof SPs would require the calculation for wave vectors within the irreducible Brillouin zone. As the considered system has C_4 symmetry around the z axis, the associated EM field, being longitudinal, would transform as the unitary vector along the wave vector direction under C_4 transformations. Here, as in the 1D case, we restrict ourselves to the illustrative case of $k_y = 0$ and describe the spoof SP properties when they propagate along the x direction.

We assume that the indentations are small enough that all the waveguide modes inside them are evanescent; this occurs for $k_0 < \pi/a$ ($a < \lambda/2$). Note that this establishes a fundamental difference versus the groove arrays considered in Sec. II.B, where the lowest mode is always propagating (Porto, García-Vidal, and Pendry, 1999). In the 2D case,

the relevant waveguide mode is TE polarized (García-Vidal *et al.*, 2005) and has an electric field $\vec{E}_\parallel^0(\vec{r}_\parallel) = (\sqrt{2}/a) \times \sin(\pi y/a)\vec{u}_x$, with $k_z^0 = \sqrt{k_0^2 - (\pi/a)^2}$ and an admittance $Y_0 = k_z^0$.

As is done for 1D groove arrays, it is illustrative to start with the metamaterial description of spoof SPs under the perfect conductor approximation. Equation (10) then yields the following analytical expression for the dispersion relation (Pendry, Martín-Moreno, and García-Vidal, 2004):

$$k = k_0\sqrt{1 + \left(\frac{2\sqrt{2}a}{\pi d}\right)^4 \frac{k_0^2}{(\pi/a)^2 - k_0^2}F(h)}, \quad (12)$$

where $F(h) = \tanh^2[\sqrt{(\pi/a)^2 - k_0^2}\,h]$ includes the dependence of the modal wave vector on the corrugation depth. Note that Eq. (12) is scalable in a manner similar to Eq. (11) when all lengths are varied by the same factor.

Equation (12) reveals that the evanescent character of the EM fields inside the dimples yields bound surface EM modes for all indentation thicknesses. Figure 5 renders the spoof SP bands in 2D dimple arrays, within the metamaterial description, and in the limit $F(h \to \infty) = 1$ (that is, when the corrugation depth is much larger than any other length scale in the system). The mode frequencies lie close to the light cone for $\lambda \gg a$ and present flat asymptotes at the cutoff wavelength of the fundamental mode $\lambda_c = 2a$ ($d/\lambda_c = d/2a$). Notice, however, that this band flattening always takes place at $k > \pi/d$. This means that this regime (and the associated EM confinement) should not be accessible once diffraction effects are incorporated into the calculations, as bands are then folded back into the first Brillouin zone when they enter the light cone.

The effective permittivity and permeability tensors can be extracted for the anisotropic metamaterial formed by the corrugations once diffraction effects are neglected, using arguments similar to those employed for 1D groove arrays.
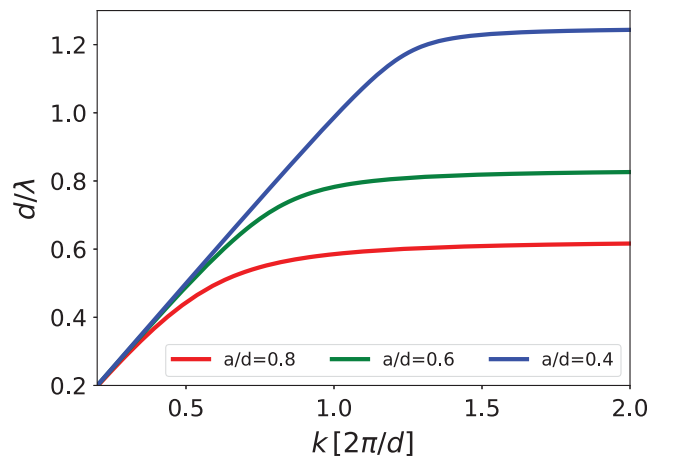

FIG. 5. Spoof SP bands for a 2D square array of square dimples of different sizes, computed using the metamaterial approximation in Eq. (12) (evaluated at $h \to \infty$). As diffraction is neglected, the bands have not been folded into the first Brillouin zone. The asymptote in the dispersion relation occurs at the cutoff wavelength of the fundamental waveguide mode.

As the dispersion of the fundamental waveguide mode is independent of (k_x, k_y), we can assign $\epsilon_{zz} = \mu_{zz} = \infty$. Imposing continuity of both the parallel component of the electric field and the normal component of the Poynting vector, we can write (García-Vidal, Martín-Moreno, and Pendry, 2005)

$$\mu_{xx} = \mu_{yy} = \left(\frac{2\sqrt{2}a}{\pi d}\right)^2, \tag{13}$$

$$\epsilon_{xx} = \epsilon_{yy} = \left(\frac{\pi d}{2\sqrt{2}a}\right)^2 \left(1 - \frac{\pi^2 c^2}{a^2 \omega^2}\right), \tag{14}$$

where we have made the dependence of the permittivities on frequency explicit. Note that these have exactly the same form as the dielectric constant of a lossless Drude metal (Pendry, Martín-Moreno, and García-Vidal, 2004). This approximate metamaterial approach again illustrates how the EM response of corrugated metal surfaces can be tuned through geometry, for instance, by inducing an effective plasma frequency, as shown in Eq. (14).

Figure 6 renders the spoof SP bands for 2D dimple arrays beyond the simplified metamaterial approach, including both diffraction effects and a finite corrugation thickness ($h/d = 0.5$). As in Fig. 3, three different periods ($d = 1$, 10, and 100 μm) and relative dimple sizes ($a/d = 0.4$, 0.6, and 0.8) are considered. The phenomenology of the dependence of the spoof SP dispersion on both parameters is similar to that found in the 1D case: in all spectral and size regimes, the bands are dominated by geometry, with the material properties playing a relevant role only for the smallest wavelengths considered ($\lambda = 2$ to 3 μm for $d = 1$ μm). We can observe gap openings close to $k = \pi/d$, which are especially apparent for large dimples. Figure 6 (inset) shows the comparison of the full result against the metamaterial prediction [Eq. (12)] for dimples with $d = 100$ μm and $a = 60$ μm. The metamaterial approach captures the main trend, but, contrary to the 1D system, it overestimates the deviation of the spoof SP dispersion from the light cone, except close to the band edge, where the diffraction effects are most relevant (de Abajo and Saenz, 2005; Hendry, Hibbins, and Sambles, 2008).

Figure 7 shows both the normalized vertical confinement [Fig. 7(a)] and FOM [Fig. 7(b)] as previously defined of the spoof SP modes studied in Fig. 6. The usual trade-off in plasmonics between out-of-plane confinement and in-plane propagation is apparent. Notice that the ratio L_z/λ is controlled mainly by geometry, while the FOM depends on both EM confinement and metallic absorption. The corrugation enhances the vertical confinement (reduces L_z) of conventional SPPs by 1 to 2 orders of magnitude. Still, the bound EM modes propagate up to hundreds of wavelengths, even in the infrared regime. Only in the vicinity of the spoof SP band gaps (sharp minima in L_z) does a strong suppression of the FOM take place in Fig. 7(b).

We finish the fundamental analysis of this section by pointing out two strategies that increase the binding of spoof SPs to the corrugated metal surface. The first one exploits the filling of the indentations with a high refractive index dielectric ϵ. For $\epsilon > 1$ the cutoff frequency of the fundamental
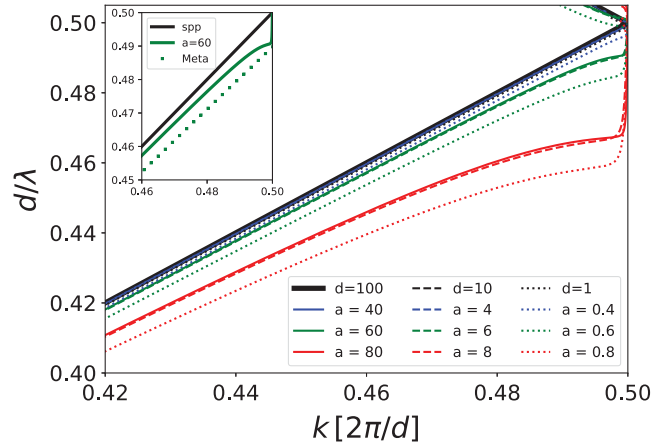

FIG. 6. Spoof SP bands for 2D dimple arrays with $h/d = 0.5$. Line colors indicate the three dimple sizes considered: $a/d = 0.4$ (blue), 0.6 (green), and 0.8 (red). The line types correspond to three periods (and spectral ranges): $d = 1$ μm (dotted), 10 μm (dashed), and 100 μm (solid). The SPP frequencies for a flat metal surface are plotted with black lines (in all cases, they are indistinguishable from the light cone). Inset: comparison between the dispersion relation for conventional SPPs (black curve) and the metamaterial prediction (green dashed line) and full calculations (green solid line) for a dimple array with $d = 100$ μm, $h/d = 0.5$, and $a/d = 0.6$. All the dimensions in the legends are in microns.

mode redshifts, increasing the deviation of the spoof SP band from the light cone and inducing the emergence of cutoff related asymptotes at lower in-plane wave vectors (Martín-Moreno and García-Vidal, 2008). The cutoff wavelength in filled dimples is $\lambda_c = 2a\sqrt{\epsilon}$, while the modal wavelength at the edge of the first Brillouin zone is $\lambda(k = \pi/d) \approx d/2$. Thus, this mechanism is most effective when $\epsilon > (d/4a)^2$.

The second strategy, which is compatible with the first one, consists of removing the bulk metal underneath
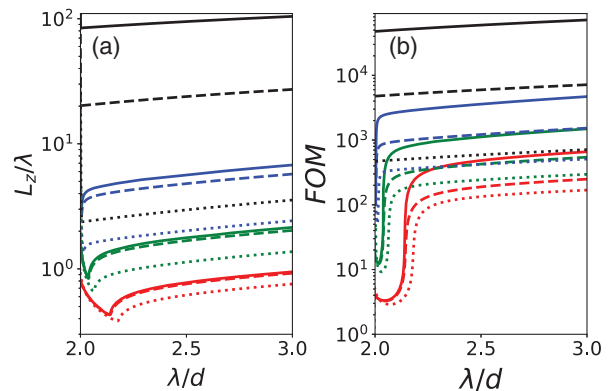

FIG. 7. Vertical confinement and FOM for the spoof SPs in Fig. 6. (a) $L_z = 1/\text{Im}(k_z)$ given in units of the free-space wavelength. (b) Plot of FOM $= \text{Re}\{k\}/(2\pi\text{Im}\{k\})$. Colors and line styles code the relative dimple sizes and array periods considered: $a/d = 0.4$ (blue), 0.6 (green), and 0.8 (red). The three periods (and spectral ranges) are $d = 1$ (dotted), 10 (dashed), and 100 μm (solid). The black lines correspond to conventional SPPs in a flat metal surface.

the indentations. That way, the system becomes a fully perforated metallic film. If the film is thin enough, spoof SPs propagating along the two surfaces hybridize through the holes, leading to a splitting of the dispersion bands. One of them approaches the light cone, becoming more delocalized. This mode, reminiscent of the so-called long-range SPPs (Berini, 2000), propagates longer along the in-plane direction. The other band, more akin to conventional short-range SPPs, redshifts and deviates further from the light cone. This yields a stronger confinement along the out-of-plane direction. The splitting of the spoof SP bands in perforated films is illustrated in Fig. 8, which shows metamaterial predictions for perforated perfect conductor films of three different thicknesses h/d and a dimple size of $a/d = 0.6$. The dispersion relations were obtained from Eq. (12) with $F(h) = \sinh^2(\text{Im}\{k_z\}h)/[\cosh(\text{Im}\{k_z\}h) \pm 1]^2$, where $\text{Im}\{k_z\} = \sqrt{(\pi/a)^2 - k_0^2}$ and the plus-minus symbol corresponds to long- and short-range spoof SPs, respectively (Huidobro *et al.*, 2018).

Here, due to their simplicity and benefiting from the quasianalytical coupled mode theory presented in Sec. II.A, we focus on 2D square arrays of square dimples. Various studies have analyzed the photonic band structure of spoof SPs in other structured planar surfaces with a focus on site or lattice effects. Numerical tools such as finite-difference time-domain (Qiu, 2005), finite-element (Plouin *et al.*, 2006), and boundary-element (de Abajo *et al.*, 2006) methods have been applied to the problem. The flexibility of these approaches allowed a thorough comparison of the spoof plasmon properties in small and large (Chern, Chang, and Chang, 2006), shallow and deep (Popov, Bonod, and Enoch, 2007), open and closed (Stone and Hendry, 2011), and solid and void indentations (Sakai and Tachibana, 2007). Other quasianalytical approaches similar to the coupled mode analysis presented here have been also developed (Collin *et al.*, 2009; Huang, Peng, and Fan, 2010). Slanted corrugations have been also considered, revealing that their nonvertical orientation allows further control over the spoof SP characteristics (Wood *et al.*,

2012; Mercier *et al.*, 2015). Nonsquare lattice geometries such as hexagonal ones (Lan and Chern, 2006) have been also investigated. Effective medium approaches accounting for the finite skin depth of real metals have also been proposed (Collin, Pardo, and Pelouard, 2007) to assess the influence of material loss in spoof SP propagations. All these reports shed further insight into the geometric control of the guiding and EM confinement characteristics of planar spoof SPs.

Although spoof SPs have been studied and utilized mainly in relation to both their propagation characteristics (aiming to create waveguides based on them; see Sec. III) and their associated EM field concentration (with the goal of building up resonators, as described in Sec. IV), these EM modes also play an important role in other physical phenomena. For example, heat transfer at room temperature is largely increased in corrugated metal surfaces supporting spoof SPs in the infrared spectral range with respect to the noncorrugated case (Guérout *et al.*, 2012; Dai, Dyakov, and Yan, 2015, 2016; Dai *et al.*, 2016; Messina *et al.*, 2017).

D. Experimental realization of planar spoof SPs

In this section, we present the two first direct observations of spoof SPs in structured planar surfaces, in the gigahertz and terahertz frequency regimes. We stress that indirect evidence of the excitation of spoof SPs in planar geometries was reported in the context of the so-called extraordinary optical transmission phenomenon (Ebbesen *et al.*, 1998). The resonances appearing in the visible spectrum of periodically perforated thick films were known to be assisted by conventional SPPs. The emergence of similar effects at much lower frequencies, such as millimeter wavelengths where metals behave as quasiperfect electrical conductors (Beruete *et al.*, 2004), was attributed to leaky (radiative) spoof SPs whose frequency lies above the light cone (Garcia-Vidal *et al.*, 2010).

The low-frequency, large–wave vector section of the spoof SP dispersion relation at microwave frequencies was first probed using a traditional scheme for the excitation of conventional SPPs at optical frequencies (Hibbins *et al.*, 2008). Inspired by previous studies for diffractive submillimeter waves (Ulrich and Tacke, 1973), this experiment employed the Otto-like (Otto, 1968) setup sketched in Fig. 9(a). A wax prism was used to couple free-space gigahertz radiation into the bound EM modes, supported by a 15 mm thick perforated brass film under the conditions of frustrated total internal reflection. The refractive index of the prism was 1.5, and the periods and sides of the apertures were $d = 9.53$ mm and $a = 6.96$ mm, respectively. The spoof SP dispersion band on the right-hand side of the panel was obtained by tracking the incident angle (and therefore the parallel wave vector) and frequency of the far-field reflectivity minima (which give the optimum coupling conditions). The empty circles correspond to measurements, which lie below the light cone, indicated by the straight solid line. The metamaterial prediction given by Eq. (12) is rendered by the dashed line, and its correction through the inclusion of diffraction effects is shown as a dotted line. We can observe that both calculations overestimate the binding of the spoof SPs. The large size of the apertures and the small thickness of the sample film required the inclusion of higher-order
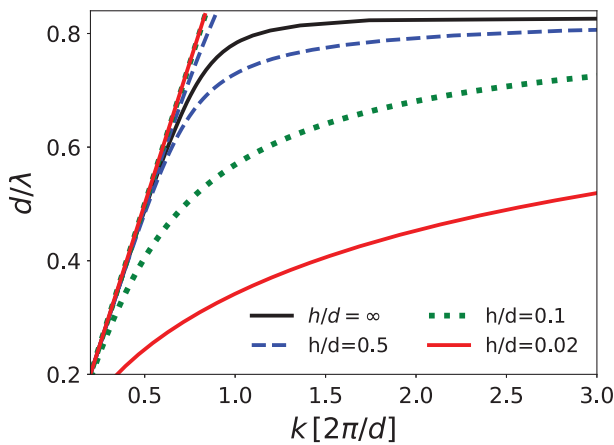

FIG. 8. Spoof SPs in fully perforated perfect conductor films. Dispersion relation for the bound EM modes in films of different thicknesses: $h/d = 0.5$ (blue dashed lines), 0.1 (green dotted lines), and 0.02 (red solid lines). The black solid line plots the spoof SP band for an infinitely thick slab. In all cases, the dimple size is $a/d = 0.6$.
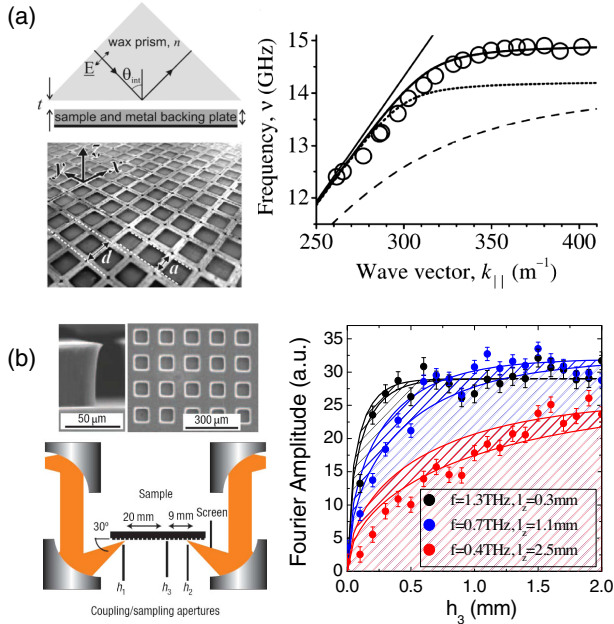
FIG. 9. Experimental verification of spoof SPs in corrugated planar surfaces. (a) Prism coupling of gigahertz radiation to the bound modes sustained by a brass film perforated by millimeter-sized holes. A comparison between the experimental (empty circles) spoof SP band and different theoretical descriptions is depicted. From Hibbins *et al.*, 2008. (b) Aperture coupling of terahertz radiation to the spoof SPs propagating along a copper surface drilled by micrometer-sized dimples. The measured transmitted amplitude (solid circles) vs the intermediate aperture size h_3 for three different frequencies (and L_z values) is shown. Theoretical calculations accounting for the experimental uncertainties are represented as color-shaded areas. From Williams *et al.*, 2008.

waveguide modes (solid line) in order to reproduce the experimental results (Hibbins *et al.*, 2008). The same researchers performed a thorough exploration of the leaky section of the spoof SP dispersion in similar samples (Hibbins, Evans, and Sambles, 2005) and shed light into the key role played by these bound modes in the transmission resonances of holey perfect conductor films (Hibbins *et al.*, 2006). They also reported spoof SP-like modes in ultrathin microwave metamaterials (Hibbins *et al.*, 2004; Lockyear, Hibbins, and Sambles, 2009).

Figure 9(b) illustrates the verification of the presence of tightly confined terahertz spoof SPs decorating drilled metals (Williams *et al.*, 2008). The samples consisted of flat copper surfaces perforated with square arrays of square dimples, the geometry considered in the theory detailed in Sec. II.C. The array period was $d = 100 \ \mu m$ and the dimple dimensions were $a \simeq h \simeq 50 \ \mu m$. In this case, the in- and out-coupling of the spoof SP modes was realized by means of metallic blades, perpendicular to the sample surface and separated from it by only a few microns. The subwavelength dimensions of these blade-sample gaps allowed the excitation of bound EM modes below the light cone. Moreover, a third blade was placed in between, and its distance from the structured copper surface h_3 was used to explore the confinement of the EM waves propagating along it. It also blocked the propagation of

grazing, Zenneck-like waves (Zenneck, 1907) along the sample.

The right-hand side of Fig. 9(b) displays the Fourier transform of the out-coupled terahertz signal detected in the far-field versus h_3 for three different operating frequencies. The legend indicates the theoretical vertical confinement L_z obtained for the experimental conditions. The measurements (solid circles) are in excellent agreement with the theoretical predictions (color-shaded areas) under the simple assumption that the frequency-dependent amplitude of the detected terahertz waves should behave as

$$A(\omega) \propto \sqrt{\int_0^{h_3} e^{-2z/L_z} dz} \propto \sqrt{1 - e^{-2h_3/L_z}}. \qquad (15)$$

Note that Eq. (15) assumes that the blade blocks the spoof SP fields without distorting them significantly. The good agreement between the measurements and Eq. (15) validate this approximation and prove the strong confinement of the spoof SP modes to the sample surface. This is especially evident at high frequencies, where the confinement is strongest and the accordance between theory and experiment is optimum. This study was subsequently extended to annular-shaped holes, revealing the emergence of two different spoof SP bands associated with the two lowest waveguide modes sustained by these apertures (Williams *et al.*, 2010).

III. WAVEGUIDES

In this section, we review a number of structures that exploit spoof SPs to guide low-frequency (microwave and terahertz, mainly) radiation within subwavelength transverse cross section areas.

A. Structured wires: Annular and helicoidal rings

The idea of increasing the propagation characteristics of radio waves through the corrugation of metallic wires was explored in the 1950s (Gobau, 1950; Piefke, 1959). Those works demonstrated that the guiding capabilities of cylindrical wires could be enhanced by texturing periodically their bare surface. Here we overview how the introduction of the spoof SP concept 50 years later boosted those early designs, providing an unprecedented control over the propagation and focusing of EM radiation through textured metallic wires.

Using the coupled mode formalism discussed in Sec. II.A, we can also describe the formation of spoof SPs on perfect conductor corrugated wires (Chen *et al.*, 2006; Maier *et al.*, 2006). The description of periodic cylindrical geometries, like the one sketched in the inset of the top panel of Fig. 10, requires the replacement of the solutions of the Helmholtz equation in Cartesian coordinates with their polar counterparts. We first consider only azimuthally independent modes, which are the lowest in frequency. Expanding the EM fields in p-polarized modes within the unit cell of period d, imposing continuity at $r = R$ (the external wire radius), and projecting the continuity equations over a plane wave basis, we arrive at a set of matching equations on the electric-field modal amplitudes E_α of the form of Eq. (5). Taking advantage of the
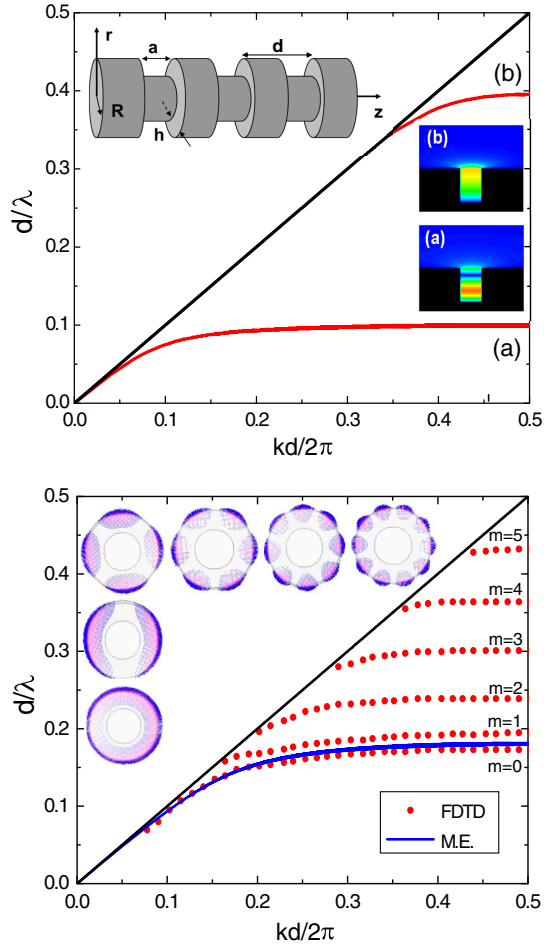
FIG. 10. Top panel: spoof SP dispersion relation for wires of radius $R = 2d$ perforated with rings of width $a = 0.2d$. Azimuthally independent bands for $h = 1.6d$ are also shown. Inset: the corrugated wire geometry. The zr maps show the electric-field amplitudes at $k = \pi/d$. Bottom panel: finite-difference time-domain bands for all azimuthal orders and $h = 0.5d$. The blue line corresponds to the azimuthally independent mode calculated with Eq. (16). Insets: electric-field patterns at the band edge ordered with increasing m from the left bottom corner to the right top corner. From Fernández-Domínguez, Martín-Moreno *et al.*, 2008.

subwavelength character of the corrugations ($\lambda \gg a$, where a is the groove width), we can keep only the lowest (TM$_0$) mode within the rings. This reduces the set of equations to a single one that can be expressed as

$$\sum_n \frac{k_0}{\kappa_n} \frac{K_1(\kappa_n R)}{K_0(\kappa_n R)} S_n^2 = -\frac{J_1(k_0 R) - \gamma_0 N_1(k_0 R)}{J_0(k_0 R) - \gamma_0 N_0(k_0 R)}, \quad (16)$$

where $q_n = k + n(2\pi/d)$ takes into account diffraction effects and n is an integer that runs from $-\infty$ to ∞, $\kappa_n = \sqrt{q_n^2 - k_0^2}$, and $\gamma_0 = J_0[k_0(R - h)]/N_0[k_0(R - h)]$, with k the wave vector of the surface EM mode in the direction of propagation. $J_m(\cdot)$, $N_m(\cdot)$, and $K_m(\cdot)$ are different Bessel functions of the orders of $m = 0$ and 1. The 1D overlapping integrals S_n have the same expression as their planar counterpart: $S_n = \sqrt{a/d}\,\text{sinc}(q_n a/2)$. For $\lambda \gg d$, neglecting the $|n| > 0$

diffraction orders and using the large argument form of the various Bessel functions in Eq. (16), we recover Eq. (11). This agrees with the fact that, as in the planar case, the key parameter governing the binding of the modes is the ring depth h. Note that a similar coupled mode analysis has been developed for the geometry complementary with the inset of the top panel of Fig. 10 and describes the guided modes propagating along a milled dielectric void carved within a metal bulk (Konoplev *et al.*, 2010, 2012; Aghadjani and Mazumder, 2015). Spoof SPs in milled wires encapsulated by a metallic cylindrical shell have been also treated using this formalism (Talebi and Shahabadi, 2010).

The top panel of Fig. 10 plots the azimuthally independent spoof SP dispersion relation obtained from Eq. (16) (Fernández-Domínguez, Williams *et al.*, 2008) for the geometric parameters given in the caption. We observe that two modes are supported by the structure, associated with different radial orders, as illustrated by the electric-field amplitude rz maps in the insets. They are evaluated at the band edge ($k = \pi/d$), where the field confinement is maximum. They show the nonvanishing character of the fields inside the ring for the mode in Fig. 10(a), and an apparent zero along the radial direction in the mode in Fig. 10(b). The bottom panel of Fig. 10 renders the spoof SP bands calculated by finite-difference time-domain simulations for rings shallower than those in the top panel, showing guided modes of all azimuthal orders labeled as m. The insets display electric-field amplitude maps for all m evaluated at the band edge. We observe that the spoof SP of the mth order presents $2m$ nodes along the azimuthal direction. A solid blue line indicates the $m = 0$ band calculated from Eq. (16), which is in excellent agreement with its numerical counterpart.

As discussed in Sec. II, the scalable character of spoof SPs in perfect conductor structures allows for the implementation of waveguiding schemes similar to Fig. 10 in different regimes of the EM spectrum. Much interest has focused on the gigahertz range, where corrugated wires have been used as unit cells in metamaterial structures (Fan *et al.*, 2018). Here, for illustrative purposes, we focus on devices operating in the terahertz regime. They present corrugation dimensions in the range $10 - 100$ μm. Beyond the guiding characteristics of corrugated cylindrical wires, the strong dependence of the spoof SP confinement on the texture geometry can be exploited to achieve focusing and concentration of the terahertz radiation. This is shown in Fig. 11, which illustrates the operation of a tip consisting on a corrugated conical wire whose external radius is gradually decreased along the direction of propagation (Maier *et al.*, 2006; Fernández-Domínguez, Martín-Moreno *et al.*, 2008). The top panel plots the spoof SP bands for cylindrical wires with four different external radii R. We can observe that the dispersion deviates further from the light line for smaller R. Thus, at a fixed frequency the modal wave vector k increases as R decreases. The inset renders the amplitude of the radial component of the electric field E_r as a function of the distance to the wire surface at 0.6 THz for the four structures. Therefore, a larger k (smaller R) yields a stronger field confinement. Note that, normalized to λ, a similar degree of spatial confinement has been reported in millimeter-sized rings at microwave frequencies (Wu, Yang, and Shen, 2009). The larger dimensions of
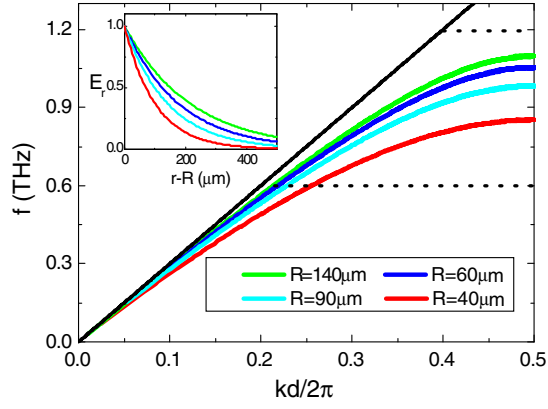
FIG. 11. Top panel: dispersion relation of the guided modes supported by the corrugated wires of four different radii and rings with $d = 100\ \mu m$, $h = 30\ \mu m$, and $a = 50\ \mu m$. Inset: radial component of the electric field vs $r - R$ at 0.6 THz. Bottom panels: electric-field amplitude at 0.6 and 1.2 THz for a 2 mm long corrugated cone whose radius is reduced from 140 to 40 μm. From Fernández-Domínguez, Martín-Moreno *et al.*, 2008.

impact of metallic losses at visible frequencies, similar ideas have been transferred to scanning near-field optical probes (Lotito, Sennhauser, and Hafner, 2010).

Spoof SPs in textured wires have been implemented experimentally at both microwave (Gong *et al.*, 2015; Liu, Li, Gu *et al.*, 2015) and terahertz frequencies (Fernández-Domínguez, Williams *et al.*, 2008; Andrews, 2014). In the following, we discuss the latter, in which the waveguide sample consists of a helically grooved wire; see the inset of Fig. 12(a). The waveguides were formed by tightly wrapping a steel wire of radius 200 μm around a 200 μm radius cylindrical core. Measurements were performed using time-domain terahertz spectroscopy under excitation by a few
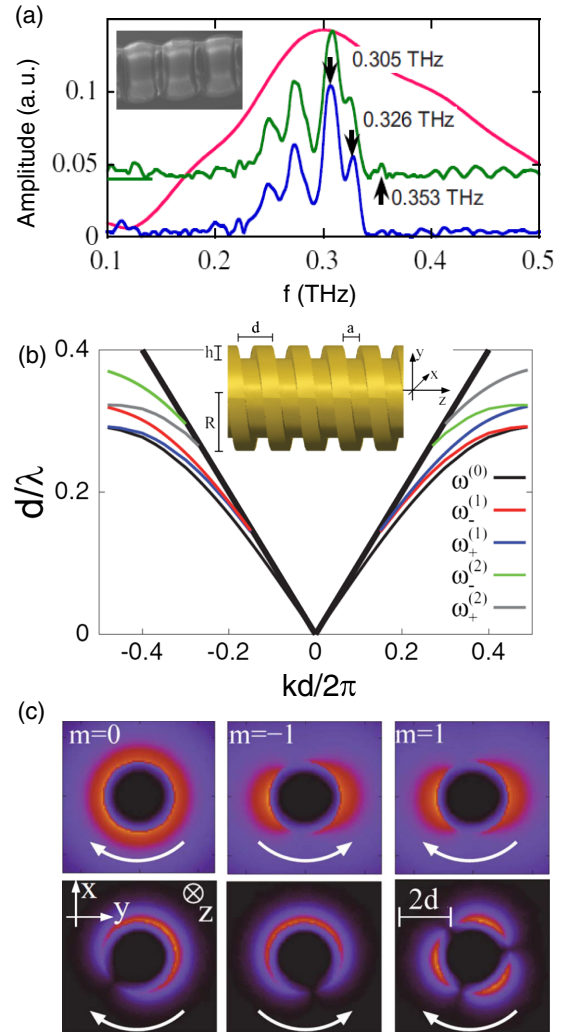

FIG. 12. (a) Experimental transmission spectra for 150 mm long smooth (red line) and (two identical) helically grooved wires (blue and green lines) with $R = d = 400\ \mu m$. Inset: electron micrograph of the experimental sample. From Fernández-Domínguez, Williams *et al.*, 2008. (b) Dispersion relation of the spoof SP modes supported by a perfect conductor wire of radius $R = 600\ \mu m$ inscribed with a helical groove of pitch $d = 400\ \mu m$ ($a = 200\ \mu m$ and $h = 150\ \mu m$). (c) Snapshots of the electric field at the band edge for the three lowest spoof SP modes evaluated at $k = 0.30\pi/d$ (top row) and $k = 0.98\pi/d$ (bottom row). From Rüting *et al.*, 2012.

these devices has made the tailoring of coupling between guided and free-space modes possible through the modulation of the ring depth (Panaretos and Werner, 2016).

The bottom panels of Fig. 11 show electric-field amplitude maps for a 2 mm long conical tip, designed by reducing the external radius of a cylindrical wire gradually from 140 to 40 μm (see top panel). At 0.6 THz (indicated with a horizontal dotted line in the top panel), the guided modes are tightly bounded to the structure even for the smallest radius considered. However, at 1.2 THz guided modes are not supported by wires with $R \leq 140\ \mu m$. This gives rise to guiding and focusing of EM radiation at 0.6 THz, and field scattering into free space at 1.2 THz. The white bars indicate the operating wavelength, revealing that EM energy can be concentrated into deeply subwavelength volumes in this milled conical geometry (Johnson, 2007). The description of terahertz focusing in corrugated metal tips beyond the perfect conductor approximation have demonstrated that the effect of absorption is tolerably small, except for operating wavelengths in the asymptotic region of the spoof SP dispersion relation (Shen *et al.*, 2008). Despite the larger

picosecond pulse. The red line in Fig. 12(a) plots the spectra obtained for an uncorrugated wire. Its broad and dispersionless character reveals the excitation of unbounded Sommerfeld waves in the system (Wang and Mittleman, 2004; Jeon, Zhang, and Grischkowsky, 2005). The blue and green lines render the amplitude versus the frequency for two nominally identical helically grooved wires. Both spectra present well-defined cutoff frequencies at which the transmitted signals decay abruptly. These frequencies are in excellent agreement with the three lowest modal band-edge frequencies $[\omega(k = \pi/d)]$, calculated by means of finite-difference time-domain simulations for the wire geometry. In the following, we analyze in more detail the dispersion relation and modal characteristics of the spoof SPs sustained by helically grooved wires.

Figure 12(b) plots the spoof SP dispersion relation for a helically grooved perfectly conducting wire (see inset) calculated using the finite-element method (Rüting *et al.*, 2012). The geometrical parameters are chosen in accordance with the previously mentioned experimental values. The guided modes present chiral characteristics inherited from the supporting geometry. They can be characterized using two labels (Pendry, 2004): m, which sets the number of azimuthal nodes $(2m)$ that the EM fields present for small values of k, and a sign that depends on the rotation direction along which the mode accumulates phase $+$ $(-)$ for a clockwise (counter-clockwise) rotation with respect to the propagation direction. Note that the spoof SP frequencies are different for positive and negative values of k, i.e., $\omega_{\pm}^{(m)}(k) \neq \omega_{\pm}^{(m)}(-k)$. We can also observe that the relation that holds between bands with different signs is

$$\omega_{\mp}^{(m)}(k) = \omega_{\pm}^{(m)}(-k). \tag{17}$$

Therefore, both the propagation and the rotation direction of the chiral modes must be reversed to keep their frequency fixed. This behavior is not present in either noncorrugated wires or periodic ring arrays, as it is a direct consequence of the underlying helical geometry. Note that Fig. 12(b) shows that, apart from the chiral degeneracy given by Eq. (17), modes with consecutive indices and opposite signs share the same band-edge frequencies: $\omega_{\pm}^{(m)}(\pm\pi/d) = \omega_{\mp}^{(m+1)}(\pm\pi/d)$.

The two chiral spoof SP labels can be combined into a single integer m, now with positive or negative values. This index allows one to write the helical spoof SP fields as (Fernández-Domínguez, Williams *et al.*, 2008)

$$F_m(r, \theta, \xi) = f(r, \xi)e^{i(m + kd/2\pi)\theta}, \tag{18}$$

where r and θ are the radial and azimuthal coordinates and $\xi = z - d\theta/2\pi$ is parallel to the z direction but measured from the surface $z = d\theta/2\pi$. The fields described by Eq. (18) are eigenvectors of the helical translation operator and show that the spoof SP fields along the helical surfaces ($\xi = $ const) evolve in time as $\cos[(m + kd/2\pi)\theta - \omega^{(m)}(k)t]$. This simple expression predicts field profiles whose azimuthal dependence varies along their dispersion band, presenting $2|m|$ nodes along one period at $k = 0$, and $|2m + 1|$ at $k = \pi/d$. This phenomenology is illustrated by the finite-element numerical

calculations presented in Fig. 12(c). It displays the electric-field profiles for modes with $m = 0, \pm 1$. To reveal the chiral character of these modes, the panels show the absolute value of the real part of the electric field averaged along one helical pitch. In accordance with Eq. (18), the field patterns for $m = -1$ and $+1$ are similar for small values of the propagating wave vector ($k = 0.3\pi/d$; top row). On the contrary, close to the band edge ($k = 0.98\pi/d$; bottom row) the modes with $m = 0$ and -1 show the same azimuthal dependence. The local excitation, asymmetric transport behavior, and tunable orbital momentum of spoof SP chiral modes have been demonstrated in finite and more realistic guiding geometries (Rüting *et al.*, 2012; Yao and Zhong, 2015).

B. Corrugated channels, wedges, and domino plasmons

We turn our attention to spoof SP 1D waveguides carved in planar metal surfaces. As a difference with the freestanding cylindrical wires considered in Sec. III.A, these are fully compatible with photonic circuits implementing biosensing or optoelectronic functionalities, as we review in Sec. V. Initial proposals of planar spoof SP waveguides featuring diffraction-limited lateral confinement were formed by local variations of the perfectly periodic lattices analyzed in Sec. II (Maier and Andrews, 2006; Juluri *et al.*, 2009; Kim *et al.*, 2015). Note that dispersionless guiding of gigahertz and terahertz beams in periodic geometries was also reported (Kim *et al.*, 2011). The adiabatic modification of the lattice unit cell along the propagation direction has been exploited to achieve frequency-selective slow-light and EM localization (Fu *et al.*, 2008; Gan *et al.*, 2008; Kim *et al.*, 2015; Guan *et al.*, 2018; Huang *et al.*, 2018), as well as to improve the efficiency and provide directionality to the in- and out-coupling of guided modes and free-space radiation (Gan *et al.*, 2007; Khanikaev *et al.*, 2010; Tang, Ma, and Liu, 2016; Huang *et al.*, 2018). Similar design concepts were also exploited to tailor and harvest visible, terahertz, and microwave beams (Lezec *et al.*, 2002; Martín-Moreno *et al.*, 2003; Lee *et al.*, 2010; Yu *et al.*, 2010).

The first waveguide designs presenting transverse modal shapes in the subwavelength regime consisted of 1D chains of dimples and square or rectangular apertures (Ruan and Qiu, 2007; Zhu, Agrawal, and Nahata, 2008; Shen *et al.*, 2011; Zhu *et al.*, 2011; Pandey, Gupta, and Nahata, 2013). By considering more complex unit cells such as coaxial holes (Williams *et al.*, 2010; Navarro-Cia *et al.*, 2011; Zhang *et al.*, 2011; Yu *et al.*, 2014) and slanted, L-shaped, or tapered grooves (Wood *et al.*, 2012; Li, Jadidi *et al.*, 2013; Xiang *et al.*, 2015; Tian *et al.*, 2016), further control over the spectral and spatial characteristics of these guided modes was achieved. Another design strategy that allows strong transverse confinement to spoof SPs to be provided relies on mimicking geometries exploited in conventional plasmonics (Maier, 2007). Thus, by considering metal films fully perforated by periodic apertures, the spoof SP analog to the so-called long-range SPPs (Berini, 2009) has been conceived (Shen, Catrysse, and Fan, 2005; Wang *et al.*, 2007; Zhang, Shen, and Ran, 2009; Ooi, Okada, and Tanaka, 2011), as noted in Sec. II.

Similarly, by placing two textured metal surfaces next to each other and separated by a small gap, the spoof SP analog

of metal-dielectric-metal waveguides (Economou, 1969) is obtained. The modes sustained by this geometry have been investigated in the gigahertz (Hibbins, Lockyear, and Sambles, 2007; Shin, Barnett, and Luhmann, 2008; Meng *et al.*, 2016; Liu, Sun *et al.*, 2020), terahertz (Zhang *et al.*, 2009; Kats *et al.*, 2011; Lee *et al.*, 2012; Liu, Kong, and Liu, 2016), and visible (Xu, Zhang, and Song, 2013) regimes. The dispersion relation of the spoof SPs propagating between two parallel groove arrays separated by a gap *w* can be calculated using the coupled mode method described in Sec. II.A as (Fernández-Domínguez *et al.*, 2009a)

$$\frac{k_\perp}{k_0} \coth\left(\frac{k_\perp w}{2}\right) = S_k^2 \tan(k_0 t), \qquad (19)$$

where *t* is the depth of the grooves, $k_\perp = \sqrt{k^2 - k_0^2}$, and S_k is the 1D overlapping integral $[S_k = \sqrt{a/d}\,\mathrm{sinc}(ka/2)]$. Notice that in reaching Eq. (19) diffraction effects have been neglected. Figure 13 renders the spoof SP bands for grooves with $t = a = 0.5d$ and *w* between $4d$ (red line) and $0.25d$ (cyan line). The bottom inset displays the electric-field amplitude at the band edge for $w = 1.5d$. Note that by decreasing the gap size the bands lower and, therefore, at a given operating wavelength the spoof SP propagating wave vector increases. This yields a stronger field confinement that can be illustrated by the effective permittivity ($\epsilon_{\mathrm{eff}} = k^2/k_0^2$) rendered in the upper inset ($d/\lambda = 0.25$). This field localization is accompanied by a larger sensitivity to metal absorption losses, which can be quantified by the propagation length $l = 2\mathrm{Im}\{k\}$. The upper inset of Fig. 13 also shows *l* vs w/d at $d/\lambda = 0.25$, calculated numerically for aluminum textured surfaces with $d = 200\ \mu m$. Note that the increase in field confinement and damping associated with smaller *w* shares

many similarities with the phenomenology analyzed in Fig. 11 for conical tips.

Figure 13 anticipates another family of spoof SP waveguides inspired in conventional plasmonic designs. At optical frequencies, V-shaped grooves carved on a metal surface sustain the propagation of channel plasmon polaritons (Novikov and Maradudin, 2002; Bozhevolnyi *et al.*, 2006), thereby presenting a deeply subwavelength modal size. Similarly, the increase in mode confinement with decreasing gap size in parallel groove arrays indicates that confined EM fields can also propagate along corrugated V grooves drilled on the surface of a perfect conductor. These modes, termed spoof channel plasmons, were predicted theoretically (Fernández-Domínguez *et al.*, 2009a), explored in different variations of the original V-shaped waveguide (Gao, Shen, and Zheng, 2012; Li, Jiang *et al.*, 2013; Wu, Wu, Hou *et al.*, 2015), and then verified experimentally at gigahertz frequencies (Jiang *et al.*, 2011; Zhou, Jiang, and Jun Cui, 2011). The beneficial impact that waveguide texturing has in the guiding characteristics of conventional channel plasmons at telecom frequencies has also been addressed theoretically (Nesterov *et al.*, 2010).

The upper inset of Fig. 14(a) sketches a spoof channel plasmon waveguide of period *d*. The main panel plots the dispersion relation for the two lowest guided modes sustained by a textured groove of dimensions given in the figure caption, as calculated with a finite-difference time-domain numerical solver (Fernández-Domínguez *et al.*, 2009a). Both spoof channel plasmons present a finite cutoff frequency at which the dispersion band crosses the light line and the mode becomes leaky; i.e., it radiates into free space. The flat character of the dispersion relation translates into a small spectral overlap between the two modes, which enables the monomode operation of the waveguide. The bottom insets display the longitudinal component of the electric field for the spoof modes in the main panel. The field maps are evaluated at $k = \pi/d$ and within the shallow section of the corrugated V groove, revealing that the modes have opposite parities with respect to the symmetry plane of the structure. The distance between the positions in these insets at which the field amplitude has decayed to one-tenth of its maximum value can be taken as a measure of the field confinement. This yields subwavelength modal sizes for both guided modes at the band edge: 0.52λ and 1.06λ for the first and second modes, respectively.

Figure 14(b) analyzes the guiding of terahertz radiation through the lowest spoof channel plasmon in Fig. 14(a) for $d = 200\ \mu m$. The transmission for a 20 mm long straight waveguide (black squares) is compared to 90° bends of the same length and a different curvature radius *r*. The red vertical arrows correspond to the cutoff and band-edge frequencies of the mode; between them the transmission is close to 1. The transmission decreases for bent structures with smaller *r*: more significantly so at low frequencies, where spoof channel plasmons are more sensitive to radiative losses. Note that the transmission remains much larger than the values reported for weakly bounded terahertz Sommerfeld waves in metallic wires (Wang and Mittleman, 2004). The inset shows the electric-field amplitude above the metal surface for the
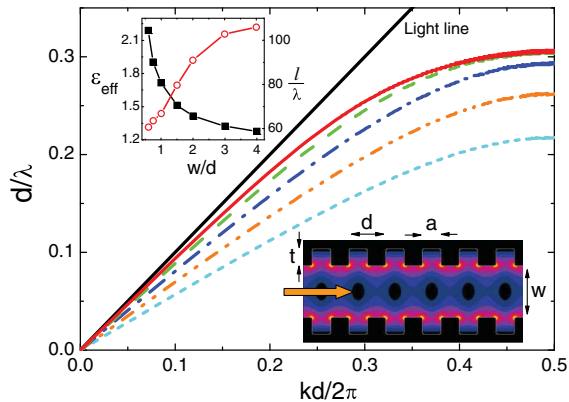

FIG. 13. Dispersion relation of the guided EM modes between two groove arrays of period *d* perforated on perfect conductors. The grooves' width and depth are $a = t = 0.5d$. Five different gap widths (*w*) are considered: $4d$ (red solid line), $2d$ (green dashed line), *d* (blue dot-dashed line), $0.5d$ (orange double dot-dashed line), and $0.25d$ (cyan dotted line). Lower inset: electric-field amplitude at the band edge for $w = 1.5d$. Upper inset: the effective permittivity (black squares) and propagation length (red circles) at $d/\lambda = 0.25$ for Al and $d = 200\ \mu m$. From Fernández-Domínguez *et al.*, 2009a.
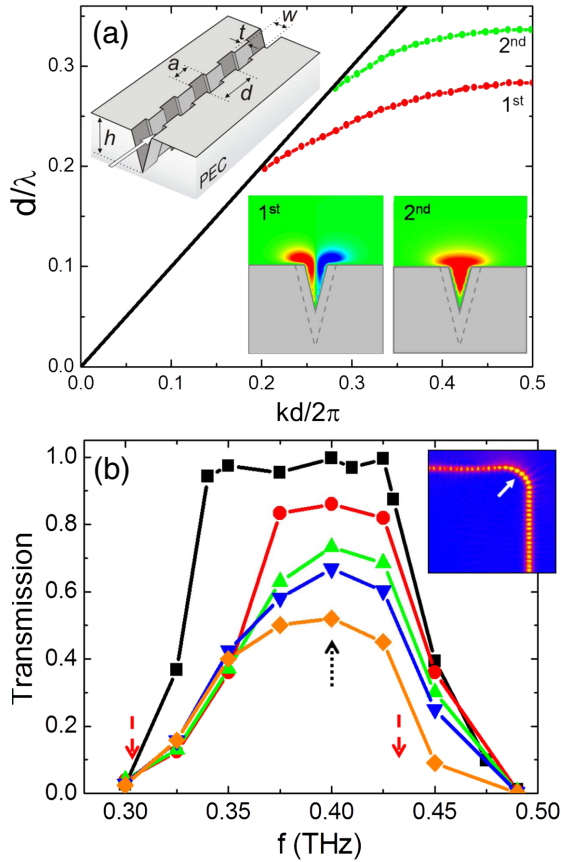
FIG. 14. (a) Dispersion relation of the two lowest spoof channel plasmons. Upper inset: sketch of the waveguide ($a = t = 0.5d$, $w = 0.76d$, and $h = 5d$). Lower inset: longitudinal component of the electric field at the band edge for both modes. (b) Transmission spectra for 20 mm long, $d = 200 \ \mu m$ spoof channel plasmon straight (black squares) and 90° bent waveguides with different curvature radii r: 10 (red circles), 4.5 (green triangles), 2.9 (blue inverted triangles), and 1.5 mm (orange rhombuses). Red arrows indicate the cutoff and band-edge frequencies. Inset: the electric-field amplitude above the planar surface evaluated at 0.4 THz and $r = 2\lambda = 1.5$ mm (indicated with the black arrow in the main panel). From Fernández-Domínguez *et al.*, 2009a.

FIG. 15. Dispersion relation of spoof wedge plasmons supported by textured wedges of different angles: θ ($a = t = 0.5d$ and $h = 5d$). The dashed black line plots the dispersion for a flat, $\theta = 180°$ groove array. Inset: the waveguide geometry. The right panels display the electric-field amplitude at $k = \pi/d$ for (a) $\theta = 60°$ and (b) $\theta = 20°$. From Fernández-Domínguez *et al.*, 2009b.

waveguide with $r = 2\lambda = 1.5$ mm (indicated with a vertical black line in the main panel).

For conventional channel plasmons propagating in deep grooves, the EM field is highly concentrated at the bottom of the grooves (Gramotnev and Bozhevolnyi, 2010). However, for shallow grooves the EM modes are guided mainly along its edges (Pile and Gramotnev, 2004; Moreno *et al.*, 2006). This is because guided EM modes result from the hybridization of purely channel plasmons and another set of guided modes, the so-called wedge plasmon polaritons (Pile *et al.*, 2005; Boltasseva *et al.*, 2008; Moreno *et al.*, 2008). The electric-field distribution in Fig. 14(a) reveals that, for this set of geometrical parameters, the EM modes supported by corrugated V grooves are also concentrated at the edges, implying that spoof channel plasmons must be hybridized with the spoof analog of wedge plasmon polaritons (referred to as
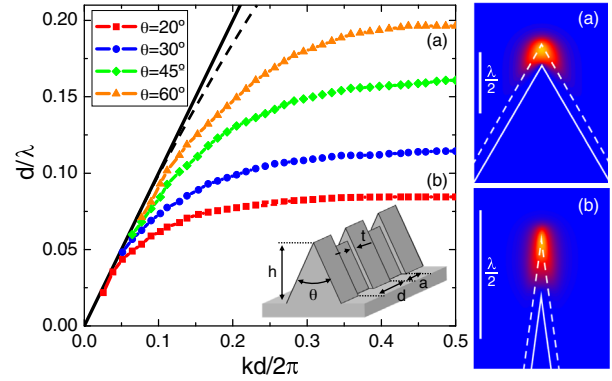
spoof wedge plasmons from now on) (Fernández-Domínguez *et al.*, 2009b; Gao, Zhang, and Shen, 2010).

Figure 15 plots the dispersion relation of these spoof wedge plasmons and the inset shows a schematic representation of the supporting geometry, a corrugated wedge on top of a flat metallic surface. Spoof wedge plasmon bands for four different θ's (color dots) are compared to spoof SPs in a flat surface (dashed black line). All the structures present the same corrugation geometry as the V grooves in Fig. 14. Like spoof channel plasmons, spoof wedge plasmon bands present a cutoff frequency, below which the modes lose their non-radiative character. We observe that reducing the wedge angle lowers the dispersion bands, and hence increases the mode confinement. This is illustrated by the band-edge amplitude field maps in the right panels. The modal size (defined in a manner similar to the channel case) is 0.78λ for $\theta = 60°$ and reduces down to 0.28λ for $\theta = 20°$. Note that the last geometry can be directly compared to the spoof channel plasmons in Fig. 14(a), as the channel angle in that case was also 20°, which shows that the EM field confinement capabilities of wedge-shaped geometries is significantly higher. This fact has been exploited for the realization of frequency-selective flat focusing tips based on terahertz spoof wedge plasmons (Fernández-Domínguez *et al.*, 2009b).

A similar type of spoof SP modes are the so-called domino plasmons (Martin-Cano *et al.*, 2010). These are sustained with a simple structure reminiscent of domino pieces: a 1D array of parallelepipeds sitting on top of a surface. Again, this geometry can be considered the low-frequency version of a noble metal nanoparticle waveguide, which have been thoroughly explored in the optical regime (Krenn *et al.*, 1999; Maier *et al.*, 2003). The waveguide, which is characterized by four geometrical parameters (period d, height h, spacing a, and lateral width L), is sketched in the inset of Fig. 16(a). The main panel reveals the reason behind the interest gathered around these guided modes. It plots the dispersion relation of the domino plasmon modes for $a = L = 0.5d$ and two different heights $0.75d$ (blue line) and $1.5d$ (black and gray
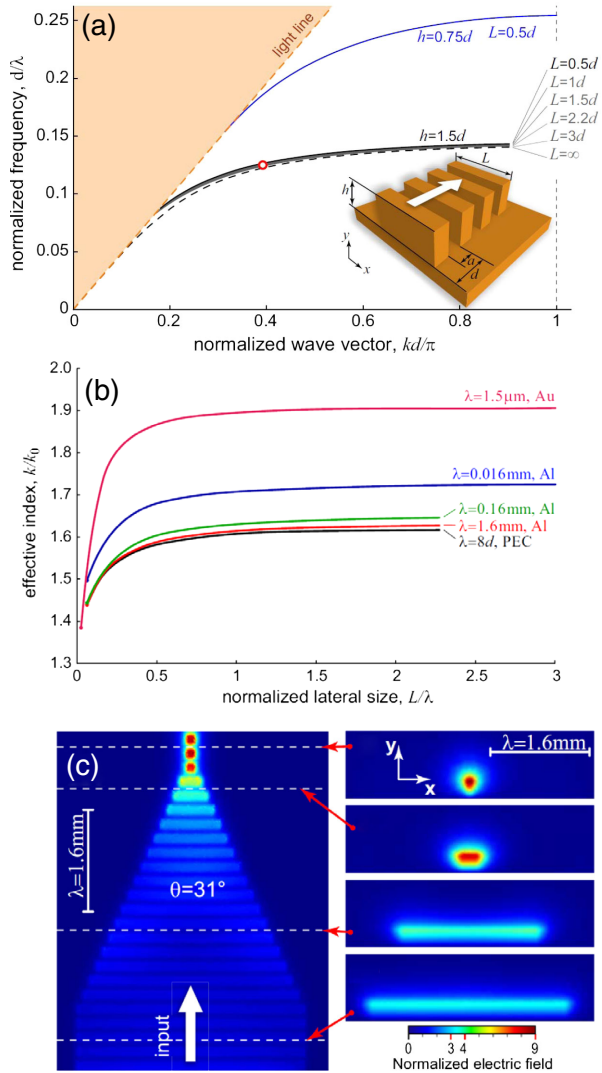
FIG. 16. (a) Dispersion relation of domino plasmons with $a = 0.5d$ and various lateral widths L. The black and gray (blue) lines correspond to height $h = 1.5d$ ($h = 0.75d$). The dashed line corresponds to an infinitely wide groove array ($L \to \infty$). Inset: the domino geometry. (b) Effective mode index vs L in real metal dominoes with different wavelength regimes and $d = 0.125\lambda$. (c) Modulus of the Poynting vector distribution slightly above a tapered terahertz domino structure ($L_{\mathrm{in}} = 16d$, $L_{\mathrm{out}} = 0.5d$, $h = 1.5d$, $d = 200\ \mu m$, and $\lambda = 1.6$ mm). Right panels: transverse cuts at the locations indicated with white dashed lines in the main panel. From Martin-Cano *et al.*, 2010.

lines). In a manner similar to that described in Sec. II for infinitely long groove arrays, h controls the binding of the domino plasmons: the deeper the parallelepipeds, the more confined their EM fields are. Indeed, the black dashed line renders the spoof SP band for a grove array with $h = 1.5d$, demonstrating a noteworthy accordance with the corresponding domino plasmon, except in the vicinity of the light line, where the latter presents a cutoff frequency. The gray lines plot the dispersion relation for larger L, and all virtually overlap with the subwavelength configuration ($L = 0.5d$). Thus, the guiding characteristics of domino plasmons are independent

of the lateral dimension of the waveguide sustaining them, even in the subwavelength regime.

Figure 16(b) analyzes in more detail the sensitivity of the transverse confinement of domino plasmon modes to the parallelepiped's lateral dimension, not only for perfect conductor structures but also for real metals in different (terahertz and telecom) frequency regimes. The figure plots the modal effective index ($n_{\mathrm{eff}} = \sqrt{\epsilon_{\mathrm{eff}}} = k/k_0$) versus L/λ for waveguides with periodicity d ranging 3 orders of magnitude ($a = 0.5d$ and $h = 1.5d$). The curves for a perfect conductor (black line) and Al at $\lambda = 1.6$ mm (red line) are, as expected, almost identical. They show that n_{eff} varies by only 12% from infinitely long grooves to $L = 0.5d = \lambda/16$. The green and blue lines correspond to Al dominoes at $\lambda = 0.16$ and 0.016 mm, which were obtained by reducing d by factors of 10 and 100, respectively. We observe that the binding of the domino plasmon increases thanks to the finite skin depth of Al, which allows the EM field penetration into the parallelepipeds and the substrate. Note that this is accompanied by a higher impact of metal absorption in the mode propagation length. The variation in n_{eff} is slightly larger in these cases, up to 15%. The magenta line plots the effective index for Au waveguides operating at 1.6 μm. In this case, both EM field confinement and its sensitivity to L are stronger (38%).

Figure 16(c) displays a simple guiding scheme that exploits the insensitivity of microwave domino plasmons to the lateral width: a tapered waveguide (Martin-Cano *et al.*, 2010). The left panel shows a top view of the power propagation along a domino chain where L is varied from $16d$ to $0.5d$ along only 16 periods (only twice the operating wavelength). Finite-element simulations indicated that the back reflection in this device is smaller than 2%, and only 5% of the incoming power is scattered into free-space radiation, greatly outperforming the spoof SP designs based on cylindrical and wedge geometries. The right panels are cross sections at different positions along the taper illustrating the process of field concentration. The panels show the uniform character of the EM fields between adjacent metallic elements. The boundary conditions at the laterally open gaps are more akin to perfect magnetic walls, and the corresponding electric fields are approximately constant, even when $L \to 0$. This lack of spatial structure in the confined fields is the origin of the insensitivity of the dispersion relation of the domino plasmon on the waveguide lateral dimensions.

Other devices such as power dividers, directional couplers, and ring resonators have also theoretically been proposed. Sophisticated variations of the domino geometry, such as L-shaped (Martín-Cano *et al.*, 2011), T-shaped (Gupta, Pandey, and Nahata, 2014), and U-shaped (Wu, Wu, Shen *et al.*, 2015) protrusions have been also explored. Structural dispersion has been proposed as a means of increasing domino plasmon binding and confinement (Zhang *et al.*, 2021). The notable guiding capabilities of domino plasmons have been proven experimentally at gigahertz frequencies (Zhao *et al.*, 2010; Brock, Hendry, and Hibbins, 2011; Gao *et al.*, 2012), and functionalities such as splitters, filters, and resonators (Ma *et al.*, 2011; Guan *et al.*, 2017; Qi, Liao, and Xue, 2018), as well as in- and out-coupling devices (Liu, Li, Xu *et al.*, 2015; Liu *et al.*, 2017; Yuan *et al.*, 2020), were realized. Even

topological networks based on domino plasmons were fabricated (Gao *et al.*, 2016; Gao, Yang *et al.*, 2017). Finally, the existence of domino plasmons in the terahertz regime has been also verified experimentally (Kumar *et al.*, 2013; Zhang, Xu *et al.*, 2018).

C. Ultrathin and conformal surface plasmons

As discussed in Sec. II, before the discovery of domino plasmons and their insensitivity to waveguide thickness, surface EM modes supported by ultrathin structures were explored in the context of the so-called high impedance surfaces (Sievenpiper *et al.*, 1999). Generally, these designs consist of two connected or disconnected perforated thin metal films separated by a dielectric layer. In these structures, the EM-induced capacitive and inductive currents between the films are exploited to yield large efficient surface impedances and strong field confinement in complex geometries, such as Sievenpiper mushrooms or complementary split-ring resonators (Lockyear, Hibbins, and Sambles, 2009; Navarro-Cia *et al.*, 2009; Yang *et al.*, 2015, 2017; Fan *et al.*, 2018; Popov *et al.*, 2019). Similar architectures were explored subsequently in the context of planar metamaterial surfaces with tailored reflection and transmission properties (Zhou and Chan, 2004; Hao, Zhou, and Chan, 2007; Luukkonen *et al.*, 2008) and for efficient far- to near-field coupling devices (Sun *et al.*, 2016; Duan *et al.*, 2017).

By pushing the width insensitivity of domino plasmons to its ultimate limits, a different spoof SP–like strategy to realize surface EM modes propagating in ultrathin metallic structures was conceived. As a difference from the aforementioned proposals, the supporting structure, illustrated in the inset of Fig. 17(a), involves a single metal strip with near-zero thickness. The parameters defining the comb-shaped geometry are also indicated, the width W, period d, and the groove depth and width h and a, all of which are much larger than the waveguide thickness t (note the similarity to domino chains, rotated 90° around the z axis). The mechanical flexibility of this platform and the tightly bound character of the associated EM fields are behind the term coined for this type of spoof SP,

usually known as conformal surface plasmons (Shen *et al.*, 2013). The main panel plots the dispersion relation of conformal surface plasmons for different t ($W = d$ and $h = 2a = 0.8d$). As happened with the domino plasmons (see Fig. 16), conformal surface plasmon frequencies are only slightly dependent on the waveguide thickness. For $t \to \infty$, the corresponding band is that of the 1D array of grooves discussed in Sec. II. This curve overlaps with the dispersion for $t = 20d$. When the thickness is reduced to 4 orders of magnitude, the modal frequency is lowered by only ~4%. The dashed lines correspond to the long- and short-range conformal surface plasmon modes that emerge when both sides of the ultrathin metal strip, instead of just one, are decorated with grooves.

Figure 17(b) proves that conformal surface plasmon modes emerge in comb-shaped ultrathin strips described beyond the perfect conductor approximation. They emerge in finite-element calculations for copper at various spectral ranges, from the gigahertz to the midinfrared, and $t = 0.02d$. We can observe that the normalized dispersion relation (at different spectral ranges) is insensitive to the scaling of the period d. On the contrary, the inset shows that the impact of copper absorption increases significantly at a higher operating frequency, and therefore the propagation length (normalized to λ) is strongly reduced. Figure 17(c) renders the magnetic field (white arrows) and z component of the Poynting vector (color scale) evaluated at two x-y planes within the waveguide period. The yellow ellipses indicate the area (of size ~0.44λ) within which 70% of the power flux is contained. These field maps show that EM energy is highly localized within the comb-shaped metal structure. Moreover, it also reveals that the mechanism behind this tight modal confinement is the magnetic field circulation enabled by the free-standing and ultrathin character of the underlying structure (Shen *et al.*, 2013). The extraordinary guiding capabilities of conformal surface plasmons have been thoroughly investigated in recent years in the gigahertz and terahertz frequency regimes. Several functional devices based on these capabilities are presented in Sec. V.
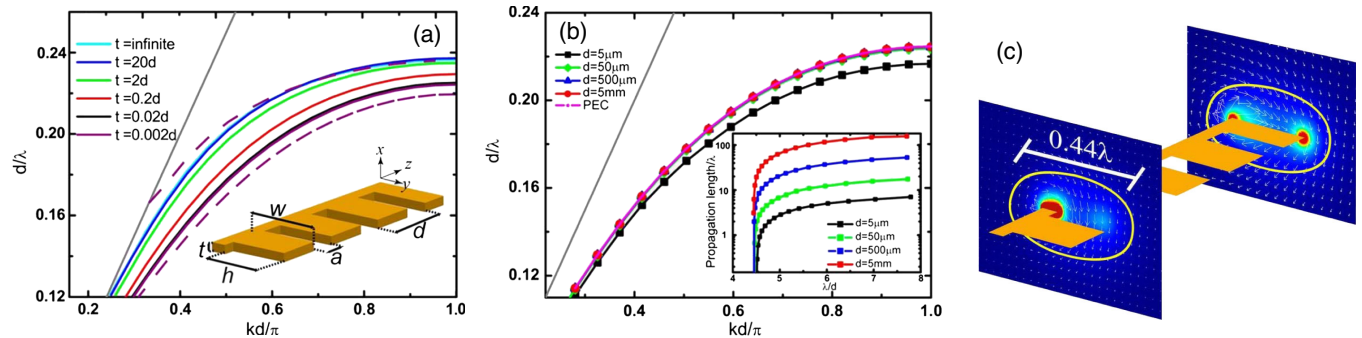

FIG. 17. (a) Dispersion relation (solid lines) of conformal surface plasmons as a function of the waveguide thickness t. Inset: the supporting comb-shaped geometry ($w = d$, $a = 0.4d$, and $h = 0.8d$). The two dashed lines correspond to a double-comb structure with $t = 0.02d$. (b) Bands for different values of period d for copper waveguides ($t = 0.02d$). Inset: propagation length of the modes in the main panel. (c) Power flow (contour plot) and magnetic field (vector map) within two transverse x-y planes along the structure. The color scale ranges from dark blue (lowest intensity) to red (highest intensity), and the length of the white arrows weight the magnetic field amplitude. The modal size is indicated by the yellow ellipses. The geometric parameters are the same as in (b) for $d = 5$ mm ($\lambda = 30$ mm). From Shen *et al.*, 2013.

IV. RESONATORS

Surface plasmon resonances also arise in metal particles with closed surfaces (Kreibig and Vollmer, 1995). When light impinges on a metallic particle, the electron gas in the metal gets polarized, with polarization charges localized at the surface. As a consequence, a restoring force emerges and originates plasmon oscillations that are confined at the surface of the metal particle, resulting in a large EM field confinement on the subwavelength scale. These EM resonances emerge in the optical range of the EM spectrum and are called localized surface plasmon (LSP) modes. Taking advantage of their EM field confinement, LSPs have been widely used in near-field optics (Novotny and Hecht, 2006), in surface-enhanced Raman spectroscopy (García-Vidal and Pendry, 1996; Anker *et al.*, 2008), as optical antennas (Novotny and van Hulst, 2011), in photovoltaics (Atwater and Polman, 2010), and for enhancing nonlinear processes (Bouhelier *et al.*, 2003).

Whereas previously in this review we focused on spoof SPs that propagate both along periodically perforated planar geometries and in a variety of structured waveguide configurations, here we discuss how textured metal particles of closed surfaces can also support the localized version of spoof surface plasmons, the so-called spoof LSPs. These EM modes mimic the properties of optical LSPs and have already been utilized to transfer their capabilities and potentialities to lower frequency regimes such as the terahertz and microwave ranges.

A. Spoof localized surface plasmons

The simplest structure in which spoof LSPs emerge is an infinitely long corrugated cylinder made of a perfect conductor, as sketched in Fig. 18(a). The 2D structure consists of a circle of radius R corrugated with a periodic array (period $d = 2\pi R/N$) of N grooves. The grooves have width a and depth h, with $r = R - h$ the radius of the inner core. The number of grooves and the radius of the cylinder are chosen to yield $d \ll \lambda_0$ (λ_0 is the wavelength of the incident wave).
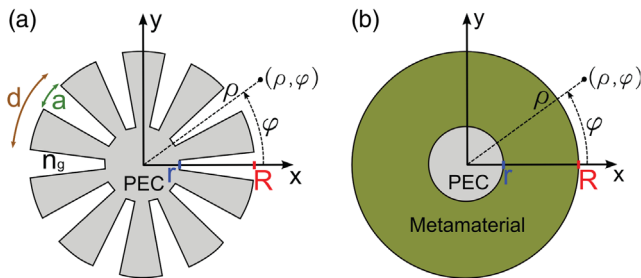

FIG. 18.   (a) A 2D corrugated perfect conductor cylinder (invariant along the z direction) is illuminated with a wave polarized with the magnetic field along the cylinder's axis ($\mathbf{H} = H\mathbf{u}_z$). The geometrical parameters defining the structure are radius R, periodicity d, groove depth h, and groove width a. The grooves may be filled with a dielectric material of refractive index n_g. (b) In the effective medium approximation, the geometry displayed in (a) behaves as an inhomogeneous and anisotropic layer of thickness h surrounding the inner cylinder. From Pors *et al.*, 2012.

The grooves could be filled with a dielectric material of refractive index n_g, and the surrounding medium is assumed to be air. From now on, the outer radius R is used as the unit length, as the resonance frequencies scale with the reciprocal size of the structure within the perfect conductor approximation, as previously discussed.

To search for the EM resonances of this 2D structure, a TM-polarized incident plane wave ($\vec{H}$ pointing along the z direction) propagating along the y axis can be used as a probe. Within the perfect conductor limit, the EM response of particles is conveniently quantified by the scattering cross section. In Fig. 19(b) (solid line) we present this magnitude as a function of frequency for a representative textured cylinder calculated using a finite-element framework (Pors *et al.*, 2012). The cross section is normalized to the diameter $2R$, whereas the frequency is normalized to the asymptote frequency ω_a of the fundamental spoof SP mode that would propagate on a 1D periodically textured flat surface with similar grooves ($\omega_a \approx \pi c/2hn_g$), as previously discussed.
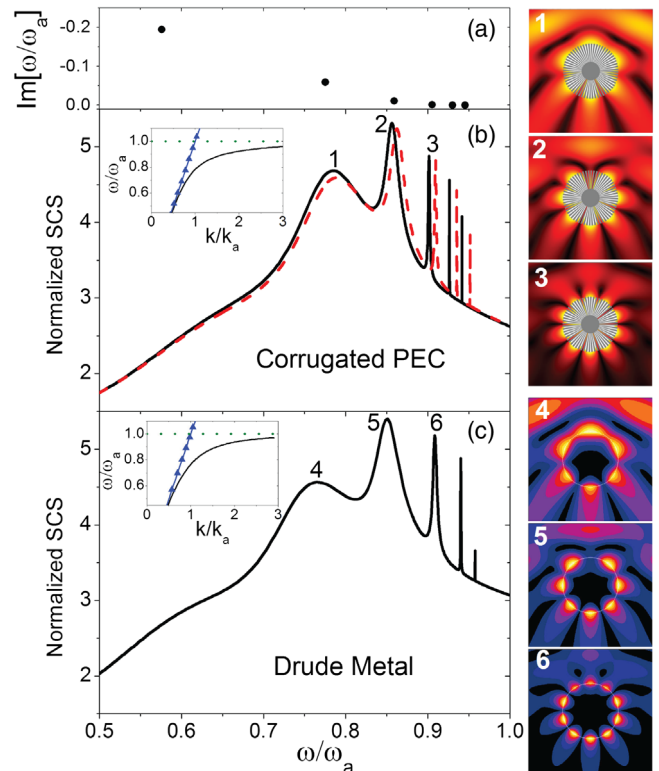

FIG. 19.   A textured perfect conductor cylinder ($r = 0.33R$, $N = 60$, $a = 0.4d$, $n_g = 1$, and $\omega_a R = 0.89\pi c$) mimics the response of a Drude metal cylinder in the optical regime. (a) Complex resonance frequencies found using the analytical method [Eq. (21)]. (b) Numerically computed scattering cross section (solid line) for the textured perfect conductor cylinder. The dashed line in (b) corresponds to the calculation in the metamaterial approximation. Inset: dispersion relation of the corresponding spoof SP. (c) The same magnitude for a Drude metal cylinder of radius R with $\omega_p = \sqrt{2}\omega_a$ and the same ω_a value as in (b). Inset: dispersion relation for SPPs propagating along a Drude metal surface. Right panels: the absolute H field at the hexapole, octopole, and decapole resonances for the two systems. From Pors *et al.*, 2012.

The inset of Fig. 19(b) shows the dispersion relation of these spoof SPs (solid line) and the free-space light dispersion (triangular dotted line) in normalized units ($k_a = \omega_a/c$). The multiple peaks that show up in the spectrum correspond to the EM modes supported by the corrugated perfect conductor cylinder, which share strong similarities with optical LSPs supported by metal cylinders. This statement can be further reinforced by comparing the scattering cross section spectrum in Fig. 19(b) to that of an uncorrugated metallic cylinder with Drude permittivity,

$$\epsilon_m(\omega) = 1 - \frac{\omega_p^2}{\omega^2}, \qquad (20)$$

as depicted in Fig. 19(c). For a quantitative comparison between perfect and Drude metals, Ohmic losses in the Drude response have been neglected and the plasma frequency ω_p has been chosen to yield the same $\omega_a R$ value as for the corrugated perfect conductor cylinder case ($\omega_p = \sqrt{2}\omega_a$). Despite the different structures and frequency regimes, a corrugated cylinder is able to mimic the plasmonic response of a Drude metal cylinder, both in the spectral locations and linewidths of the resonances and in their corresponding cross section magnitudes. The analogy between the two structures is further exemplified in the right panels of Fig. 19, which display the field amplitude (H_z) for three higher-order modes that appear in the scattering spectrum (hexapole, octopole, and decapole resonances) in both cases. The comparison illustrates how geometry in a perfect conductor particle can indeed mimic the EM response of a real metal, which in turn is ultimately determined by the collective response of its free electrons.

A good asset of this 2D case is that it is possible to derive an analytical transcendental equation for the resonance condition of its spoof LSPs following the steps of the coupled mode method, similar to that described before when we analyzed propagating spoof SPs. The transcendental equation for the spoof LSP mode of the order of n reads [details of the derivation were given by Pors *et al.* (2012)]

$$S_n^2 \frac{H_n^{(1)}(k_0 R)}{H_n^{(1)'}(k_0 R)} \frac{f}{g} = n_g, \qquad (21)$$

where $H_n^{(1)}$ is the Hankel function of the first kind and of the order of n (the prime indicates differentiation with respect to the argument in parenthesis), k_0 is the wave number in air, $f = J_1(k_0 n_g r)Y_1(k_0 n_g R) - J_1(k_0 n_g R)Y_1(k_0 n_g r)$ and $g = J_0(k_0 n_g R)Y_1(k_0 n_g r) - J_1(k_0 n_g r)Y_0(k_0 n_g R)$, where J_0 and J_1 (Y_0 and Y_1) are the zeroth- and first-order Bessel functions of the first (second) kind, respectively, and S_n is given by $S_n = \sqrt{a/d}\text{sinc}(na/2R)$. For subwavelength texturing ($a \ll R$), its expression reduces to $S_n \approx \sqrt{a/d}$. Physically, the picture that emerges from this equation regarding the emerging spoof LSP modes is that of surface EM modes running around the cylinder surface, with each resonance appearing when an integer number of modal wavelengths fits into the perimeter. Based on the modal expansion of the EM fields, the following analytical expression for the normalized scattering cross section can be also derived:

$$\sigma = \frac{2}{k_0 R} \sum_{n=-\infty}^{\infty} |a_n|^2, \qquad (22)$$

where the coefficient a_n for each mode n is given by

$$a_n = -i^n \frac{(a/d)J_n(k_0 R)f - n_g J_n'(k_0 R)g}{(a/d)H_n^{(1)}(k_0 R)f - n_g H_n^{(1)'}(k_0 R)g}. \qquad (23)$$

In addition, we can separate the contribution of each mode as follows:

$$\sigma_0 = \frac{2}{k_0 R}|a_0|^2, \qquad \sigma_n = 2\frac{2}{k_0 R}|a_n|^2 \quad (n \neq 0). \qquad (24)$$

Figure 19(a) shows the resonance frequencies calculated with the coupled mode method in the complex plane. Each resonance frequency corresponds to the solution of Eq. (21) for a different order n. In addition, Fig. 19(b) (dashed line) renders the scattering cross section of the corrugated perfect conductor cylinder under the incidence of a TM plane wave calculated using Eq. (22). The predictions of the analytical model are in good agreement with the full numerical results (solid line). For each pole in the complex frequency plane, a resonance appears in the scattering spectrum. Notice that resonances with frequencies with a large imaginary part are only barely apparent in the spectrum, as in the case of the dipolar and quadrupolar modes. However, resonances with frequencies that lie closer to the real frequency axis, such as the hexapole, octopole, and decapole resonances highlighted in Fig. 19(b), lead to discernible sharp peaks in the scattering spectrum.

It is worth developing a complementary way to look into the physics of the spoof LSPs by applying the concept of EM metamaterials, as done in the case of planar surfaces. As the perfect conductor cylinder is textured on a subwavelength scale ($d \ll \lambda_0$), it is expected that the region with grooves could be interpreted as an effective medium of thickness h, as illustrated in Fig. 18(b). The effective parameters can be deduced from the following line of thought. As the perfect conductor boundary condition within the subwavelength radial grooves forces $E_\rho = E_z = 0$ and $H_\varphi = 0$, $\epsilon_\rho = \epsilon_z = -\infty$ and $\mu_\varphi = \infty$. By averaging $1/\epsilon$ in the φ direction, we obtain $\epsilon_\varphi = n_g^2 d/a$. As light propagates in the grooves in the ρ or z direction with the velocity c/n_g, the effective material must satisfy the equation $\sqrt{\epsilon_\varphi \mu_z} = \sqrt{\epsilon_\varphi \mu_\rho} = n_g$, which leads to $\mu_\rho = \mu_z = a/d$. Note that in Cartesian coordinates these effective parameters transform to permittivity and permeability tensors with off-diagonal elements and elements that depend on the (x, y) coordinates. In other words, within the metamaterial approximation the region containing subwavelength grooves behaves as an anisotropic but also inhomogeneous layer with both electric and magnetic properties.

When going from an infinitely long 2D corrugated cylinder to a more realistic 3D corrugated disk [see Fig. 20(a), spoof LSP modes are still supported, as first reported in a combined theoretical-experimental work performed in the microwave regime (Shen and Cui, 2014). Figure 20(b) illustrates the evolution of the spoof LSP modes by analyzing how the
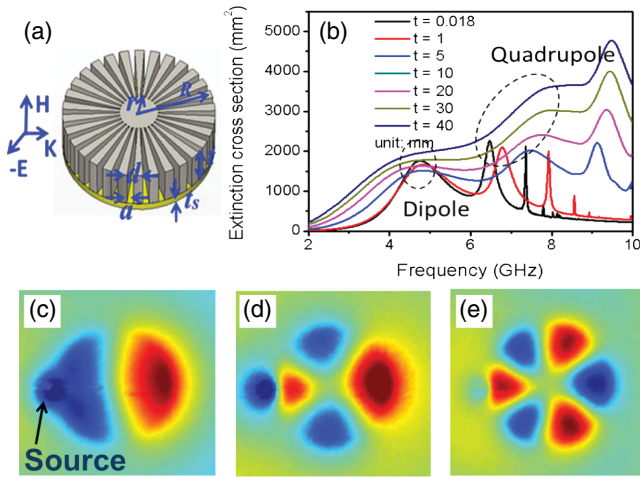
FIG. 20. (a) A 3D textured metallic disk with inner and outer radii r and R, respectively, placed on top of a thin dielectric substrate (yellow area) with thickness t_s. In the numerical calculations rendered in (b), the thickness of the metallic disk (t) is varied from infinity to nearly zero. (b) Extinction cross section spectra of textured metallic disks with different thicknesses ($t = 0.018, 5, 10, 20, 30$, and 40 mm), in which redshifts of resonance frequencies are observed when t decreases. The rest of the geometrical parameters are $t_s = 0.4$ mm, $R = 10$ mm, $r = 0.25R$, $a = 0.4d$, and $N = 60$. (c)–(e) Near-field patterns associated with the z component of the E field, measured on a plane 0.5 mm above a textured metallic disk of thickness $t = 0.018$ mm, for the dipole mode at 4.52 GHz, quadrupole mode at 6.24 GHz, and hexapole mode at 7.28 GHz. The geometrical parameters correspond to those in (b). From Shen and Cui, 2014.

calculated extinction cross section spectrum changes when the metallic disk thickness t is varied. The quality factor of the resonances largely increases when t is decreased. This explains why the dipolar and quadrupolar resonances, which do not show up in the 2D case [as shown in Fig. 19(b)], now clearly emerge in the extinction spectrum. In addition, the resonance frequencies redshift as the thickness decreases. This shift is larger for spoof LSP resonances of higher n, while the spectral location of the dipole mode is almost maintained in this evolution. The existence of these spoof LSP modes for the case of ultrathin metallic disks ($t = 0.018$ mm) was also experimentally verified using a near-field probe (Shen and Cui, 2014). Figures 20(c)–20(e) show the experimental results of the near electric-field distributions of the multipolar spoof LSPs, corresponding to the dipole, quadrupole, and hexapole modes, respectively. An interesting addition to these corrugated structures is the incorporation of a ground plane, as demonstrated by Gao, Gao, Shi *et al.* (2015) for the case of ultrathin metallic disks. This ground plane allows the dispersion of the spoof LSP modes to be effectively tuned and is also able to enhance the quality factors of the corresponding resonances.

One-dimensional grooves of depth h and filled with a material with refractive index n_g possess different cavity resonances with frequencies $\omega_a^m \approx m\pi c/2hn_g$, where m is an integer. This fact means that spoof LSP modes supported

by either corrugated 2D cylinders or 3D disks could present a multiband behavior, each spoof LSP band associated with a different value of m. Unlike the previously discussed case, which corresponds to $m = 1$, spoof LSP modes originating from bands with $m > 1$ display a radial dependence, as predicted and experimentally verified by Liao *et al.* (2015). An alternative way to create multiband spoof LSP modes but relying only on the fundamental groove mode ($m = 1$) is to use multiple groove depths, as determined by Li, Liu *et al.* (2014). The possibility of using spoof LSP modes with multiband characteristics could be exploited in the design of resonators able to operate efficiently in a broadband frequency range in both the microwave and terahertz regimes.

The use of geometry to generate spoof LSP modes is not restricted to structures based on cylinders or disks corrugated with radial grooves. A fan-shaped ultrathin metallic strip, such as the one shown in Fig. 21(a), also supports spoof LSP modes (Gao, Gao, Xu *et al.*, 2016). In this case, spoof LSP modes can be seen as the Fabry-Perot–like resonances that arise due to the terminations of the open surfaces. Both the number of resonances and their frequencies can be tailored by tuning the total arc length of the fan. In hollow perfect conductor cylinders and disks in which the central hole displays a corrugated pattern [see Fig. 21(b)], multipolar spoof LSP resonances (Li, Xu *et al.*, 2014) also emerge, with characteristics that are similar to LSPs in the optical regime, but the EM field is concentrated in the central region. An alternative geometry was proposed and experimentally tested by Yang, Zhou, and Xiao (2015) and Zhou, Xiao, and
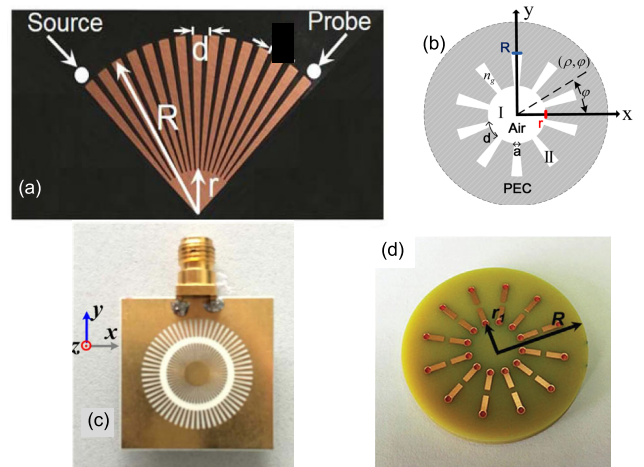

FIG. 21. (a) Photo of a fan-shaped ultrathin metallic corrugated resonator. The radius is $R = 12$ mm, the depth of the radial grooves is $h = 9$ mm, and the width and periodicity of the grooves are $a = 0.625$ mm and $d = 1.255$ mm, respectively. The thickness of the disk is $t = 18$ μm. From Gao, Gao, Xu *et al.*, 2016. (b) A 2D corrugated perfect conductor circular cavity with the inner and outer radii r and R, periodicity d, and groove width a. From Li, Xu *et al.*, 2014. (c) A corrugated ring resonator. From Zhou, Xiao, and Jia Yang, 2015. (d) Metadisk based on split-ring resonators that support spoof LSP modes. The period of the array is $p = 5.44$ mm. The gray region is the FR4 substrate with $d = 4$ mm and $l = 14$ mm. The brown region corresponds to the split-ring resonators made of copper with $a = 9$ mm, $s = w = 1.2$ mm, $t = 0.035$ mm, and $r = 0.8$ mm. From Qin *et al.*, 2018.

Jia Yang (2015). It consists of a corrugated ring resonator printed on a thin dielectric substrate, as depicted in Fig. 21(c). Basically, it is composed of a circular metal strip in which periodic arrays of grooves are placed on both surfaces of the ring and a dielectric substrate. When compared to the localized resonances of corrugated disks, spoof LSP modes in corrugated rings present higher quality factors, which are further enhanced when a ground plane is placed below the dielectric substrate, as previously discussed. More recently, so-called toroidal spoof LSP resonances have been reported (Qin *et al.*, 2018). These localized EM modes emerge in compact planar metadisks based on split-ring resonators; see Fig. 21(d). A toroidal multipolar mode is another form of a multipole that cannot be accounted for using a standard multimode expansion, as it is produced when currents flow on the surface of a torus along its meridian.

B. Subwavelength regime

Arguably the most relevant regime in conventional plasmonics is that of LSPs supported by metal nanoparticles of dimensions much smaller than the wavelength of relevant light. However, and in contrast to plasmonics in the optical regime, the subwavelength regime in the case of corrugated geometries cannot be reached using a simple downscaling of the structure, since in the perfect conductor limit resonance frequencies scale with the inverse of the size of the structure, as previously discussed. Hence, to bring spoof LSPs to the subwavelength regime, ω_a must be lowered while keeping R constant in the case of corrugated perfect conductor cylinders. As $\omega_a \approx \pi c / 2 h n_g$ for geometries containing 1D grooves, h and/or n_g must be increased in order to reach the subwavelength regime. Here we first discuss the effect of increasing n_g within the grooves in the spoof LSPs supported by corrugated cylinders.

Figure 22 presents the EM response of a textured perfect conductor cylinder with grooves filled with a dielectric material. The scattering cross section spectrum closely resembles what is observed for subwavelength metal particles at optical frequencies. This analogy suggests that the first

resonance peak is due to the electrical dipole resonance, while the narrow peak at higher frequency is associated with the electrical quadrupole. While the assignment of the high-frequency peak is correct, a calculation of the eigenmodes of the structure using the quasianalytical model reveals that the first resonance peak has contributions from two different EM modes with similar eigenfrequencies. The resonance frequencies of these two modes for the textured perfect conductor cylinder are displayed as vertical lines in Fig. 22 for the considered geometry. One mode has an electrical dipole character [see Fig. 22(b)], whereas the other mode has a field pattern that is independent of the azimuthal angle, as corresponds to a magnetic dipole pointing along the z axis [see Fig. 22(c)]. In the subwavelength limit, Eq. (21) predicts that the mode for $n = 0$ (i.e., the mode that is azimuthally independent) will be close in frequency to the mode for $n = 1$, but with a much broader linewidth. This result shows that the EM response of deep-subwavelength corrugated perfect conductor structures is at odds with what happens in standard plasmonics, in which the optical response of subwavelength metal nanoparticles is dominated by the electrical dipole resonance.

As the infinitely long 2D textured cylinder is transformed into a 3D corrugated disk of finite thickness, the frequencies of the EM resonances (electrical and magnetic dipoles) shift. While this coincides with the behavior observed for LSPs in the optical regime (the dipolar resonance wavelength decreases as the size of the particle is reduced), the quasidegeneracy between the electric and magnetic modes is lifted in the case of corrugated perfect conductor disks since the frequency shift associated with the magnetic mode is larger than that observed for the electric one, as illustrated in Fig. 23. The scattering spectra for two disks of different thicknesses L are shown in Fig. 23(a). The disks are corrugated with grooves filled with a dielectric material. As in the 2D case, in the 3D finite-element simulations an incident plane wave polarized
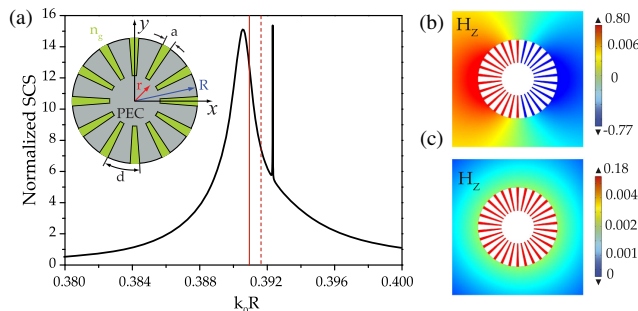

FIG. 22. Spoof LSPs supported by a cylinder corrugated with grooves filled with a dielectric material of refractive index $n_g = 8$ and geometrical parameters: $r = 0.4R$, $N = 40$, and $a/d = 0.3$. (a) Numerical scattering cross section (SCS) spectrum calculated using the finite-element method. The solid (dashed) vertical lines show the position of the $n = 1$ ($n = 0$) mode according to the quasianalytical model. (b),(c) Field pattern (H_z) at these two spoof LSP modes.
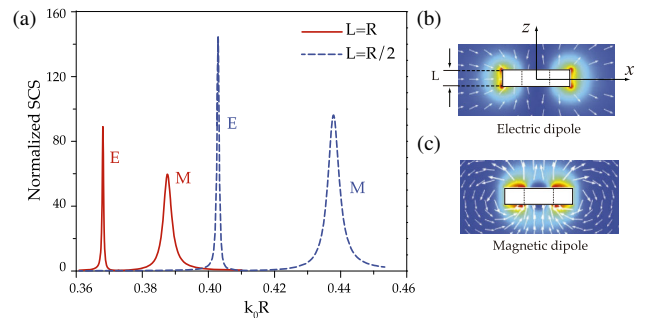

FIG. 23. Spoof LSPs in subwavelength perfect conductor disks corrugated with grooves filled with a dielectric material. Structures of finite thickness and with the same h, N, a/d, and n_g values as taken in Fig. 22 are considered. (a) SCS for corrugated disks of thicknesses $L = R$ (solid line) and $L = R/2$ (dashed line). (b),(c) Near-field distributions of the (b) electric and (c) magnetic dipole resonances for a disk of thickness $L = R/2$. The arrows show the electric-field lines and the color map shows the norm of the electric field in (b) and the magnetic field lines and magnetic field, respectively, in (c). From Huidobro *et al.*, 2014.

with the magnetic field pointing in the z direction and propagating along the x axis is considered. The scattering cross section is calculated from the scattered Poynting vector, where the geometrical normalization factor is in this case $\sigma_{\text{geom}} = 2RL$. Two distinct peaks can be seen in the cross section plot for disks of thicknesses $L = R$ (solid line) and $L = R/2$ (dashed line). The field patterns associated with the two peaks, displayed in Figs. 23(b) and 23(c) for the $L = R/2$ case, show that the resonance at lower frequencies corresponds to the electric LSP while the one at a higher frequency is a magnetic LSP. This is consistent with the vectorial plots also displayed in those panels. In the first case [Fig. 23(b)], the E-field arrows go from one end of the structure to the other, as corresponds to an electrical dipole, whereas in Fig. 23(c) the arrows show how the magnetic field circulates around the disk, as corresponds to a magnetic dipole.

Standard dielectric particles of subwavelength sizes and large refractive index also display magnetic and electric dipole modes (García-Etxarri *et al.*, 2011; Kuznetsov *et al.*, 2012) that are reminiscent of the ones under study here. However, as opposed to the modes for the corrugated perfect conductor disk, for dielectric particles the magnetic dipole resonance lies at lower energies than the electric dipole resonance. The physical origin of this opposite frequency ordering for corrugated perfect conductor and dielectric disks is related to the dissimilar shapes of the corresponding electric-field line patterns (Huidobro *et al.*, 2014). This difference is associated with the fact that the effective metamaterial parameters are both anisotropic and inhomogeneous, as previously discussed.

As a proof of concept, it has been shown that subwavelength perfect conductor structures corrugated with grooves filled with a dielectric material indeed support spoof dipolar LSPs, and they can display either an electrical or a magnetic character (Huidobro *et al.*, 2014). However, they rely on dielectric materials with high refractive indexes, which places severe limitations on the feasibility of their implementation. Building up spoof LSP modes supported by purely metallic structures is more convenient from a practical point of view. As previously discussed, another way to decrease ω_a, and hence reach the subwavelength regime, is to increase the length of the grooves, i.e., to use long air grooves that possess an effective length much larger than R such that $h \gg R$. Two different strategies that exploit this basic idea have already been pursued: cylinders or disks corrugated with either meanders or spiral grooves. Numerical simulations have confirmed that bent grooves behave like larger straight ones, despite the possible internal reflections at the bends (Huidobro *et al.*, 2014). Figure 24 summarizes the results on the spoof LSP modes supported by perfect conductor structures corrugated with meanders. The geometry of the structure is shown in the inset: a cylinder of radius R is textured with four meander-shaped grooves of effective depth $h_m \approx N(R - r)/4$. The computed scattering cross section for such a structure is plotted as a black line for the 2D case. As in the previously discussed case of a perfect conductor cylinder with filled grooves, the scattering spectrum presents a dominant peak that contains both electrical and magnetic dipolar modes, as shown in Figs. 24(b) and 24(c). Three-dimensional structures corrugated with meanders also behave like perfect conductor disks
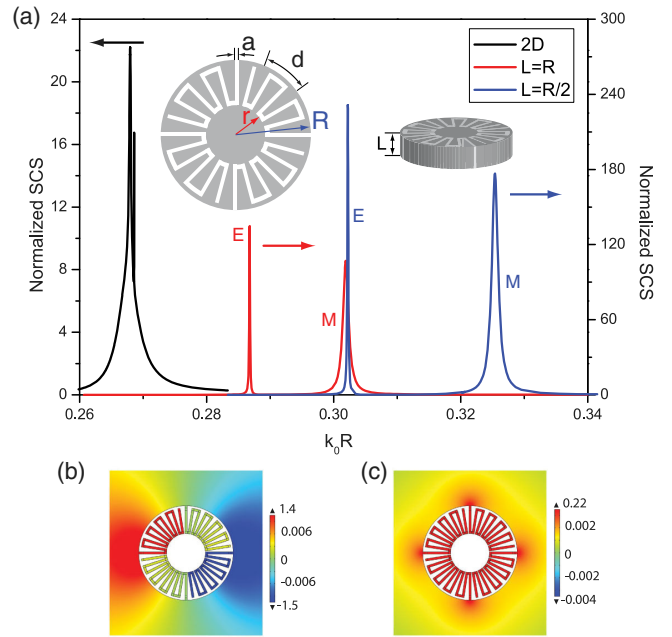

FIG. 24. Spoof LSPs in perfect conductor subwavelength structures without dielectric filling. (a) SCS for an infinite cylinder (black line) and disks of thicknesses $L = R$ (red line) and $L = R/2$ (blue line), corrugated with four meanders and with parameters $N = 40$, $a = 0.3d$, $n_g = 1$, and effective depth $h_m \approx 6R$. (b),(c) Field pattern (H_z amplitude) for the 2D case at the dominant peak in the spectrum ($k_0 R = 0.27$) showing the (b) electric dipole and (c) magnetic dipole modes, respectively. From Huidobro *et al.*, 2014.

corrugated with filled grooves. In particular, the scattering spectrum for disks with meanders (thicknesses $L = R$ and $L = R/2$) shows a shift in resonant frequencies, with the magnetic LSP spectrally located at higher frequencies than the electrical LSP, as in the case of corrugated perfect conductor disks with grooves filled with a dielectric material.

An alternative way of achieving grooves of long depth is based on a spiral geometry. As in the case of meander-shaped grooves, a perfect conductor structure (cylinder or disk) textured with spiral-shaped grooves mimics the EM response of a corrugated perfect conductor particle with shallow grooves and filled with a dielectric (Huidobro *et al.*, 2014). Moreover, both electrical and magnetic spoof LSP modes survive in ultrathin metallic disks (limit $L \to 0$), as illustrated in Fig. 25, where the existence of these spoof LSP modes in the microwave regime was confirmed both theoretically and experimentally. The measured near-field spectrum for the ultrathin spiral structure is presented in Fig. 25(a) with a solid line. The EM response of the structure is measured by means of a transmitting antenna that is placed 3 mm away from one side of the sample to excite the modes, and a receiving antenna that is located at the other side of the sample to detect the resonance spectrum. Two distinctive resonance peaks at frequencies $f = 1.1$ GHz ($k_0 R = 0.22$) and $f = 1.87$ GHz ($k_0 R = 0.37$) can be clearly identified. To reveal the physical nature of these two resonances, the extinction cross section spectrum for the same structure is also shown (dashed line). This spectrum has been calculated by means of full wave
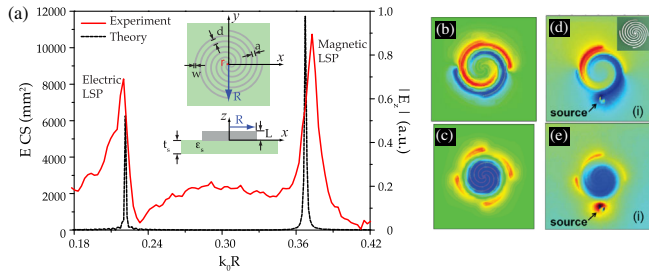
FIG. 25. Resonance spectrum for subwavelength ultrathin textured metallic disks. (a) Experimental near-field spectrum ($|E_z|$ is measured) and calculated extinction cross section spectrum. Insets: the structure shown placed atop a dielectric of thickness $t_s = 0.8$ mm and $\epsilon_s = 3.5$. The parameters of the fabricated structure are $R = 9.5$ mm, $r = 0.6$ mm, $d = 1.508$ mm, $a = 1.008$ mm, and $L = 0.035$ mm. (b),(c) Calculated near-field distribution of the E_z-field component at the (b) electric and (c) magnetic spoof LSPs in a x-y plane cut 1.5 mm above the ultrathin disk. Red and blue indicate positive and negative values, respectively. (d),(e) Measured near-field distribution of the LSP. The same quantities as in (b) and (c) are plotted. (d) Photograph of the sample. From Huidobro *et al.*, 2014.

simulations in which both the metal absorption and the presence of a dielectric substrate are taken fully into account. The simulated field patterns at the two resonances are plotted in Figs. 25(b) and 25(c), showing that the first resonance is due to the electrical spoof LSP [Fig. 25(b)], while the second peak emerges from the magnetic spoof LSP [Fig. 25(c)]. The measured near-field distributions are presented in Figs. 25(d) and 25(e), which show the local z component of the electric field for both modes. A comparison of Figs. 25(d) and 25(e) with the numerical results shown in Figs. 25(b) and 25(c) shows a notable agreement between the simulation results and the experimental images.

Ultrathin metallic disks textured with spiral-shaped grooves also support high-order electrical and magnetic spoof LSP modes, as reported by Gao, Gao, Zhang, Shi *et al.* (2015). In particular, the high-order magnetic spoof LSP resonances exhibit a higher sensitivity to the environmental refractive index than the fundamental magnetic dipole ones. Along these lines, an analytical model was developed (Liao, Fernandez-Dominguez *et al.*, 2016) to describe the EM properties of the 2D version (an infinitely long cylinder), showing that their associated spoof LSP modes can be engineered through the spiral angle and the number of grooves. Taking advantage of the Babinet principle, a complementary version of the previously discussed ultrathin metallic spiral structure was proposed and experimentally tested (Gao, Gao, Zhang, and Zhang, 2015). The structure consists of several spiral slots perforated on a metallic thin layer. As expected from the Babinet principle, their electric (magnetic) mode profiles match the magnetic (electric) mode profiles of the metallic spiral structure, in which the frequency order of the resonances is inverted; i.e., the spoof LSP mode with a magnetic dipole character now emerges at lower frequencies that the electrical dipole one.

To mitigate the inherent losses of metals when building up structures that support spoof LSP resonances, Li *et al.* (2019)

designed a bounded waveguide filled with a dielectric material whose resonances are similar to spoof LSP resonances. Unlike the metal case in which TM modes are the relevant ones, here the surface EM modes are created by the structural dispersion of the TE modes. Owing to the strongly suppressed absorption losses, the designed structure can support multipolar sharp resonances that are expected to be sensitive to the dielectric environment and robust to the size and shape of the resonator, which could be used for sensing applications.

C. Coupled resonators and arrays of resonators

Near-field coupling between resonators supporting spoof LSP modes has also been reported. When two corrugated disks with asymmetric geometries are placed in proximity on the same horizontal plane (Liao, Pan *et al.*, 2014), coupling between the multipolar modes of each disk occurs, leading to the emergence of Fano resonances due to interference. In this way, dark modes of one disk become bright thanks to the interaction with the dipole mode of the other disk. Note that these Fano resonances do not emerge when two equal corrugated disks are utilized but reappear when the coupling is vertical, as demonstrated by Gao, Gao, Luo, and Zhang (2016a). Figure 26(a) displays the transmission spectrum in the horizontal configuration, showing how the hexapole and octopole modes hybridize and the associated resonances split, showing no signatures of Fano resonances. The near-field excitation is achieved with a monopole antenna at the point marked "Source" in the inset of Fig. 26(a), and the transmission spectrum is measured with another monopole antenna at the point labeled "Probe." Coupling is much stronger in the vertical configuration, leading to a larger mode splitting and, as a result, a so-called invisibility dip associated with a Fano-like process emerges in the spectrum due to the interference between the hexapole and octopole modes; see Fig. 26(b).

Couplings between subwavelength ultrathin metallic disks textured with spiral-shaped grooves have also been studied. When placed in the horizontal configuration [see Fig. 26(c)], the hybridization between the spoof LSP electrical-dipolar modes of each metallic disk results in the splitting of these modes into bonding and antibonding resonances (Zhang *et al.*, 2017), in a manner similar to what happens in simple molecules like H_2. These hybrid modes can be manipulated to produce enormous field enhancement (> 5000) by tuning the separation between the disks, as shown in Fig. 26(d). Two coupled spiral particles were also analyzed in a vertical configuration (Gao, Gao, Zhang, and Zhang, 2016), in accordance with the symmetric and antisymmetric stacking configurations, as shown in Fig. 26(e). The resonance spectra of mode splitting associated with the magnetic spoof LSP modes are shown in Fig. 26(f). For both symmetrically and antisymmetrically stacked dimers, the magnetic dipole moments of the two particles align parallel at the lower split frequency, but antiparallel at the higher one. However, despite the similar magnetic coupling, the electric coupling depends on the direction of spiral grooves and accounts for the difference of mode splitting frequencies between the two stacking configurations.

Resonators able to support spoof LSP modes have also been used as building blocks of 1D photonic crystals that can be
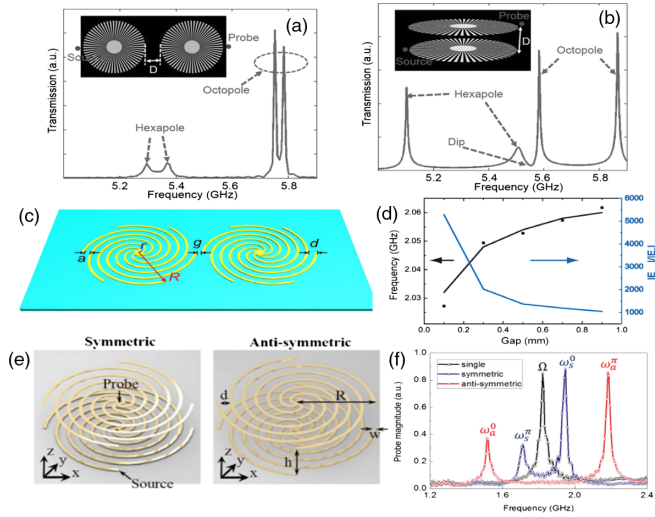
FIG. 26. (a) Transmission spectrum obtained when two corrugated disks are placed in proximity at the same horizontal plane (see inset). (b) Transmission spectrum obtained when the two corrugated disks are placed in the vertical coupling configuration at the same distance. The geometrical parameters are the same as those in (a). (a),(b) From Gao, Gao, Luo, and Zhang, 2016. (c) Photograph of adjacent spiral structures placed in a horizontal configuration. The gap between the two spirals is $g = 0.1$ mm. (d) Resonance frequency of the "bonding" spoof LSP mode and the maximum field enhancement (blue) as a function of the gap size. The solid curves correspond to the simulation results, and the dots denote the measurement result. (c),(d). From Zhang *et al.*, 2017. (e) Schematic of symmetric and antisymmetric stacking configurations of two vertically coupled metallic spiral structures. The two monopole antennas indicated as black arrows can be used to excite and probe the resonances. (f) The measured near-field response spectra of a single metallic spiral structure (black triangles) and two vertically coupled metallic spiral structures with symmetric (blue squares) and antisymmetric (red circles) stacking configurations. (e),(f) From Gao, Gao, Zhang, and Zhang, 2016.
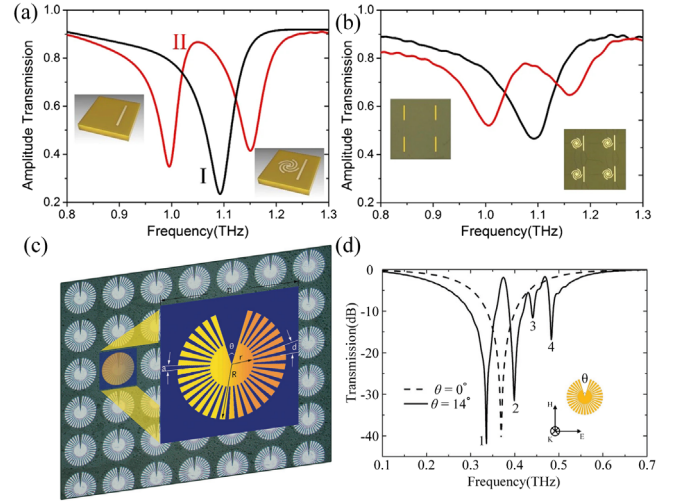

FIG. 27. (a) Simulated amplitude transmission spectra of the cut-wire structure (black line) and the combined system (red line). Insets: structures of the simulated unit cells. (b) Measured amplitude transmission spectra for the two systems shown in (a). (a),(b) From Liao, Liu *et al.*, 2016. (c) Schematics and microscopic image of a 2D array made of defected corrugated metal disks. The geometrical parameters are $r = 60$ μm, $R = 150$ μm, $d = 2\pi R/36$, and $a = 0.4d$. (d) Simulated transmission spectra of symmetric (dashed line) and symmetry broken (solid line) under normal incidence with an angle of defect of 14^0. Modes 1–4 correspond to dipole, quadrupole, hexapole, and octopole modes, respectively. (c),(d) From Chen *et al.*, 2017.

utilized as waveguides operating in the microwave regime. It has been demonstrated (Gao, Gao *et al.*, 2017) that the coupling factor between the previously described tightly localized spoof LSP modes can reverse its sign by choosing between the two different coupling configurations (bonding and antibonding). As a consequence, two propagating spoof EM modes with positive and negative group velocities arise in the same frequency range, forming a Dirac-point-like crossing of dispersions and allowing for a switching between forward and backward surface Bloch waves using selective excitation. More recently, a 1D waveguide consisting of metal spiral structures was also proposed and tested experimentally (Fu *et al.*, 2020). Thanks to the deep-subwavelength confinement associated with the magnetic spoof LSP modes supported by the individual resonators, this waveguide is able to propagate microwave radiation along highly curved surfaces over long distances.

Two-dimensional arrays made of such spoof LSP-based resonators as unit cells have been also constructed aiming to build up 2D metamaterials and metasurfaces with interesting functionalities in the terahertz and microwaves ranges of the EM spectrum. When an ultrathin metallic disk textured with spiral-shaped grooves is used as the unit cell of the 2D metamaterial, only the electrical dipole LSP mode can be excited by a normally incident plane wave. However, if an additional metallic cut wire is introduced within the unit cell, the near-field coupling between the wire and the spiral structure allows for the excitation of the magnetic spoof LSP dipole mode, leading to the emergence of a transparency window in the transmission spectrum associated with this coupling, as found by Liao, Liu *et al.* (2016) and shown in Figs. 27(a) and 27(b). These new transmission features can be seen as a consequence of the phenomenon of electromagnetically induced transparency in which the role of radiative element ("bright atom") is played by the dipolar mode supported by the cut wire and the subradiant element ("dark atom") is the magnetic spoof LSP dipole mode associated with the ultrathin metallic disk. A similar behavior was found in the microwave regime upon replacing the metallic cut wire with an additional layer of hybrid resonators that combines metallic cut wires and square rings within the same unit cell (Liu, Xu *et al.*, 2020). Another strategy to make the dark multipolar spoof LSP resonances emerge in the spectrum of 2D metamaterial arrangements consists of placing a C-shaped resonator in the vicinity of the corrugated disks, as demonstrated by Chen *et al.* (2016). An alternative way to transform dark multipolar spoof LSP modes into bright ones and mimic the phenomenon of electromagnetically induced transparency is to break the symmetry of the corrugated metallic disk by introducing a small angular defect (Chen *et al.*, 2017). In this way, mutual coupling between spoof SP modes results in the
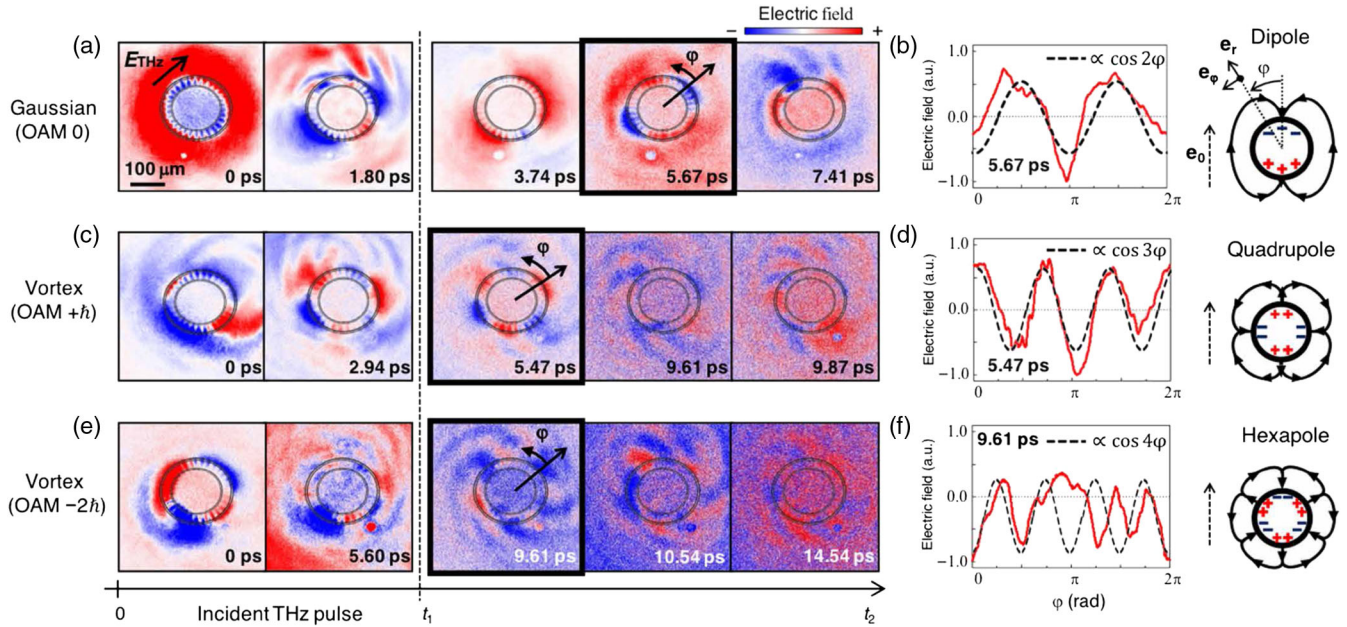
FIG. 28. Selective excitation of multipole localized spoof SPs. Selected snapshots of the near-field evolution around the sample excited by (a) a Gaussian beam, (c) a vortex beam (OAM $+ \hbar$), and (e) a vortex beam (OAM $- 2\hbar$) are shown. The double circle represents the position of the sample (inner and outer radii). The time origin (0 ps) is the time when the first positive peak of the incident pulse comes. (b),(d),(f) The electric field taken along the outer circle of the sample as a function of the azimuthal angle ϕ (red curves). The dashed cosine curves are the expected electric-field patterns when the modes depicted on the right are excited. The solid arrows schematically represent the quasistatic electric field around each mode. From Arikawa *et al.*, 2020.

emergence of multiple Fano resonances, each of which leads to a transparency window in the terahertz transmission spectrum, as illustrated in Figs. 27(c) and 27(d).

A more sophisticated approach to detect dark multipolar spoof LSP modes supported by ultrathin corrugated disks is using vortex beams as probes instead of plane waves (Arikawa *et al.*, 2020). Manipulation of the vortex beam orbital angular momentum (OAM) allows for a selective excitation of the multipolar modes of the structure, as the selection rules appear from the conservation of the total OAM, as illustrated in Fig. 28. The efficient transfer of the light's OAM to elementary excitations in solid-state systems at room temperature, as demonstrated by Arikawa *et al.* (2020), opens up many possibilities for the manipulation of orbital angular momentum that could provide a feasible platform for terahertz sensing.

V. PASSIVE AND ACTIVE DEVICES

Spoof SPs show some advantages over traditional technologies in the design of both passive and active functional devices. Compared to traditional microwave technology, spoof SP devices not only provide a customized approach to optimize the performance, but also break a series of technological challenges in traditional microwave engineering at a fundamental level. In this section, we review the development of passive and active devices based on spoof SPs in the microwave and terahertz regimes.

A. Passive devices based on spoof SPs

As previously mentioned, 1D metallic gratings with designed EM characteristics are one of the most

straightforward platforms to guide the propagation of spoof SPs. With specifically designed gradient gratings, spatial EM modes, e.g., a cylindrical wave from a probe, as shown in Fig. 29(a), can first be coupled to the spoof SP waveguide and then guided in a predetermined direction or split into different branches (Caglayan and Ozbay, 2008; Zhou and Cui, 2011). In addition to straight channels, the high transmission efficiency of spoof SPs has been experimentally verified in bending paths at microwave frequencies (Zhou, Jiang, and Cui, 2011), as shown in Fig. 29(b). However, all these spoof SP waveguides have an inherent
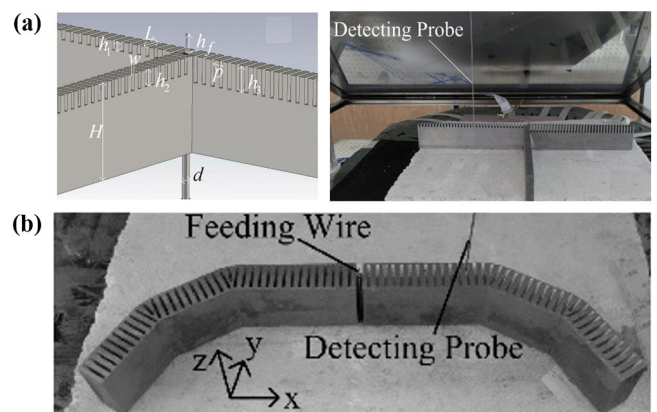

FIG. 29. Bulky transmission lines based on spoof SPs. (a) Sketch of a three-directional surface-wave splitter (left panel) and photograph of the field mapping experiment setup (right panel). From Zhou and Cui, 2011. (b) Fabricated bending splitter and the feeding wire used to excite the spoof SPs in the gratings. From Zhou, Jiang, and Cui, 2011.

3D character, and therefore are difficult to incorporate into compact, planar, or light communication systems. That is why conformal surface plasmons, which can propagate through ultrathin and flexible metal films (Shen *et al.*, 2013), as described in Sec. III.C, are better suited as building blocks in the design of 1D waveguides, also called transmission lines, at low frequencies.

Different types of transmission lines based on conformal surface plasmons have been conceived for different purposes. Both single-sided (Liao, Zhao *et al.*, 2014; Kianinejad, Chen, and Qiu, 2015) and double-sided strips (Ma *et al.*, 2014; Kianinejad, Chen, and Qiu, 2016) can operate as single-conductor waveguides in ungrounded planar circuits. Examples illustrating these two types of transmission lines are depicted in Figs. 30(a) and 30(b). Single-conductor waveguides are better suited to flexible platforms than traditional multiconductor waveguides. However, owing to the fact that a great portion of integrated circuits are packaged and that a metallic ground is sometimes unavoidable, dual-conductor transmission lines containing the ground [see Fig. 30(c)] have also been developed (Zhang, Zhu *et al.*, 2015; Lee, Wang, and Cappelli, 2017). Compared to conventional 1D waveguides such as microstrip lines, coplanar waveguides, and substrate-integrated waveguides, spoof SP–based waveguides possess great flexibility in terms of dispersion relations, the modal field, and transmission properties. On the one hand, its band gap can be controlled by tuning the geometry of the unit cell, as explained in Sec. III. On the other hand, a strong confinement
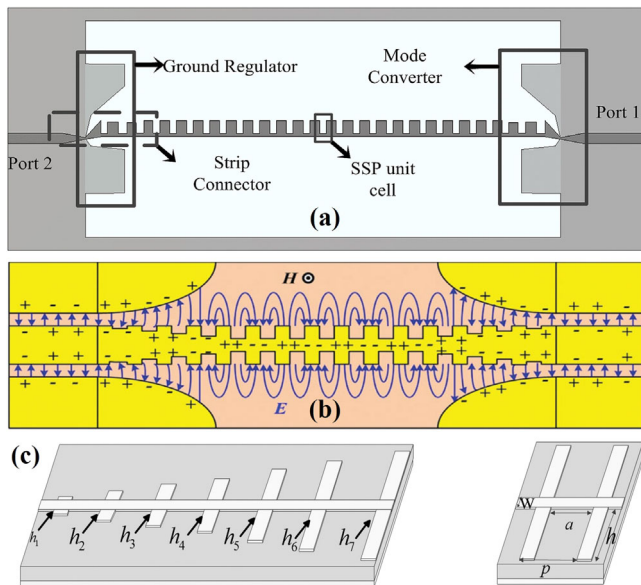

FIG. 30. Ultrathin transmission lines based on spoof SPs. (a) Conformal surface plasmon structure connected to a microstrip line via matching transitions to build a hybrid substrate-integrated waveguide–spoof SP device. From Kianinejad, Chen, and Qiu, 2015. (b) Configuration for bridging coplanar waveguides and ultrathin corrugated metallic strips that are capable of supporting the propagation of conformal surface plasmons. From Ma *et al.*, 2014. (c) A grounded spoof SP transmission line that presents a gradient in the grooves' depth for a better conversion of the surface EM waves supported by the microstrip line with conformal surface plasmons. From Zhang, Zhu *et al.*, 2015.
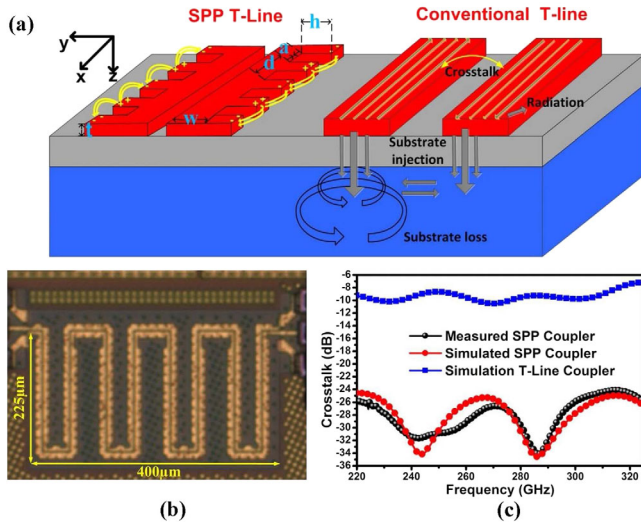
of EM fields leads to both low mutual coupling between adjacent transmission lines and low radiation loss. Moreover, the modal field can be designed through the specific configuration of the waveguide. For example, the distribution of EM fields present even or odd parities in spoof SP–based waveguides, depending on the feeding mechanism that is utilized (Gao, Zhou, and Cui, 2015; Du *et al.*, 2020). Backward waves with an antiparallel phase and negative group velocities are available when the dispersion relation displays a negative slope (Quesada *et al.*, 2014; Liu *et al.*, 2016, 2018). More recently complex geometries such as glide ones were introduced to offer even more freedom to control the propagation of spoof SPs (Padilla *et al.*, 2018; Yan *et al.*, 2021).

High-efficiency excitation of spoof SPs is essential to the performance of transmission lines. Conventional SPPs are commonly excited using components such as prisms and grating couplers in order to compensate for the momentum mismatch between the incident plane wave and the corresponding SPP wave. Along these lines, for microwave and terahertz frequencies specific gradient-index metasurfaces can provide nearly 100%-efficiency conversions (O'Hara and Averitt, 2005; Sun *et al.*, 2012). Different strategies have been utilized for the excitation of spoof SPs aiming to feed transmission lines. For instance, simple monopoles can be positioned close to the waveguide [see Fig. 29(a)], but this leads to poor coupling efficiency due to a large impedance mismatch. Most traditional 1D waveguides are fed with a coaxial cable or other types of waveguides in which only guided modes are supported. However, transmission lines based on spoof SPs cannot be fed in the same manner due to their significantly different spatial profiles. A series of adapters need to be developed to build the bridge between guided waves and spoof SPs. For the single-sided waveguide shown in Fig. 30(a), an efficient transition region is designed to transform the quasi-TEM mode supported by a microstrip line to the TM mode on the spoof SP waveguide by matching the momentum and polarization. In addition, the impedance of the spoof SP structure is matched to that of the microstrip transmission line. For the double-sided spoof SP waveguide in Fig. 30(b), a balanced matching transition includes gradient corrugations and flaring ground between a coplanar waveguide and the spoof SP structure. The grounded spoof SPP transmission line in Fig. 30(c) can be efficiently excited through a gradient-corrugated strip because smooth changes of both the wave vector and impedance from the microstrip to the spoof SP structure are possible. Excitation methods for other types of waveguides, such as dual-strip spoof SP–based waveguides (Zhang, Cui *et al.*, 2015) and hybrid substrate-integrated waveguide–spoof SP transmission lines (Guan *et al.*, 2017), have also been devised.

Owing to the strong confinement of EM energy, 1D waveguides based on conformal surface plasmons can break the physical limit of signal integrity as they significantly reduce mutual coupling (Zhang, Cui *et al.*, 2015). Depressed mutual coupling is in extremely high demand in on-chip systems because complex circuitry and components are usually embedded in a limited space. Figure 31 shows an example of on-chip subterahertz spoof SP transmission lines using standard 65 nm complementary metal oxide semiconductor (CMOS) technology. Two transmission lines with

FIG. 31. Compact devices. (a) Layout and *E*-field distributions of two different structures deposited in a lossy substrate environment: two conventional microstrip transmission lines (right) and two ultrathin corrugated metal strips that support conformal surface plasmon modes (left). (b) Die micrograph of a coupler based on spoof SPs that is built up in 65 nm CMOS technology and able to operate in the terahertz range. (c) Comparison between the cross talk performance (measured and simulated) of the two structures depicted in (a). From Liang *et al.*, 2015.

a separation of 2.4 μm present a -30 dB cross talk ratio on average in the operation range between 220 and 325 GHz, which is around 20 dB lower than the control sample of microstrip lines in the same range (Liang *et al.*, 2015).

Transmission lines based on spoof SPs have also been proposed as a feasible technology for interconnecting chips (Joy *et al.*, 2019). This work has demonstrated that a dynamic interconnect based on spoof SPs could work in two distinct regimes: as a *RC*-limited electrical interconnect at low frequencies and as a beyond *RC*–limited communication channel near its resonant frequency. Limits on the information transfer capability of the spoof SP structure have been theoretically analyzed and show that the bandwidth density of the spoof SP communication network with $\sim$10 mm information transfer distance can exceed 1 Gbits/s μm, where each channel can carry 300 Gbits/s information with nominal cross talk. This type of spoof SP–based interconnections could be applied between two chips as an energy-economic solution to traverse the "last centimeter" distance and facilitate the development of fast and reliable data transfer communication with high signal integrity.

As discussed in Sec. III, dispersion relations of propagating spoof SPs present a cutoff frequency, which has been utilized for filtering purposes. Different types of filters based on spoof SP waveguides, including low-pass, bandpass, and band-stop ones, are feasible when designed transmission zeros are added to the bare waveguides. Figure 32(a) shows a coplanar waveguide-fed spoof SP bandpass filter composed of two oppositely oriented single-sided corrugated strips coupled to two double-sided corrugated strips (Yin *et al.*, 2015). The transmission spectrum is governed by the coupling part (as shown in the dashed box)
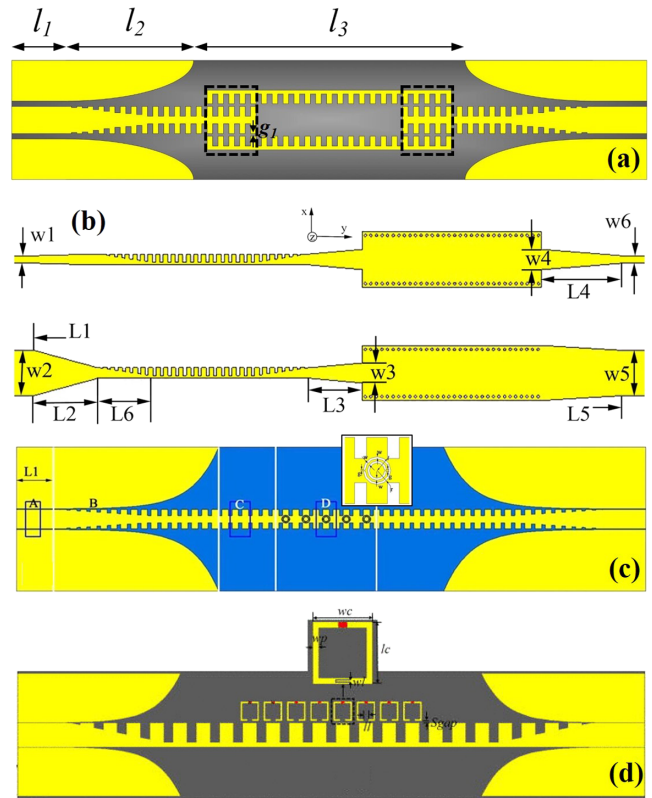

FIG. 32. Filters based on spoof SPs. (a) An ultrathin metallic frequency-selective structure based on conformal surface plasmons, in which the yellow part is metal and the dark gray part is a thin dielectric substrate. From Yin *et al.*, 2015. (b) Top and bottom views of a hybrid circuit containing both a spoof SP waveguide and a surface-integrated waveguide. From Zhang, Zhang *et al.*, 2015. (c) A filter based on ultrathin corrugated transmission lines in which several split-ring resonators are etched. From Zhang, Zhang *et al.*, 2016. (d) Schematic of the frequency-spectrum-controllable 1D waveguide based on spoof SPs that is loaded with varactor diodes to control its transmission properties. From Xu *et al.*, 2016.

and can be tuned by modifying the size of the gap, the length of the coupling strip, and also the number of unit cells involved. Figure 32(b) shows another bandpass filter whose lower cutoff frequency is dictated by the low-pass property of the spoof SP component, whereas the high-pass filtering property is provided by the surface-integrated waveguide (Zhang, Zhang *et al.*, 2015). Band-stop filters can be also devised by introducing resonant components such as split-ring resonators and electric-*LC* structures. Figure 32(c) shows an example of a rejection filter based on the interaction between conformal surface plasmons and complementary split-ring resonators (Zhang, Zhang *et al.*, 2016). Different kinds of resonators have been adopted in bandpass and band-rejection filters at microwave (Pan *et al.*, 2014; Zhang and Chan, 2020) and terahertz (Jaiswal, Pandit, and Pathak, 2019b) frequencies. Moreover, structures based on spoof SPs can operate as frequency-spectrum-reconfigurable filters if tunable capacitances are loaded in the system. In Fig. 32(d) varactor diodes are embedded in split-ring resonators and tuned electrically. In this way,
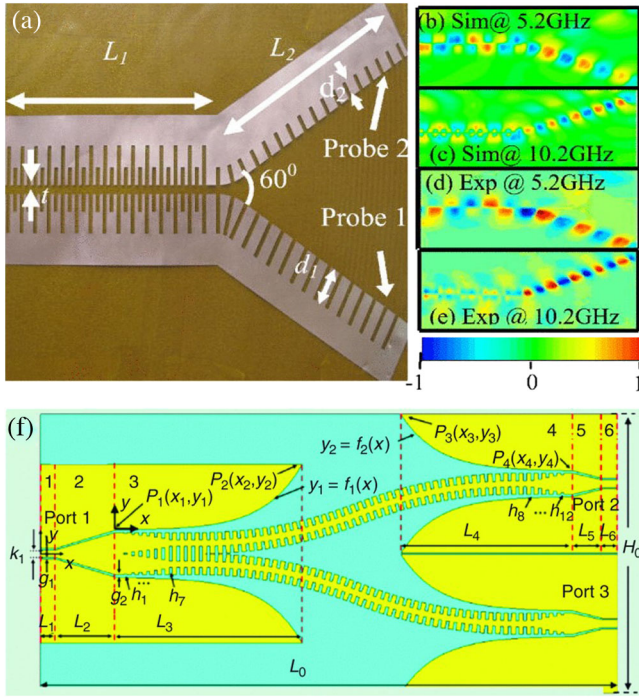
FIG. 33. Splitters based on spoof SPs. (a) Photo of a fabricated ultrathin frequency splitter based on spoof SPs, which is composed of one straight double-periodic grating and two single-periodic grating branches. (b)–(e) Simulation and experimental results of the E_z field distributions of the frequency splitter shown in (a), evaluated at 5.2 and 10.2 GHz. (a)–(e) From Gao *et al.*, 2013. (f) Schematic of a terahertz ultrawideband power divider. From Gao, Zhou *et al.*, 2015.

real-time controlled band rejection of spoof SPs was achieved in the frequency range 3.7–4.6 GHz (Xu *et al.*, 2016).

In addition to filters, power dividers and splitters that build up the network and control the power flow in circuits are key components in EM technology and have also been constructed using 1D waveguides based on conformal surface plasmons. An example of a frequency splitter is presented in Fig. 33(a) (Gao *et al.*, 2013). At the input side, a transmission line with double-periodic gratings is designed to support two conformal surface plasmon modes that have different asymptote frequencies. Two branches diverging at an angle of 60° are then devised as output channels such that the two different operating frequencies split spatially when reaching the junction, as shown in Figs. 33(b)–33(e). An ultrawideband 3 dB power divider has also been constructed using a straight-composite transmission line based on spoof SPs and two branches as shown in Fig. 33(f) (Gao, Zhou *et al.*, 2015). Coplanar waveguide sections and transitions are added at three ports of the network to guarantee high transmission and low reflection. Besides, an unequal power divider can also be achieved by constructing symmetric or quasisymmetric structures (Wu *et al.*, 2016). Dividers based on spoof SPs possess broadband performance and easy implementation of flexible power-dividing ratios and branches (Zhou *et al.*, 2019).

Figure 34 presents examples of a frequency splitter [Fig. 34(a)] and a 3 dB directional coupler [Fig. 34(b)], both
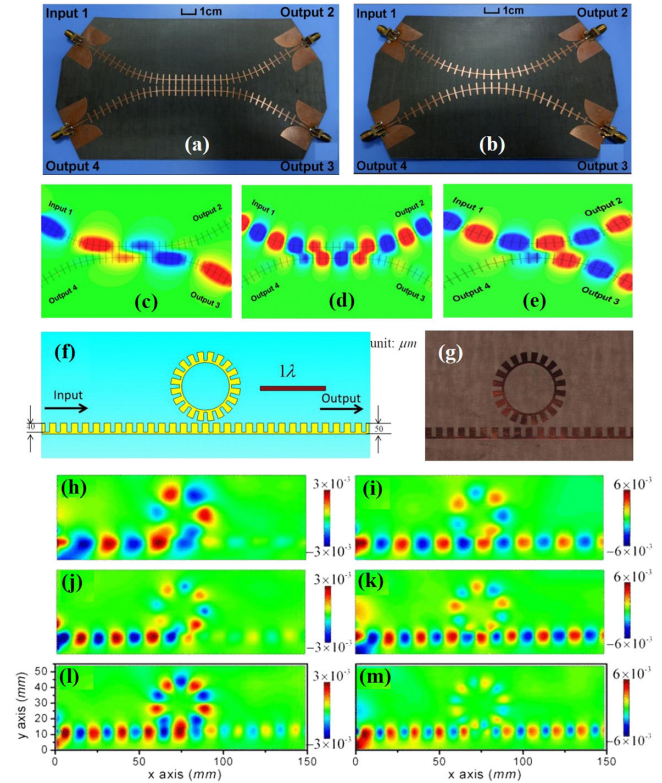

FIG. 34. (a) Photograph of a splitter device operating in the microwave regime based on the propagation of conformal surface plasmons with input and output coplanar waveguide sections linked with subminiature connectors. (b) Photograph of a 3 dB directional coupler device also operating in the microwave regime. Simulated electric-field E_z distributions for the frequency splitter of (a) evaluated at (c) 0.25 and (d) 0.55 THz. (e) Simulated electric-field E_z distribution for the directional coupler of (b) evaluated at 0.45 THz. (a)–(e) From Liu *et al.*, 2014. A planar ring resonator composed of a transmission line based on spoof conformal surface plasmon modes and a corrugated metallic ring: (f) the geometry in the terahertz regime and (g) a photograph of the prototype fabricated for operating at microwave frequencies. Measured electric fields of the planar ring resonator of (g) evaluated at (h) 7.5, (i) 8.5, (j) 9.3, (k) 10, (l) 10.6, and (m) 11.2 GHz. (f)–(m) From Shen and Cui, 2013.

of which are based on spoof SP waveguides. In the frequency splitter, the two strips are identical and full power can be transferred provided that the coupling length satisfies a specific relation with the wavelength-dependent coupling constant (Liu *et al.*, 2014). Thanks to this design, the EM energy is directed to different arms at different frequencies, as illustrated in Figs. 34(c) and 34(d). For the 3 dB directional coupler, though, the two strips are constructed to have different geometrical parameters, and hence different propagation constants. In this case, the EM energy cannot be completely switched from one arm to the other. However, within a specific frequency range (e.g., from 0.40 to 0.47 THz), the EM energy is almost equally divided to outputs 2 and 3, as shown in Fig. 34(e).

The coupling between waveguides based on spoof SPs and planar ring resonators can also lead to interesting functionalities, as demonstrated by Shen and Cui (2013).

This structure was designed for terahertz frequencies [see Fig. 34(f)] and fabricated in the microwave frequency regime [see Fig. 34(g)]. When the phase change around the ring is equal to $2m\pi$, with m an integer, the ring is in the resonance state and the signal is transmitted to the output port. When the phase change is equal to $(2m + 1)\pi$, the ring is in the closed state and the signal is cut off. The measured electric-field distributions demonstrate these two operation regimes, as shown in Figs. 34(h)–34(m).

Antennas with designed radiation patterns are essential components in wireless communication systems. To construct antennas based on spoof SPs, it is necessary to convert a propagating spoof SP mode on a waveguide into radiating waves with a tailored far-field performance. This can be achieved by using a 1D phase-gradient metasurface as a basic component and incorporating a designed modulation to the corrugated structures, as illustrated in Fig. 35(a) (Xu *et al.*, 2015). Another way to create an antenna device based on spoof SPs is to introduce space harmonics in the corrugated structure such that the corresponding spoof SPs travel fast enough to radiate. A diffraction radiation based on an antisymmetric transmission line [see Fig. 35(b)] (Xu *et al.*, 2017) and a leaky-wave radiation based on the combination of a spoof SP waveguide and an array of circular patches [see Fig. 35(c)] (Yin *et al.*, 2016) belong in this category. Sinusoidally or triangularly modulated strips with periodically changed groove depths also serve as leaky-wave antennas (Kong *et al.*, 2016; Liao, Zhou *et al.*, 2020). When combined with periodically modulated ring resonators, this antenna is able to radiate a vector vortex beam (Yin *et al.*, 2018; Liao, Zhou *et al.*, 2020), as shown in Fig. 35(d). A third strategy in antenna design is to use resonators based on spoof LSPs as end-fire radiators, as depicted in Fig. 35(e). These resonators can then be fed using different types of networks (Pan and Cui, 2017; Yin *et al.*, 2017; Liao, Luo *et al.*, 2020).

Taking advantage of the strong field enhancement and ultrahigh Q factor associated with the excitation of spoof LSP modes, novel types of microwave sensing applications, including liquid sensing, gas sensing, and dielectric permittivity sensing have been devised. It has been demonstrated that a device composed of two stacked corrugated metal rings (Zhou *et al.*, 2020) is able to support an EM resonance with a Q factor of around 3×10^3 allowing for detection of minute changes of glucose aqueous solutions as small as 10 mg/dl. An ultrafast and high-sensitivity humidity sensor has been also fabricated that is able to quantify the humidity by monitoring the transmission coefficient and resonance frequency of the spoof LSP device (Yu *et al.*, 2020). A microfluidic chemical sensor was also created based on quarter-mode spoof LSPs, which possesses the merits of high sensitivity, compact size, and a limited requirement to test liquid (Shao, Zhou, and Yang, 2018). A microfluidic approach has also been adopted to design a label-free and highly sensitive sensor for aqueous biological samples (Pandit, Jaiswal, and Pathak, 2020). In addition, because of the flexible and conformal property of conformal surface plasmons, sensors based on this type of spoof SPs have great potential in wearable and stretchable devices, such as a microfluidic
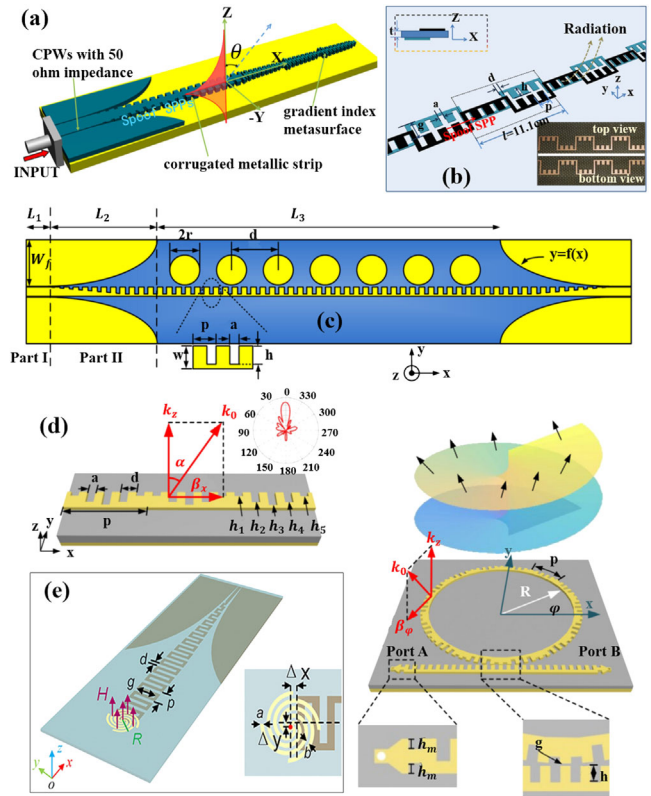

FIG. 35. (a) Schematic of an antenna design based on the propagation of conformal surface plasmon modes on an ultrathin corrugated metal strip that displays a phase-gradient modulation. From Xu *et al.*, 2015. (b) Schematic of the proposed structure for the analog of Cherenkov radiation wakes. From Xu *et al.*, 2017. The structure is composed of a plurality of balanced transmission line segments periodically interconnected with a matching stub. Inset: photograph of the fabricated phase-reversal structure. (c) Schematic of a beam scanning patch array fed by spoof SPs propagating in an ultrathin corrugated metallic transmission line. From Yin *et al.*, 2016. (d) Left panel: schematic view of a triangularly modulated spoof SP waveguide that acts as a leaky-wave antenna. From Liao, Zhou *et al.*, 2020. Inset: the far-field radiation pattern. Right panel: illustration of a ring resonator that is coupled to an access waveguide for wave input. (e) An antenna design that operates by coupling an ultrathin corrugated metal strip supporting conformal surface plasmons with an ultrathin metallic disk textured with spiral-shaped grooves. From Liao, Luo *et al.*, 2020.

sensing device for dynamic sweat secretion analysis (Nyein *et al.*, 2018).

It is known that the widespread use of terahertz spectroscopy in sensing applications is greatly obstructed by the scarcity of good sources and the less efficient sensitivity of detectors in this frequency regime. The tightly confined nature of terahertz spoof SPs anticipates that they can be sensitive to the dielectric environment and could significantly facilitate terahertz sensing (Liu *et al.*, 2013; Ng *et al.*, 2013; Ma *et al.*, 2017). For example, Ng *et al.* (2013) introduced a spoof SP–based metamaterial to demonstrate refractive index sensing of various fluids in an Otto prism setup [shown in Figs. 36(a)–36(c)]. In addition to this narrowband device, broadband terahertz sensing has been experimentally achieved
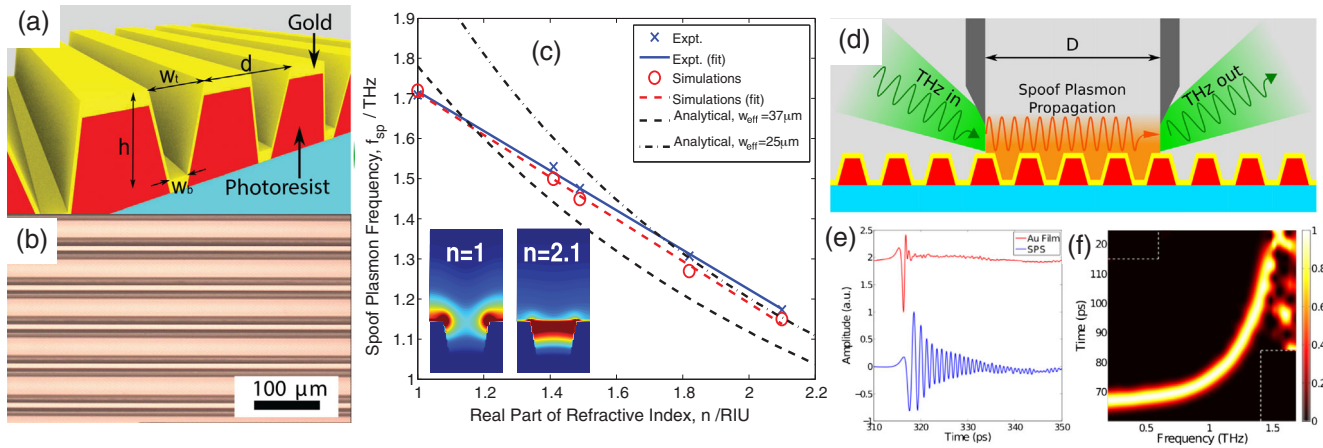
FIG. 36. (a) 3D image of a metamaterial based on spoof SP modes propagating on a 1D grating. The red region depicts the photoresist grooves, and the yellow region depicts the gold film. (b) Optical microscope image of the fabricated groove array. (c) Resonance frequencies of various fluids f_{sp} plotted against refractive indices for experiments (blue solid line, crosses), simulations (red dashed line, open circles), and analytical expressions with $w_{eff} = 37\ \mu m$ (black dotted line) and $w_{eff} = 25\ \mu m$ (black dash-dotted line). Insets: electric energy density distributions for $n = 1$ and $n = 2.1$ evaluated at f_{sp}. From Ng *et al.*, 2013. (d) The scattering edge coupling configuration. (e) Scattering edge coupled time-domain signal of a flat Au film (red line) and corrugated Au film (blue line) with $D = 8$ mm. (f) Filtered spectrogram associated with the corrugated Au film with $D = 8$ mm. (d)–(f) From Ng *et al.*, 2014.

based on spoof SPs. As shown in Figs. 36(d)–36(f), in corrugated metallic surfaces consisting of a linear array of subwavelength grooves it is possible to discern the group velocity characteristics of a spoof SP pulse, which in turn allows extracting broadband dispersion data from 0.4 to 1.44 THz in a single measurement (Ng *et al.*, 2014). Together with the capability to integrate spoof SP surfaces with microfluidics and the flexibility in the design of their EM properties, these surfaces provide a versatile platform for on-chip broadband terahertz sensing.

Plasmonic sensors operating in the optical regime are regarded as an exciting advance in biomedical engineering due to their real-time, label-free, and ultrasensitive monitoring features (Homola, 2008). However, their comprehensive application remains impeded by the poor modulation properties of the operating frequency, single amplitude characterization method and is limited to low-loss substances. Based on spoof SPs, terahertz wave absorption and propagation characteristics in metallic meshes can be designed for terahertz sensing and its application in the biomedical field (Tabata, 2015). By combining steerable plasmonic resonances and attenuated total reflection, an ultraprecise terahertz sensor has been realized with direct phase readout capacity (Huang *et al.*, 2020).

B. Active devices based on spoof SPs

Several plasmonic devices leading to amplification and lasing in the visible and telecom regimes have already been constructed by integrating different metallic structures and gain materials (Oulton *et al.*, 2009; Berini and De Leon, 2012). Along these lines, stimulated emission of SPPs at telecom wavelengths with erbium-doped glass as a gain medium have been demonstrated (Ambati *et al.*, 2008). This type of structure has also been used in the design of plasmonic amplifiers and lasers. Active control over SPPs has

been realized by using a digital spatial light modulator (Gjonaj *et al.*, 2011) that could be used to design devices for sensing, photovoltaics, quantum communication, nanocircuitry, and superresolution microscopy. Furthermore, a modulator composed of a hybrid plasmonic waveguide with a length of only 1.5 μm has been built up (Lu *et al.*, 2017). The operation of this device is based on an electrically controlled light propagation in the plasmonic waveguide with a sandwiched graphene monolayer.

To transfer the advantages of strong field confinement and high efficiency of surface plasmons to the microwave regime, broadband amplification of spoof SPs [see Fig. 37(a)] has been also proposed (Zhang, Liu *et al.*, 2015). This spoof SP–based active device is composed of a low-noise amplifier chip produced by semiconductor technology and a spoof SP–based transmission line that contains two ultrathin corrugated metallic strips on the top and bottom surfaces of a dielectric substrate with mirror symmetry. In this way, spoof SPs can be amplified with a high gain of around 20 dB. To realize attenuation, amplification, and transmission simultaneously, a dynamically tunable integrated device based on a combination of a spoof SP waveguide and graphene [see Fig. 37(b)] was proposed (Chen *et al.*, 2020). By changing the bias voltage applied to the graphene sandwich, amplification gain and attenuation of the spoof SP propagating in the transmission line could be dynamically tuned from 15 to −10 dB, respectively.

Nonlinear devices are also important components in EM technology, as they can provide different frequency responses to an incident wave, such as frequency multiplication and mixing. However, light-matter coupling is usually weak for common materials, and nonlinear effects can thus rarely be used in real applications. Hence, to obtain highly efficient nonlinear devices, some special structures or materials (i.e., diodes or transistors) must be added to enhance nonlinear phenomena. Among them, spoof SP technology is a potential
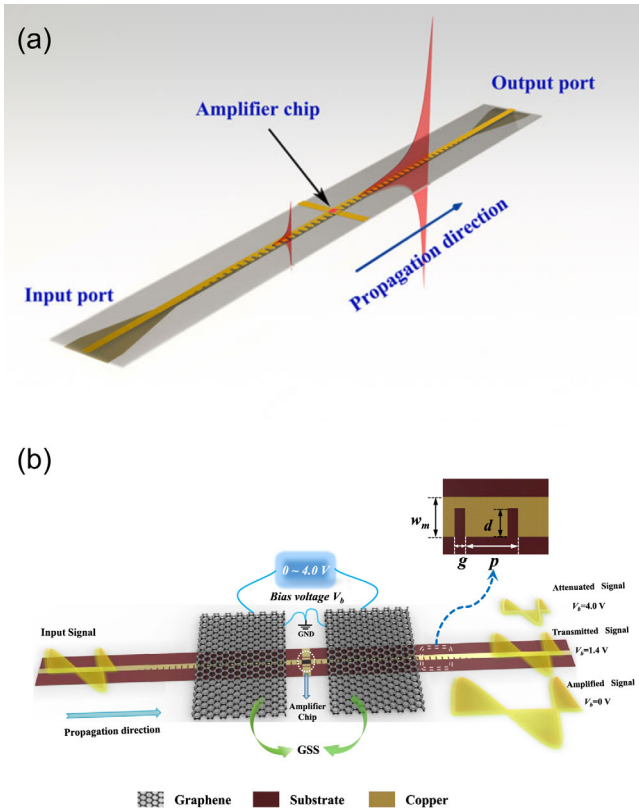
FIG. 37. (a) Broadband amplification of spoof SPs at microwave frequencies using a low-noise amplifier chip produced with semiconductor technology. From Zhang, Liu *et al.*, 2015. (b) Dynamically tunable integrated device for attenuation, amplification, and transmission of spoof SPs using graphene. From Chen *et al.*, 2020.
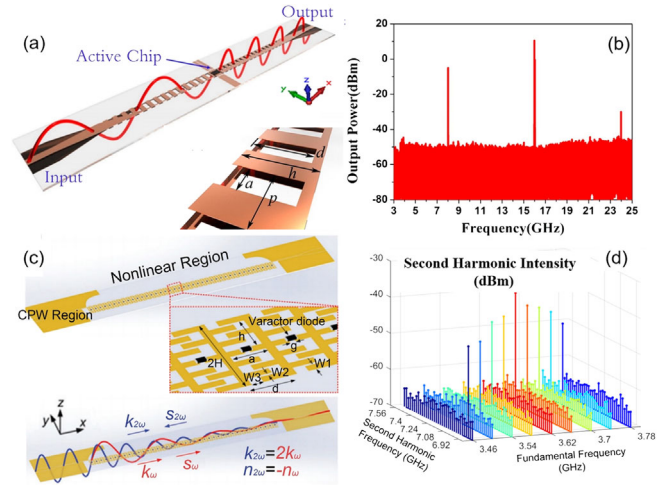

FIG. 38. (a) Schematic showing the generation of second-harmonic spoof SPs through a subwavelength-scale nonlinear active chip integrated in a spoof SP waveguide composed of two antisymmetric ultrathin corrugated metallic strips. (b) Measured frequency spectrum of the second-harmonic generator depicted in (a) when the fundamental frequency is 8 GHz. (a),(b) From Zhang, Fan *et al.*, 2016. (c) Schematic showing the backward phase-matching effect using spoof SP modes. The red and blue lines represent the fundamental frequency (FF) and second-harmonic waves, respectively. (d) Associated frequency-doubled signals emerging from the device depicted in (c). At each excitation frequency f_{FF}, the output signal features a distinct peak at $2 \times f_{FF}$. (c),(d) From Liu *et al.*, 2018.

candidate for real circuitry applications, owing to its known capacity to enhance EM fields. Along these lines, the interaction between a spoof SP mode supported by a corrugated waveguide and a Kerr nonlinear material was theoretically analyzed using finite-difference time-domain modeling in the terahertz regime by Song and Mazumder (2012). They proved that this architecture indeed provides both a high Q factor and strong light localization, leading to an enhanced slowdown factor such that a nonlinear response emerges in the structure despite the fact that the inherent nonlinearity of the base material is extremely small. A demonstration of non-linear effects using spoof SPs was also experimentally achieved (Zhang, Fan *et al.*, 2016) by directly integrating a nonlinear field-effect transistor chip within a spoof SP–based transmission line. This device acts as a second-harmonic generator of a spoof SP wave, as shown in Fig. 38(a). Thanks to the low-pass feature of these spoof SP–based waveguides, this structure can also suppress the unwanted high-order harmonics. Based on this design, both a threefold frequency conversion gain and significant high-order harmonic suppression were reported. This structure can be directly used in the system as a double multiplier device, as rendered in Fig. 38(b).

However, designs based on transistors need an extra dc supply, which leads to increased complexity in the system. To solve the problem, Liu *et al.* (2018) investigated the use of backward phase-matching technology using a negative-index

platform based on conformal surface plasmons, in which the fundamental and second-harmonic components can be separated through different posts, as shown Figs. 38(c) and 38(d). In this way, a second-harmonic spoof SP mode with negative group velocity is observed at the phase-matching point. The measured highest conversion is about 0.07%, which is limited mainly by the coherence length and input power. Thereafter, an improved reconfigured design was proposed to achieve a higher conversion efficiency (i.e., a 0.8% measurement), which can also switch the backward and forward second-harmonic signals by introducing different kinds of varactor diodes (Gao, Zhang, Zhang *et al.*, 2020).

Based on the capabilities of surface plasmons in the optical range, tunable plasmonic devices were also proposed, aiming to obtain variable functionalities without changing the underlying structure. An actively controlled device was created based on the index-sensitive properties of surface plasmons (Wang *et al.*, 2016). This tunable design can realize continuous and reversible control of the wavelength of the transmitted light by modulating the external voltage applied to a liquid crystal layer. Microlight sources and switches could be devised using the same concept. The entire transmission spectrum can also be tuned by introducing a parallel interfaced pair of graphene layers separated by two spatial silver strips (Li *et al.*, 2015). This idea provides a method of fabricating active nanointegrated circuits that operate in the midinfrared regime for optical processing. Moreover, a graphene-based metasurface was recently proposed to exhibit multifunctions, including a tunable filter and slow-light behavior, which result
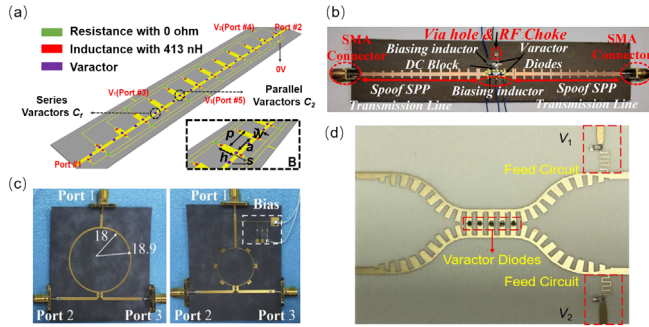
FIG. 39. (a) Schematic of a reconfigurable bandpass filter for spoof SPs that includes integrated passive lumped elements, tunable varactors, a dc bias network, and active conversion elements between the corrugated waveguide and the microstrip line. From Zhang, He *et al.*, 2018. (b) Fabricated prototype of a reconfigurable bandpass filter based on spoof SPs. From Jaiswal, Pandit, and Pathak, 2019a. (c) Photographs of Wilkinson power dividers working at around 1 GHz, with impedance transformers based on conventional microstrip lines (left panel) and ultrathin corrugated metal strips supporting conformal surface plasmons (right panel). From Zhang, Zhu *et al.*, 2018. (d) Photograph of a reconfigurable device based on spoof SPs. From Gao, Zhang, Wu *et al.*, 2020.

from the graphene plasmons and the phenomenon of plasmon-induced transparency, respectively (Jiang *et al.*, 2020).

At microwave frequencies, various tunable devices have been also delivered using spoof SP waves as basic components, by replacing conventional SPPs. A bandpass filter was proposed (Zhang, He *et al.*, 2018) whose cutoff frequencies at both sides of the passband can be controlled by changing the direct current bias of the varactors; see Fig. 39(a). Similarly, another bandpass filter using T-shaped spoof SP resonators was designed (Jaiswal, Pandit, and Pathak, 2019a) whose central frequency and bandwidth are both reconfigurable; see Fig. 39(b). In addition, the operating band can be tuned by using different spoof SP modes. An electronically controlled programmable transmission line has also been presented, with a dispersion that can be manipulated in real time by programming the bias voltage (Wang *et al.*, 2019). Because its second-order spoof SP mode cannot propagate, a filter with rejection bands that can be freely reconfigured in real time was achieved. Moreover, a frequency-reconfigurable and compact Wilkinson power divider was designed and fabricated using spoof SP–based waveguides (Zhang, Zhu *et al.*, 2018), which are periodically loaded with varactors and short-circuit stubs, as depicted in Fig. 39(c). Numerical results show a 35% frequency tunability and a footprint reduced to 46% of that associated with a conventional microstrip. A single programmable spoof SP device can display high-efficiency transmission, unequal directional coupling, and crossover transmission with a better isolation effect (Gao, Zhang, Wu *et al.*, 2020). Figure 39(d) shows a photograph of this reconfigurable device. The active control of all these functionalities is achieved by programming the bias voltages of the varactor diodes dynamically in such a way that the coupled surface EM waves propagating on the waveguides can be independently controlled.

Modulation technology is the basis of modern communication systems, including plasmonic ones (Xiao *et al.*, 2015; Zhang, Sun *et al.*, 2016). A 70 GHz plasmonic Mach-Zehnder modulator was reported with a dramatic reduction of size, low energy consumption, and ultrahigh speed (Haffner *et al.*, 2015). Plasmonic modulation offers broad electrical bandwidth in a simple and compact configuration with a length of less than 10 μm. This device fits into a silicon waveguide, which results in a notably low energy consumption of 25 fJ/bit up to the highest speeds and anticipates a cheap cointegration with electronics. Through a dense four-channel plasmonic phase modulator array that directly interconnects an optical fiber array, an ultracompact terabit transmitter solution was proposed (Koch *et al.*, 2019). This array can offer data rates of 0.8 Tbits/s on a 90×5.5 μm^2 footprint and enables new options for dense cointegration with electronics. To solve the integration problem of terahertz links into the existing fiber-optic infrastructures, an ultrabroadband plasmonic modulator was proposed (Ummethala *et al.*, 2019). Such a modulator can build a bridge of data streams between the terahertz and optical domains, leading to terahertz-to-optical conversion in wireless communications.

At lower frequencies, plasmonic modulators have to be realized using spoof SPs. Based on dynamical switching between discrete dispersion states, a new approach for active dispersion engineering based on digital control was proposed (Zhang, Cui *et al.*, 2020; Zhang, Zhang, Tang *et al.*, 2020). Spoof SP waves can be operated in three different domains (amplitude, frequency, and phase) by constructing digital spoof SP modulators, as shown in Fig. 40. This flexibility makes these modulators effective and reliable candidates for the manipulation of spoof SP waves in advanced modulation technology. In addition, there are not any foreseen challenges hindering the application of digital spoof SPs in the terahertz
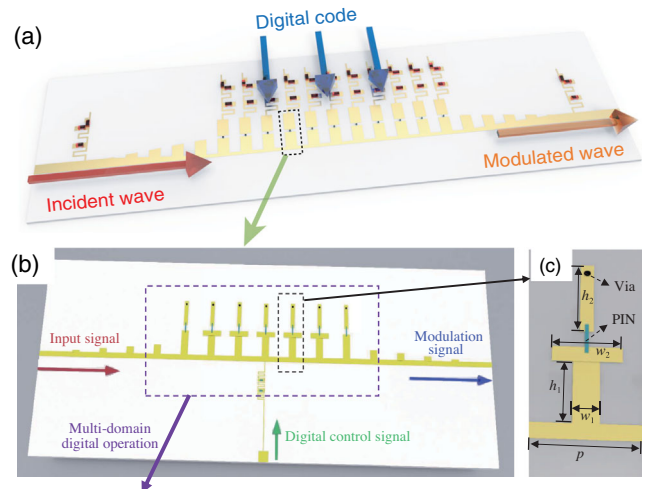

FIG. 40. Modulators based on spoof SPs. (a) Schematic of a prototype of a digital spoof SP waveguide. Here the modulation is achieved with the direct interaction between the incident spoof SP wave and a digital code. From Zhang, Cui *et al.*, 2020. (b) A multischeme modulation spoof SP waveguide whose main part is outlined with the purple dashed line. (c) Schematic of a single switchable spoof SP unit in which the period $p = 6$ mm. (b), (c) From Zhang, Zhang, Tang *et al.*, 2020.

regime, implying a promising prospect in both plasmonic and digital system research.

C. Communication systems based on spoof SPs

Plasmonic systems are considered potential candidates to overcome the speed limitation of electronic circuitry and the current critical dimensions of photonics in the optical and telecom ranges. They have been proposed for different applications ranging from sensing to telecommunications (MacDonald *et al.*, 2009; Mitchell, 2010; Sorger *et al.*, 2012; Huang *et al.*, 2014; Rodrigo *et al.*, 2015; Krasavin and Zayats, 2016). Regarding wireless communication, frequencies of the carrier waves reside in the microwave, millimeter, and terahertz ranges rather than in the visible regime. For example, the fifth generation and future sixth generation communication systems are expected to operate in those frequency ranges (Rappaport *et al.*, 2013, 2019; Andrews *et al.*, 2014; Saad, Bennis, and Chen, 2020), owing to their stronger non–line-of-sight transmissions. That is why spoof SPs are expected to play an important role in implementing these future communication systems.

Indeed, recently a wireless body sensor network entirely based on spoof SP components was designed and implemented (Tian *et al.*, 2019). Some pictures of this system, which is composed of antennas, beam splitters, and ring resonators, are rendered in Fig. 41. Thanks to the extreme subwavelength confinement of the spoof SP modes that act as EM carriers in this system, the transmission efficiency of wireless networks can be enhanced by more than 3 orders of magnitude compared to conventional radiative networks. Moreover, wireless communication can be highly localized in a region close to the body (around 10 cm), enabling efficient transmission between the different components without radiation into the surrounding space. These two capabilities allow

for an energy-efficient and secure wireless communication, in contrast to other schemes based on radiative networks.

One of the main limitations of traditional microwave technology for wireless communication is that two or more microwave signals carried out by waveguides that are separated a subwavelength distance cannot be distinguish in the far field due to diffraction effects. As a result, EM signals need to be nonlinear and gain-operated within the propagation channels, which is difficult to achieve using standard technology such as metalenses and plasmonic lenses (Kaina *et al.*, 2015; Pacheco-Pena *et al.*, 2017). To overcome this difficulty, Zhang, Zhang, He *et al.* (2020) recently realized a wireless communication system that is based entirely on spoof SP components. The propagation channels are constructed first by integrated spoof SP waveguides and active chips. Owing to the extreme field confinement associated with spoof SPs, the waveguides present less discontinuous radiation, smaller coupling between adjacent channels, and higher receiver sensitivity than traditional microstrip channels. In the experimental setup, Zhang, Zhang, He *et al.* (2020) designed an integrated two-channel system based on conformal surface plasmons and packaged it in a compact space (smaller than 1/10 wavelength), as shown in Fig. 42(a). In this system,
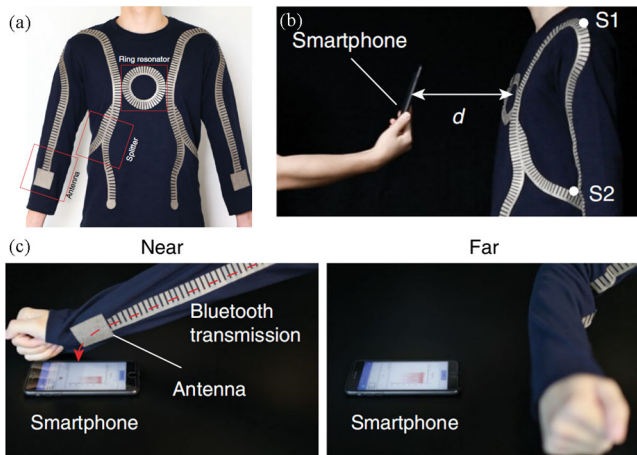

FIG. 41. (a) Metamaterial textile network integrating different elements, such as splitters, antennas, and a ring resonator, made of ultrathin corrugated metal structures capable of supporting both propagating spoof SPs and spoof LSPs. (b) Wireless communication between two sensor nodes (labeled S1 and S2) and a smartphone at a distance *d* from the body. (c) Bluetooth transmission of the electrocardiography waveform along the sleeve to a textile-integrated antenna. From Tian *et al.*, 2019.
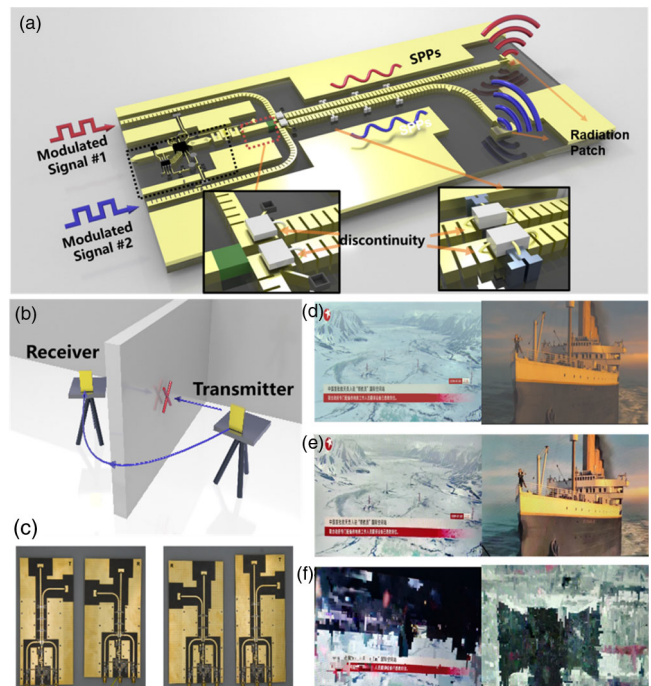

FIG. 42. (a) Schematic of the operation principle of the spoof SP–based system, which is composed of two independent signal-processing channels with a deep-subwavelength-scale separation and a shared continuous-wave oscillator. (b) Test scenario schematic of a line-of-sight real-time transmission, where the wireless signal emitted by the transmitter goes through the barrier and is received by the receiver. (c) Photographs of the fabricated spoof SP–based wireless communication system (left panel) and the conventional microstrip-based system (right panel). (d) Frames of the two original movies to be transmitted. The same frames as decoded with the receiver after being transmitted (e) by the spoof SP–based system and (f) by the conventional microstrip system. From Zhang, Zhang, He *et al.*, 2020.

a shared local oscillator with a 10 GHz frequency provides the carrier EM waves for the intermediate frequency signals. Two digital signals with spectral components of around 1.9 GHz are modulated by the radio frequency carrier waves through a spoof SP harmonic mixer that also includes the mixing functionality. The obtained modulated signals are poured into the designed spoof SP channels while packaged in a compact space and amplified during propagation. After multistage amplifications, two amplified signals are radiated by two identically designed but orthogonally polarized wide-angle patch antennas and collected by the receiver. To test the reliability of this scheme by confronting it with standard microstrip technology, robust line-of-sight real-time communication experiments were performed in a demanding scenario in which a barrier is located between the transmitter and receiver to block the line of sight, as shown in Fig. 42(b). For visualization, two different movies in 4K resolution (*Titanic* and *The Wandering Earth*) are selected as simultaneous input signals. The frames received in the spoof SP–based system [see Fig. 42(e)] are synchronized in both image quality and time with the original frames, as shown in Fig. 42(d). In contrast, the frames received in the microstrip-based system are severely distorted [see Fig. 42(f)], even though the test scenario is completely identical.

VI. SUMMARY AND PERSPECTIVES

In this paper, we have provided a detailed review on the concepts, physical features, and recent developments of spoof SPs over the past several years while focusing primarily on the theoretical framework and related planar structured surfaces, waveguides, resonators, passive and active devices, and communication systems. We have particularly explored the exotic characteristics of spoof SPs in terms of their designable dispersion and propagation properties, flexible EM field confinement and enhancement, and advantages in devising functional devices featuring compact size, high information capacity, and good performance at microwave frequencies.

Although spoof SPs have some properties in common with conventional surface plasmons at optical frequencies, they are not limited to mimicking those surface EM modes at lower frequencies and they display some unique characteristics. One interesting feature of spoof SPs is that they present designable and engineered dispersion and propagation characteristics. Unlike the dispersion relation of optical surface plasmons, which is fixed for a given material, the propagating wave vector of spoof SPs can be controlled by designing the geometry of the guiding system, leading to the possibility of engineering their propagation loss and EM field confinement simply by geometrical means. This capability opens up a large variety of stimulating new avenues for both fundamental and applied research. For example, interesting applications could be found in condensed matter physics. Highly designable spoof SPs could allow us to explore fundamental physics in the high-dimensional quantum Hall effect and in quantized electric multipole insulators.

A second asset of spoof SPs is the easy integration of active devices in their metallic unit cells, which results in reconfigurable dispersion properties and programmable functions. Similarly, resonant frequencies can also be manipulated by

changing the active devices incorporated into spoof LSP–based structures. In the future, the convenient integration of spoof LSP structures with planar circuits will endow LSP sensing with a solid technical foundation and promising prospects, which can be integrated with transducer materials in solid, liquid, and gaseous phases. Therefore, we can foresee a wide range of applications in wearable devices, biomedical engineering, and hazardous gas monitoring.

At microwave frequencies, ultrathin corrugated metallic strips are able to guide conformal surface plasmons, which behave like *microwave fibers* and have become a new type of transmission line. Based on these new waveguides, a large variety of microwave passive devices (such as filters, resonators, and splitters) and active devices (such as amplifiers, multipliers, and antennas) have already been fabricated. All these developments have directly resulted in the design and construction of the first full spoof SP–chain transmitter and receiver system for wireless communication. This system can transmit two independent movies transported by subwavelength-scale channels, thereby displaying a much better performance than traditional microwave technology. In fact, this new technology based on spoof SPs has opened up a promising new direction within microwave research. In the future, more active devices based on spoof SPs, such as oscillators, mixers, power amplifiers, and low-noise amplifiers, are expected to be the basis of more complex and functional systems.

Finally, spoof SPs are also expected to play an important role in microwave and terahertz circuitry, which have wide applications in security, nursing, and daily care due to their flexible and wearable nature. They can also be combined with the current CMOS technology to develop spoof SP–based integrated circuits, which can solve problems with high cross talk and signal distortion in the traditional technologies. Hence, they have great application potential in both data-oriented computing and wideband on-chip communication between memory and microprocessor cores. We foresee that these new transmission lines and passive and active components will enhance future CMOS technology. Additionally, recent studies show that spoof SPs can modulate digital information directly, evolving digital spoof SPs at microwave frequencies. Thus, spoof SPs also have the potential to significantly improve the design of digital-analogic joint systems, which may lead to new frameworks in future electronic and information systems.

REFERENCES

Aghadjani, M., and P. Mazumder, 2015, IEEE Trans. Terahertz Sci. Technol. **5**, 556.

Agranovich, V. M., and D. L. Mills, 1982, *Surface Polaritons* (North-Holland, Amsterdam).

Ambati, M., S. H. Nam, E. Ulin-Avila, D. A. Genov, G. Bartal, and X. Zhang, 2008, Nano Lett. **8**, 3998.

Andrews, J. G., S. Buzzi, W. Choi, S. V. Hanly, A. Lozano, A. C. Soong, and J. C. Zhang, 2014, IEEE J. Sel. Areas Commun. **32**, 1065.

Andrews, S. R., 2014, J. Phys. D **47**, 374004.

Anker, J. N., W. P. Hall, O. Lyandres, N. C. Shah, J. Zhao, and R. P. Van Duyne, 2008, Nat. Mater. **7**, 442.

Arikawa, T., T. Hiraoka, S. Morimoto, F. Blanchard, S. Tani, T. Tanaka, K. Sakai, H. Kitajima, K. Sasaki, and K. Tanaka, 2020, Sci. Adv. **6**, eaay1977.

Atwater, H. A., and A. Polman, 2010, Nat. Mater. **9**, 205.

Berini, P., 2000, Phys. Rev. B **61**, 10484.

Berini, P., 2009, Adv. Opt. Photonics **1**, 484.

Berini, P., and I. De Leon, 2012, Nat. Photonics **6**, 16.

Beruete, M., M. Sorolla, I. Campillo, J. S. Dolado, L. Martín-Moreno, J. Bravo-Abad, and F. J. García-Vidal, 2004, Opt. Lett. **29**, 2500.

Boltasseva, A., V. S. Volkov, R. B. Nielsen, E. Moreno, S. G. Rodrigo, and S. I. Bozhevolnyi, 2008, Opt. Express **16**, 5252.

Botten, L. C., and R. C. McPhedran, 1985, Opt. Acta **32**, 1479.

Bouhelier, A., M. Beversluis, A. Hartschuh, and L. Novotny, 2003, Phys. Rev. Lett. **90**, 013903.

Bozhevolnyi, S. I., V. S. Volkov, E. Devaux, J.-Y. Laluet, and T. W. Ebbesen, 2006, Nature (London) **440**, 508.

Brock, E. M. G., E. Hendry, and A. P. Hibbins, 2011, Appl. Phys. Lett. **99**, 051108.

Caglayan, H., and E. Ozbay, 2008, Opt. Express **16**, 19091.

Chen, H.-T., A. J. Taylor, and N. Yu, 2016, Rep. Prog. Phys. **79**, 076401.

Chen, L., Y. Wei, X. Zang, Y. Zhu, and S. Zhuang, 2016, Sci. Rep. **6**, 22027.

Chen, L., N. Xu, L. Singh, T. Cui, R. Singh, Y. Zhu, and W. Zhang, 2017, Adv. Opt. Mater. **5**, 1600960.

Chen, Y., Z. Song, Y. Li, M. Hu, Q. Xing, Z. Zhang, L. Chai, and C.-Y. Wang, 2006, Opt. Express **14**, 13021.

Chen, Z. P., W. B. Lu, Z. G. Liu, A. Q. Zhang, B. Wu, and H. Chen, 2020, IEEE Trans. Antennas Propag. **68**, 3953.

Chern, R.-L., C. C. Chang, and C. C. Chang, 2006, Phys. Rev. E **73**, 036605.

Collin, S., F. Pardo, and J.-L. Pelouard, 2007, Opt. Express **15**, 4310.

Collin, S., F. Pardo, R. Teissier, and J. L. Pelouard, 2001, Phys. Rev. B **63**, 033107.

Collin, S., C. Sauvan, C. Billaudeau, F. Pardo, J. C. Rodier, J. L. Pelouard, and P. Lalanne, 2009, Phys. Rev. B **79**, 165405.

Dai, J., S. A. Dyakov, S. I. Bozhevolnyi, and M. Yan, 2016, Phys. Rev. B **94**, 125431.

Dai, J., S. A. Dyakov, and M. Yan, 2015, Phys. Rev. B **92**, 035419.

Dai, J., S. A. Dyakov, and M. Yan, 2016, Phys. Rev. B **93**, 155403.

de Abajo, F. J. G., and J. J. Saenz, 2005, Phys. Rev. Lett. **95**, 233901.

de Abajo, F. J. G., J. J. Sáenz, I. Campillo, and J. S. Dolado, 2006, Opt. Express **14**, 7.

de León-Pérez, F., G. Brucoli, F. J. García-Vidal, and L. Martín-Moreno, 2008, New J. Phys. **10**, 105017.

Du, M., Y. Feng, K. Chen, and J. Zhao, 2020, J. Phys. D **53**, 165105.

Duan, J., H. Guo, S. Dong, T. Cai, W. Luo, Z. Liang, Q. He, L. Zhou, and S. Sun, 2017, Sci. Rep. **7**, 1.

D'yakonov, M. I., 1988, Sov. Phys. JETP **67**, 714.

Ebbesen, T. W., H. J. Lezec, H. F. Ghaemi, T. Thio, and P. A. Wolff, 1998, Nature (London) **391**, 667.

Economou, E. N., 1969, Phys. Rev. **182**, 539.

Fan, B., D. Filonov, P. Ginzburg, and V. A. Podolskiy, 2018, Opt. Express **26**, 17541.

Fernández-Domínguez, A. I., L. Martín-Moreno, F. J. García-Vidal, S. R. Andrews, and S. A. Maier, 2008, IEEE J. Sel. Top. Quantum Electron. **14**, 1515.

Fernández-Domínguez, A. I., E. Moreno, L. Martín-Moreno, and F. J. García-Vidal, 2009a, Phys. Rev. B **79**, 233104.

Fernández-Domínguez, A. I., E. Moreno, L. Martín-Moreno, and F. J. García-Vidal, 2009b, Opt. Lett. **34**, 2063.

Fernández-Domínguez, A. I., C. R. Williams, L. Martín-Moreno, F. J. García-Vidal, S. R. Andrews, and S. A. Maier, 2008, Appl. Phys. Lett. **93**, 141109.

Fu, T., X. Liu, G. Xiao, T. Sun, and H. Li, 2020, Opt. Express **28**, 38934.

Fu, Z., Q. Gan, Y. J. Ding, and F. J. Bartoli, 2008, IEEE J. Sel. Top. Quantum Electron. **14**, 486.

Gan, Q., Z. Fu, Y. J. Ding, and F. J. Bartoli, 2007, Opt. Express **15**, 18050.

Gan, Q., Z. Fu, Y. J. Ding, and F. J. Bartoli, 2008, Phys. Rev. Lett. **100**, 256803.

Gao, F., Z. Gao, Y. Luo, and B. Zhang, 2016, Adv. Funct. Mater. **26**, 8307.

Gao, F., Z. Gao, X. Shi, Z. Yang, X. Lin, and B. Zhang, 2015, Opt. Express **23**, 6896.

Gao, F., *et al.*, 2016, Nat. Commun. **7**, 11619.

Gao, X., J. H. Shi, H. F. Ma, W. X. Jiang, and T. J. Cui, 2012, J. Phys. D **45**, 505104.

Gao, X., J. H. Shi, X. Shen, H. F. Ma, W. X. Jiang, L. Li, and T. J. Cui, 2013, Appl. Phys. Lett. **102**, 151912.

Gao, X., L. Zhou, and T. J. Cui, 2015, Sci. Rep. **5**, 9250.

Gao, X., L. Zhou, X. Y. Yu, W. P. Cao, H. O. Li, H. F. Ma, and T. J. Cui, 2015, Opt. Express **23**, 23270.

Gao, X. X., H. C. Zhang, L. W. Wu, Z. X. Wang, P. H. He, Z. Gao, and T. J. Cui, 2020, IEEE Trans. Antennas Propag. **68**, 3770.

Gao, X. X., J. J. Zhang, H. C. Zhang, L. L. Liu, Q. Ma, P. Xu, and T. J. Cui, 2020, Adv. Opt. Mater. **8**, 1902058.

Gao, Z., F. Gao, H. Xu, Y. Zhang, and B. Zhang, 2016, Opt. Lett. **41**, 2181.

Gao, Z., F. Gao, Y. Zhang, X. Shi, Z. Yang, and B. Zhang, 2015, Appl. Phys. Lett. **107**, 041118.

Gao, Z., F. Gao, Y. Zhang, H. Xu, Y. Luo, and B. Zhang, 2017, Adv. Mater. **29**, 1700018.

Gao, Z., F. Gao, Y. Zhang, and B. Zhang, 2015, Appl. Phys. Lett. **107**, 191103.

Gao, Z., F. Gao, Y. Zhang, and B. Zhang, 2016d, Phys. Rev. B **93**, 195410.

Gao, Z., L. Shen, and X. Zheng, 2012, IEEE Photonics Technol. Lett. **24**, 1343.

Gao, Z., Z. Yang, F. Gao, H. Xue, Y. Yang, J. Dong, and B. Zhang, 2017, Phys. Rev. B **96**, 201402.

Gao, Z., X. Zhang, and L. Shen, 2010, J. Appl. Phys. **108**, 113104.

García-Etxarri, A., R. Gómez-Medina, L. S. Froufe-Pérez, C. López, L. Chantada, F. Scheffold, J. Aizpurua, M. Nieto-Vesperinas, and J. J. Sáenz, 2011, Opt. Express **19**, 4815.

Garcia-Vidal, F. J., L. Martin-Moreno, T. W. Ebbesen, and L. Kuipers, 2010, Rev. Mod. Phys. **82**, 729.

García-Vidal, F. J., L. Martín-Moreno, and J. B. Pendry, 2005, J. Opt. A **7**, S97.

García-Vidal, F. J., E. Moreno, J. A. Porto, and L. Martín-Moreno, 2005, Phys. Rev. Lett. **95**, 103901.

García-Vidal, F. J., and J. B. Pendry, 1996, Phys. Rev. Lett. **77**, 1163.

Gjonaj, B., J. Aulbach, P. M. Johnson, A. P. Mosk, L. Kuipers, and A. Lagendijk, 2011, Nat. Photonics **5**, 360.

Glybovski, S. B., S. A. Tretyakov, P. A. Belov, Y. S. Kivshar, and C. R. Simovski, 2016, Phys. Rep. **634**, 1.

Gobau, G., 1950, J. Appl. Phys. **21**, 1119.

Gong, S., K. Ogura, K. Yambe, S. Nomizu, A. Shirai, K. Yamazaki, J. Kawamura, T. Miura, S. Takanashi, and M. T. San, 2015, J. Appl. Phys. **118**, 123101.

Gramotnev, D. K., and S. I. Bozhevolnyi, 2010, Nat. Photonics **4**, 83.

Guan, D., P. You, Q. Zhang, K. Xiao, and S. Yong, 2017, IEEE Trans. Microwave Theory Tech. **65**, 4925.

Guan, D., P. You, Q. Zhang, Z. Yang, H. Liu, and S. Yong, 2018, IEEE Trans. Microwave Theory Tech. **66**, 2946.

Guérout, R., J. Lussange, F. S. S. Rosa, J.-P. Hugonin, D. A. R. Dalvit, J.-J. Greffet, A. Lambrecht, and S. Reynaud, 2012, Phys. Rev. B **85**, 180301.

Gupta, B., S. Pandey, and A. Nahata, 2014, Opt. Express **22**, 2868.

Haffner, C., *et al.*, 2015, Nat. Photonics **9**, 525.

Hao, J. M., L. Zhou, and C. T. Chan, 2007, Appl. Phys. A **87**, 281.

Hendry, E., A. P. Hibbins, and J. R. Sambles, 2008, Phys. Rev. B **78**, 235426.

Hibbins, A. P., B. R. Evans, and J. R. Sambles, 2005, Science **308**, 670.

Hibbins, A. P., E. Hendry, M. J. Lockyear, and J. R. Sambles, 2008, Opt. Express **16**, 20441.

Hibbins, A. P., M. J. Lockyear, I. R. Hooper, and J. R. Sambles, 2006, Phys. Rev. Lett. **96**, 073904.

Hibbins, A. P., M. J. Lockyear, and J. R. Sambles, 2007, Phys. Rev. B **76**, 165431.

Hibbins, A. P., J. R. Sambles, C. R. Lawrence, and J. R. Brown, 2004, Phys. Rev. Lett. **92**, 143904.

Homola, J., 2008, Chem. Rev. **108**, 462.

Huang, C. Y., M. K. Seo, T. Sarmiento, Y. Huo, and M. L. Brongersma, 2014, Nat. Photonics **8**, 244.

Huang, T.-J., J.-Y. Liu, L.-Z. Yin, F.-Y. Han, and P.-K. Liu, 2018, Opt. Express **26**, 22722.

Huang, X.-R., R.-W. Peng, and R.-H. Fan, 2010, Phys. Rev. Lett. **105**, 243901.

Huang, Y., S. C. Zhong, T. T. Shi, Y. C. Shen, and D. X. Cui, 2020, Nanophotonics **9**, 3011.

Huidobro, P. A., A. I. Fernandez-Dominguez, J. B. Pendry, L. Martin-Moreno, and F. J. Garcia-Vidal, 2018, *Spoof Surface Plasmon Metamaterials* (Cambridge University Press, Cambridge, England).

Huidobro, P. A., X. Shen, J. Cuerda, E. Moreno, L. Martin-Moreno, F. J. Garcia-Vidal, T. J. Cui, and J. B. Pendry, 2014, Phys. Rev. X **4**, 021003.

Jaiswal, R. K., N. Pandit, and N. P. Pathak, 2019a, Plasmonics **14**, 1539.

Jaiswal, R. K., N. Pandit, and N. P. Pathak, 2019b, IEEE Photonics Technol. Lett. **31**, 1293.

Jeon, T.-I., J. Zhang, and D. Grischkowsky, 2005, Appl. Phys. Lett. **86**, 161904.

Jiang, T., L. Shen, J.-J. Wu, T.-J. Yang, Z. Ruan, and L. Ran, 2011, Appl. Phys. Lett. **99**, 261103.

Jiang, X. P., D. B. Chen, Z. J. Zhang, J. Huang, K. Wen, J. He, and J. B. Yang, 2020, Opt. Express **28**, 34079.

Joannopoulos, J. D., S. G. Johnson, J. N. Winn, and R. D. Meade, 2008, *Photonic Crystals: Molding the Flow of Light*, 2nd ed. (Princeton University Press, Princeton, NJ).

Johnson, M. B., 2007, Nat. Photonics **1**, 14.

Joy, S. R., M. Erementchouk, H. Yu, and P. Mazumder, 2019, IEEE Trans. Commun. **67**, 599.

Juluri, B. K., S.-C. S. Lin, T. R. Walker, L. Jensen, and T. J. Huang, 2009, Opt. Express **17**, 2997.

Kaina, N., F. Lemoult, M. Fink, and G. Lerosey, 2015, Nature (London) **525**, 77.

Kats, M. A., D. Woolf, R. Blanchard, N. Yu, and F. Capasso, 2011, Opt. Express **19**, 14860.

Khanikaev, A. B., S. H. Mousavi, G. Shvets, and Y. S. Kivshar, 2010, Phys. Rev. Lett. **105**, 126804.

Kianinejad, A., Z. N. Chen, and C.-W. Qiu, 2015, IEEE Trans. Microwave Theory Tech. **63**, 1817.

Kianinejad, A., Z. N. Chen, and C.-W. Qiu, 2016, IEEE Trans. Microwave Theory Tech. **64**, 3078.

Kim, S.-H., T.-T. Kim, S. Oh, J.-E. Kim, H. Park, and C.-S. Kee, 2011, Phys. Rev. B **83**, 165109.

Kim, S.-H., S. S. Oh, K.-J. Kim, J.-E. Kim, H. Y. Park, O. Hess, and C.-S. Kee, 2015, Phys. Rev. B **91**, 035116.

Koch, U., *et al.*, 2019, J. Lightwave Technol. **37**, 1484.

Kong, G. S., H. F. Ma, B. G. Cai, and T. J. Cui, 2016, Sci. Rep. **6**, 29600.

Konoplev, I. V., L. Fisher, K. Ronald, A. W. Cross, A. D. R. Phelps, C. W. Robertson, and M. Thumm, 2010, Appl. Phys. Lett. **96**, 231111.

Konoplev, I. V., A. J. MacLachlan, C. W. Robertson, A. W. Cross, and A. D. R. Phelps, 2012, Appl. Phys. Lett. **101**, 121111.

Krasavin, A. V., and A. V. Zayats, 2016, Proc. IEEE **104**, 2338.

Kreibig, U., and M. Vollmer, 1995, *Optical Properties of Metal Clusters* (Springer, Berlin).

Krenn, J. R., *et al.*, 1999, Phys. Rev. Lett. **82**, 2590.

Kumar, G., S. Li, M. M. Jadidi, and T. E. Murphy, 2013, New J. Phys. **15**, 085031.

Kuznetsov, A. I., A. E. Miroshnichenko, Y. H. Fu, J. Zhang, and B. Luk'yanchuk, 2012, Sci. Rep. **2**, 492.

Lan, Y.-C., and R.-L. Chern, 2006, Opt. Express **14**, 11339.

Landau, L., J. Bell, M. Kearsley, L. Pitaevskii, E. Lifshitz, and J. Sykes, 2013, *Electrodynamics of Continuous Media*, Course of Theoretical Physics (Elsevier Science, Amsterdam).

Lee, E. S., J.-K. So, G.-S. Park, D. Kim, C.-S. Kee, and T.-I. Jeon, 2012, Opt. Express **20**, 6116.

Lee, J., K. Lee, H. Park, G. Kang, D.-H. Yu, and K. Kim, 2010, Opt. Lett. **35**, 2254.

Lee, R., B. Wang, and M. A. Cappelli, 2017, Appl. Phys. Lett. **111**, 261105.

Lezec, H. J., A. Degiron, E. Deveux, R. A. Linke, L. Martín-Moreno, F. J. García-Vidal, and T. W. Ebbesen, 2002, Science **297**, 820.

Li, H. J., L. L. Wang, Z. R. Huang, B. Sun, and X. Zhai, 2015, Plasmonics **10**, 39.

Li, S., M. M. Jadidi, T. E. Murphy, and G. Kumar, 2013, Opt. Express **21**, 7041.

Li, X., T. Jiang, L. Shen, and X. Deng, 2013, Appl. Phys. Lett. **102**, 031606.

Li, Z., L. Liu, A. I. Fernandez-Dominguez, J. Shi, C. Gu, F. J. Garcia-Vidal, and Y. Luo, 2019, Adv. Opt. Mater. **7**, 1970036.

Li, Z., L. Liu, C. Gu, P. Ning, B. Xu, Z. Niu, and Y. Zhao, 2014, Appl. Phys. Lett. **104**, 101603.

Li, Z., B. Xu, C. Gu, P. Ning, L. Liu, Z. Niu, and Y. Zhao, 2014, Appl. Phys. Lett. **104**, 251601.

Liang, Y., H. Yu, H. C. Zhang, C. Yang, and T. J. Cui, 2015, Sci. Rep. **5**, 14853.

Liao, Z., A. I. Fernandez-Dominguez, J. Zhang, S. A. Maier, T. J. Cui, and Y. Luo, 2016, ACS Photonics **3**, 1768.

Liao, Z., S. Liu, H. F. Ma, C. Li, B. Jin, and T. J. Cui, 2016, Sci. Rep. **6**, 27596.

Liao, Z., G. Q. Luo, X. Y. Wu, B. G. Cai, B. C. Pan, and Y. J. Pan, 2020, Front. Phys. **8**, 53.

Liao, Z., Y. Luo, A. I. Fernández-Domínguez, X. Shen, S. A. Maier, and T. J. Cui, 2015, Sci. Rep. **5**, 9590.

Liao, Z., B. C. Pan, X. Shen, and T. J. Cui, 2014, Opt. Express **22**, 15710.

Liao, Z., J. Zhao, B. C. Pan, X. P. Shen, and T. J. Cui, 2014, J. Phys. D **47**, 315103.

Liao, Z., J. N. Zhou, G. Q. Luo, M. Wang, S. Sun, T. Zhou, H. F. Ma, T. J. Cui, and Y. Liu, 2020, Phys. Rev. Applied **13**, 054013.

Liu, G. L., M. X. He, Z. Tian, J. Y. Li, and J. Z. Liu, 2013, Appl. Opt. **52**, 5695.

Liu, L., Z. Li, C. Gu, B. Xu, P. Ning, C. Chen, J. Yan, Z. Niu, and Y. Zhao, 2015, Opt. Lett. **40**, 1810.

Liu, L., Z. Li, B. Xu, C. Gu, C. Chen, P. Ning, J. Yan, and X. Chen, 2015, AIP Adv. **5**, 027105.

Liu, L., Z. Li, B. Xu, C. Gu, X. Chen, H. Sun, Y. Zhou, Q. Qing, P. Shum, and Y. Luo, 2017, IEEE Trans. Microwave Theory Tech. **65**, 2008.

Liu, L., L. Wu, J. Zhang, Z. Li, B. Zhang, and Y. Luo, 2018, Adv. Sci. **5**, 1800661.

Liu, S., Z. Xu, X. Yin, and H. Zhao, 2020, Sci. Rep. **10**, 8469.

Liu, X., Y. Feng, K. Chen, B. Zhu, J. Zhao, and T. Jiang, 2014, Opt. Express **22**, 20107.

Liu, X., Y. Feng, B. Zhu, J. Zhao, and T. Jiang, 2016, Sci. Rep. **6**, 20448.

Liu, Y.-Q., L.-B. Kong, and P.-K. Liu, 2016, Opt. Commun. **370**, 13.

Liu, Y.-Q., J. Sun, L. Li, and H. Yin, 2020, AIP Adv. **10**, 045005.

Lockyear, M. J., A. P. Hibbins, and J. R. Sambles, 2009, Phys. Rev. Lett. **102**, 073901.

Lotito, V., U. Sennhauser, and C. Hafner, 2010, Opt. Express **18**, 8722.

Lu, H., X. T. Gan, D. Mao, and J. L. Zhao, 2017, Photonics Res. **5**, 162.

Luukkonen, O., C. Simovski, G. Granet, G. Goussetis, D. Lioubtchenko, A. V. Raisanen, and S. A. Tretyakov, 2008, IEEE Trans. Antennas Propag. **56**, 1624.

Ma, H. F., X. Shen, Q. Cheng, W. X. Jiang, and T. J. Cui, 2014, Laser Photonics Rev. **8**, 146.

Ma, Y. G., L. Lan, S. M. Zhong, and C. K. Ong, 2011, Opt. Express **19**, 21189.

Ma, Z. J., S. M. Hanham, P. A. Huidobro, Y. D. Gong, M. H. Hong, N. Klein, and S. A. Maier, 2017, APL Photonics **2**, 116102.

MacDonald, K. F., Z. L. Samson, M. I. Stockman, and N. I. Zheludev, 2009, Nat. Photonics **3**, 55.

Maier, S. A., 2007, *Plasmonics: Fundamentals and Applications* (Springer, New York).

Maier, S. A., and S. R. Andrews, 2006, Appl. Phys. Lett. **88**, 251120.

Maier, S. A., S. R. Andrews, L. Martín-Moreno, and F. J. García-Vidal, 2006, Phys. Rev. Lett. **97**, 176805.

Maier, S. A., P. G. Kik, H. A. Atwater, S. Meltzer, E. Harel, B. E. Koel, and A. A. Requicha, 2003, Nat. Mater. **2**, 229.

Mailloux, R., 2017, *Phased Array Antenna Handbook* (Artech House, Boston).

Martin-Cano, D., M. L. Nesterov, A. I. Fernandez-Dominguez, F. J. Garcia-Vidal, L. Martin-Moreno, and E. Moreno, 2010, Opt. Express **18**, 754.

Martín-Cano, D., O. Quevedo-Teruel, E. Moreno, L. Martín-Moreno, and F. J. García-Vidal, 2011, Opt. Lett. **36**, 4635.

Martín-Moreno, L., and F. J. García-Vidal, 2008, J. Phys. Condens. Matter **20**, 304214.

Martín-Moreno, L., F. J. García-Vidal, H. J. Lezec, A. Degiron, and T. W. Ebbesen, 2003, Phys. Rev. Lett. **90**, 167401.

Meng, Y., H. Xiang, R.-Y. Zhang, X. Wu, D. Han, C. T. Chan, and W. Wen, 2016, Opt. Lett. **41**, 3698.

Mercier, J.-F., M.-L. Cordero, S. Félix, A. Ourir, and A. Maurel, 2015, Proc. R. Soc. A **471**, 20150472.

Messina, R., A. Noto, B. Guizal, and M. Antezza, 2017, Phys. Rev. B **95**, 125404.

Mitchell, J., 2010, Sensors **10**, 7323.

Moreno, E., F. J. García-Vidal, S. G. Rodrigo, L. Martín-Moreno, and S. I. Bozhevolnyi, 2006, Opt. Lett. **31**, 3447.

Moreno, E., S. G. Rodrigo, S. I. Bozhevolnyi, L. Martín-Moreno, and F. J. García-Vidal, 2008, Phys. Rev. Lett. **100**, 023901.

Munk, B. A., 2000, *Frequency Selective Surfaces: Theory and Design* (Wiley, New York).

Navarro-Cia, M., M. Beruete, S. Agrafiotis, F. Falcone, M. Sorolla, and S. A. Maier, 2009, Opt. Express **17**, 18184.

Navarro-Cia, M., M. Beruete, M. Sorolla, and S. A. Maier, 2011, Plasmonics **6**, 295.

Nesterov, M. L., D. Martín-Cano, A. I. Fernández-Domínguez, E. Moreno, L. Martín-Moreno, and F. J. García-Vidal, 2010, Opt. Lett. **35**, 423.

Ng, B., S. M. Hanham, J. Wu, A. I. Fernandez-Dominguez, N. Klein, Y. F. Liew, M. B. H. Breese, M. Hong, and S. A. Maier, 2014, ACS Photonics **1**, 1059.

Ng, B., J. Wu, S. M. Hanham, A. I. Fernandez-Dominguez, N. Klein, Y. F. Liew, M. B. H. Breese, M. Hong, and S. A. Maier, 2013, Adv. Opt. Mater. **1**, 543.

Novikov, I. V., and A. A. Maradudin, 2002, Phys. Rev. B **66**, 035403.

Novotny, L., and B. Hecht, 2006, *Near-Field Optical Probes* (Cambridge University Press, Cambridge, England).

Novotny, L., and N. van Hulst, 2011, Nat. Photonics **5**, 83.

Nyein, H. Y. Y., *et al.*, 2018, ACS Sens. **3**, 944.

O'Hara, J., and R. D. Averitt, 2005, Opt. Express **13**, 6117.

Ooi, K., T. Okada, and K. Tanaka, 2011, Phys. Rev. B **84**, 115405.

Ordal, M. A., L. L. Long, R. J. Bell, S. E. Bell, R. R. Bell, R. W. Alexander, and C. A. Ward, 1983, Appl. Opt. **22**, 1099.

Otto, A., 1968, Z. Phys. **216**, 398.

Oulton, R. F., V. J. Sorger, T. Zentgraf, R.-M. Ma, C. Gladden, L. Dai, G. Bartal, and X. Zhang, 2009, Nature (London) **461**, 629.

Pacheco-Pena, V., N. Engheta, S. Kuznetsov, A. Gentselev, and M. Beruete, 2017, Phys. Rev. Applied **8**, 034036.

Padilla, P., L. Herran, A. Tamayo-Dominguez, J. Valenzuela-Valdes, and O. Quevedo-Teruel, 2018, IEEE Microwave Wireless Compon. Lett. **28**, 750.

Pan, B. C., and T. J. Cui, 2017, IEEE Trans. Antennas Propag. **65**, 5595.

Pan, B. C., Z. Liao, J. Zhao, and T. J. Cui, 2014, Opt. Express **22**, 13940.

Panaretos, A. H., and D. H. Werner, 2016, Opt. Express **24**, 2443.

Pandey, S., B. Gupta, and A. Nahata, 2013, Opt. Express **21**, 24422.

Pandit, N., R. K. Jaiswal, and N. P. Pathak, 2020, IEEE Sens. J. **20**, 10582.

Pendry, J. B., 2004, Science **306**, 1353.

Pendry, J. B., L. Martín-Moreno, and F. J. García-Vidal, 2004, Science **305**, 847.

Piefke, G., 1959, IRE Trans. Antennas Propag. **7**, 183.

Pile, D. F. P., and D. K. Gramotnev, 2004, Opt. Lett. **29**, 1069.

Pile, D. F. P., T. Ogawa, D. K. Gramotnev, T. Okamoto, M. Haraguchi, M. Fukui, and S. Matsuo, 2005, Appl. Phys. Lett. **87**, 061106.

Pitarke, J. M., V. M. Silkin, E. V. Chulkov, and P. M. Echenique, 2007, Rep. Prog. Phys. **70**, 1.

Plouin, J., E. Richalot, O. Picon, M. Carras, and A. de Rossi, 2006, Opt. Express **14**, 9982.

Popov, E., N. Bonod, and S. Enoch, 2007, Opt. Express **15**, 4224.

Popov, V., A. Díaz-Rubio, V. Asadchy, S. Tcvetkova, F. Boust, S. Tretyakov, and S. N. Burokur, 2019, Phys. Rev. B **100**, 125103.

Pors, A., E. Moreno, L. Martín-Moreno, J. B. Pendry, and F. J. García-Vidal, 2012, Phys. Rev. Lett. **108**, 223905.

Porto, J. A., F. J. García-Vidal, and J. B. Pendry, 1999, Phys. Rev. Lett. **83**, 2845.

Qi, C., S. Liao, and Q. Xue, 2018, Appl. Phys. Lett. **113**, 161902.

Qin, P., Y. Yang, M. Y. Musa, B. Zheng, Z. Wang, R. Hao, W. Yin, H. Chen, and E. Li, 2018, Adv. Sci. **5**, 1700487.

Qiu, M., 2005, Opt. Express **13**, 7583.

Quesada, R., D. Martin-Cano, F. J. Garcia-Vidal, and J. Bravo-Abad, 2014, Opt. Lett. **39**, 2990.

Raether, H., 1988a, *Surface Plasmons on Smooth and Rough Surfaces and on Gratings* (Springer-Verlag, New York).

Raether, H., 1988b, *Surface Plasmons*, Springer Tracts in Modern Physics Vol. III (Springer, Berlin).

Rappaport, T. S., S. Sun, R. Mayzus, H. Zhao, Y. Azar, K. Wang, G. N. Wong, J. K. Schulz, M. Samimi, and F. Gutierrez, 2013, IEEE Access **1**, 335.

Rappaport, T. S., Y. Xing, O. Kanhere, S. Ju, A. Madanayake, S. Mandal, A. Alkhateeb, and G. C. Trichopoulos, 2019, IEEE Access **7**, 78729.

Ritchie, R. H., 1957, Phys. Rev. **106**, 874.

Rodrigo, D., O. Limaj, D. Janner, D. Etezadi, F. Javier, Garcia de Abajo, V. Pruneri, and H. Altug, 2015, Science **349**, 165.

Ruan, Z. C., and M. Qiu, 2007, Appl. Phys. Lett. **90**, 201906.

Rüting, F., A. I. Fernández-Domínguez, L. Martín-Moreno, and F. J. García-Vidal, 2012, Phys. Rev. B **86**, 075437.

Saad, M., M. Bennis, and M. Chen, 2020, IEEE Netw. **34**, 134.

Sakai, O., and K. Tachibana, 2007, IEEE Trans. Plasma Sci. **35**, 1267.

Shao, R. L., Y. J. Zhou, and L. Yang, 2018, Appl. Opt. **57**, 8472.

Shen, J. T., P. B. Catrysse, and S. Fan, 2005, Phys. Rev. Lett. **94**, 197401.

Shen, L., X. Chen, X. Zhang, and K. Agarwal, 2011, Plasmonics **6**, 301.

Shen, L., X. Chen, Y. Zhong, and K. Agarwal, 2008, Phys. Rev. B **77**, 075408.

Shen, X., and T. J. Cui, 2013, Appl. Phys. Lett. **102**, 211909.

Shen, X., and T. J. Cui, 2014, Laser Photonics Rev. **8**, 137.

Shen, X. P., T. J. Cui, D. Martin-Cano, and F. J. Garcia-Vidal, 2013, Proc. Natl. Acad. Sci. U.S.A. **110**, 40.

Shin, Y.-M., L. R. Barnett, and N. C. Luhmann, 2008, Appl. Phys. Lett. **93**, 221504.

Sievenpiper, D., Lijun Zhang, R. F. J. Broas, N. G. Alexopolous, and E. Yablonovitch, 1999, IEEE Trans. Microwave Theory Tech. **47**, 2059.

Song, K., and P. Mazumder, 2012, Photonics Nanostructures Fundam. Appl. **10**, 674.

Sorger, V. J., R. F. Oulton, R. M. Ma, and X. Zhang, 2012, MRS Bull. **37**, 728.

Stone, E. K., and E. Hendry, 2011, Phys. Rev. B **84**, 035418.

Sun, S., Q. He, S. Xiao, X. Qin, X. Li, and L. Zhou, 2012, Nat. Mater. **11**, 426.

Sun, W., Q. He, S. Sun, and L. Zhou, 2016, Light Sci. Appl. **5**, e16003.

Tabata, H., 2015, IEEE Trans. Terahertz Sci. Technol. **5**, 1146.

Talebi, N., and M. Shahabadi, 2010, J. Phys. D **43**, 135302.

Tang, H.-H., T.-J. Ma, and P.-K. Liu, 2016, Appl. Phys. Lett. **108**, 191903.

Tian, L., Z. Zhang, J. Liu, K. Zhou, Y. Gao, and S. Liu, 2016, Opt. Express **24**, 28693.

Tian, X., P. M. Lee, Y. J. Tan, T. L. Y. Wu, H. Yao, M. Zhang, Z. Li, K. A. Ng, B. C. K. Tee, and J. S. Ho, 2019, Nat. Electron. **2**, 243.

Ulrich, R., and M. Tacke, 1973, Appl. Phys. Lett. **22**, 251.

Ummethala, S., *et al.*, 2019, Nat. Photonics **13**, 519.

Wang, F. M., H. Liu, T. Li, S. M. Wang, S. N. Zhu, J. Zhu, and W. Cao, 2007, Appl. Phys. Lett. **91**, 133107.

Wang, H. L., H. B. Li, Y. Wang, S. P. Xu, and W. Q. Xu, 2016, Nanoscale **8**, 4650.

Wang, K., and D. M. Mittleman, 2004, Nature (London) **432**, 376.

Wang, M., H. F. Ma, W. X. Tang, H. C. Zhang, Z. X. Wang, and T. J. Cui, 2019, Adv. Mater. Technol. **4**, 1800603.

Williams, C. R., S. R. Andrews, S. A. Maier, A. I. Fernández-Domínguez, L. Martín-Moreno, and F. J. García-Vidal, 2008, Nat. Photonics **2**, 175.

Williams, C. R., M. Misra, S. R. Andrews, S. A. Maier, S. Carretero-Palacios, S. G. Rodrigo, F. J. Garcia-Vidal, and L. Martin-Moreno, 2010, Appl. Phys. Lett. **96**, 011101.

Wood, J. J., L. A. Tomlinson, O. Hess, S. A. Maier, and A. I. Fernández-Domínguez, 2012, Phys. Rev. B **85**, 075441.

Wu, J. J., C. Wu, D. J. Hou, K. Liu, and T. Yang, 2015, IEEE Photonics J. **7**, 4800208.

Wu, J.-J., T.-J. Yang, and L. F. Shen, 2009, J. Electromagn. Waves Appl. **23**, 11.

Wu, J. Jei, C. Jang Wu, J. Qi Shen, D. J. Hou, and W. Chen Lo, 2015, Sci. Rep. **5**, 14461.

Wu, Y., M. Li, G. Yan, L. Deng, Y. Liu, and Z. Ghassemlooy, 2016, AIP Adv. **6**, 105110.

Xiang, H., Y. Meng, Q. Zhang, F. F. Qin, J. J. Xiao, D. Han, and W. Wen, 2015, Opt. Commun. **356**, 59.

Xiao, B., R. Sun, J. He, K. Qin, S. Kong, J. Chen, and X. Wang, 2015, IEEE Photonics Technol. Lett. **27**, 2190.

Xu, J., H. C. Zhang, W. Tang, J. Guo, C. Qian, and W. Li, 2016, Appl. Phys. Lett. **108**, 191906.

Xu, J. J., X. Jiang, H. C. Zhang, J. Wang, S. Qu, and T. J. Cui, 2017, Appl. Phys. Lett. **110**, 021118.

Xu, J. J., H. C. Zhang, Q. Zhang, and T. J. Cui, 2015, Appl. Phys. Lett. **106**, 021102.

Xu, Y., J. Zhang, and G. Song, 2013, IEEE Photonics Technol. Lett. **25**, 410.

Yan, X. T., W. Tang, J. F. Liu, W. Wang, X. X. Gao, and T. J. Cui, 2021, Adv. Photonics **3**, 026001.

Yang, B. J., Y. J. Zhou, and Q. X. Xiao, 2015, Opt. Express **23**, 21434.

Yang, Y., H. Chen, S. Xiao, N. A. Mortensen, and J. Zhang, 2015, Opt. Express **23**, 19074.

Yang, Y., *et al.*, 2017, NPG Asia Mater. **9**, e428.

Yao, H.-Z., and S. Zhong, 2015, Opt. Commun. **354**, 401.

Yin, J. Y., D. Bao, J. Ren, H. C. Zhang, B. C. Pan, Y. Fan, and T. J. Cui, 2017, IEEE Antennas Wireless Propag. Lett. **16**, 597.

Yin, J. Y., J. Ren, H. C. Zhang, B. C. Pan, and T. J. Cui, 2015, Sci. Rep. **5**, 8165.

Yin, J. Y., J. Ren, L. Zhang, H. Li, and T. J. Cui, 2018, Laser Photonics Rev. **12**, 1600316.

Yin, J. Y., J. Ren, Q. Zhang, H. C. Zhang, Y. Q. Liu, Y. B. Li, X. Wan, and T. J. Cui, 2016, IEEE Trans. Antennas Propag. **64**, 5181.

Yu, H., C. Wang, F. Y. Meng, J. G. Liang, H. S. Kashan, K. K. Adhikari, L. Wang, E. S. Kim, and N. Y. Kim, 2020, Sens. Actuators B **304**, 127138.

Yu, N., Q. J. Wang, M. A. Kats, J. A. Fan, S. P. Khanna, L. Li, A. G. Davies, E. H. Linfield, and F. Capasso, 2010, Nat. Mater. **9**, 730.

Yu, Z., Z. Gao, Z. Song, and Z. Wang, 2014, Appl. Opt. **53**, 1118.

Yuan, M., Y. Lu, Y. Zhang, Z. Zhang, Y. Li, H. Liu, X. Zhang, J. Han, and W. Zhang, 2020, Opt. Express **28**, 1987.

Zayats, A. V., I. I. Smolyaninov, and A. A. Maradudin, 2005, Phys. Rep. **408**, 131.

Zenneck, J., 1907, Ann. Phys. (Berlin) **328**, 846.

Zhang, A. Q., W. B. Lu, Z. G. Liu, and Y. Li, 2021, IEEE Trans. Antennas Propag. **69**, 2142.

Zhang, H., T. Cui, Q. Zhang, Y. Fan, and X. Fu, 2015, ACS Photonics **2**, 1333.

Zhang, H. C., T. J. Cui, Y. Luo, J. Zhang, J. Xu, P. H. He, and L. P. Zhang, 2020, Natl. Sci. Rev. **7**, 261.

Zhang, H. C., Y. F. Fan, J. Guo, X. J. Fu, and T. J. Cui, 2016, ACS Photonics **3**, 139.

Zhang, H. C., P. H. He, X. X. Gao, W. X. Tang, and T. J. Cui, 2018, J. Phys. Condens. Matter **30**, 134004.

Zhang, H. C., S. Liu, X. P. Shen, L. H. Chen, L. M. Li, and T. J. Cui, 2015, Laser Photonics Rev. **9**, 83.

Zhang, H. C., L. P. Zhang, P. H. He, J. Xu, C. Qian, F. J. Garcia-Vidal, and T. J. Cui, 2020, Light Sci. Appl. **9**, 1.

Zhang, J., L. Cai, W. Bai, Y. Xu, and G. Song, 2009, J. Appl. Phys. **106**, 103715.

Zhang, J., Z. Liao, Y. Luo, X. Shen, S. A. Maier, and T. J. Cui, 2017, Laser Photonics Rev. **11**, 1600191.

Zhang, J., J.-Y. Ou, N. Papasimakis, Y. Chen, K. F. MacDonald, and N. I. Zheludev, 2011, Opt. Express **19**, 23279.

Zhang, L., H. Zhang, M. Tang, P. He, L. Niu, L. Liu, J. Lu, W. Tang, J. Mao, and T. Cui, 2020, Sci. China Inf. Sci. **63**, 202302.

Zhang, Q., H. C. Zhang, W. Han, and T. J. Cui, 2015, Sci. Rep. **5**, 16531.

Zhang, Q., H. C. Zhang, J. Y. Yin, B. Pan, and T. J. Cui, 2016, Sci. Rep. **6**, 28256.

Zhang, Q. L., and C. H. Chan, 2020, IEEE Trans. Circuits Syst. II **67**, 3038.

Zhang, W., L. Sun, F. Lin, G. Zhu, and D. Lu, 2016, Microwave Opt. Technol. Lett. **58**, 261.

Zhang, W., G. Zhu, L. Sun, and F. Lin, 2015, Appl. Phys. Lett. **106**, 021104.

Zhang, X. F., L. F. Shen, and L. X. Ran, 2009, J. Appl. Phys. **105**, 013704.

Zhang, X. R., W. X. Tang, H. C. Zhang, J. Xu, G. D. Bai, J. F. Liu, and T. J. Cui, 2018, Adv. Mater. Technol. **3**, 1800046.

Zhang, Y., Y. Xu, C. Tian, Q. Xu, X. Zhang, Y. Li, X. Zhang, J. Han, and W. Zhang, 2018, Photonics Res. **6**, 18.

Zhao, W., O. M. Eldaiki, R. Yang, and Z. Lu, 2010, Opt. Express **18**, 21498.

Zhou, L., and C. T. Chan, 2004, Appl. Phys. Lett. **84**, 1444.

Zhou, S.-Y., S.-W. Wong, J.-Y. Lin, L. Zhu, Y. He, and Z.-H. Tu, 2019, IEEE Microwave Wireless Compon. Lett. **29**, 98.

Zhou, Y. J., and T. J. Cui, 2011, Appl. Phys. Lett. **98**, 221901.

Zhou, Y. J., Q. Jiang, and T. J. Cui, 2011, Appl. Phys. Lett. **99**, 111904.

Zhou, Y. J., Y. L. Qian, H. Z. Zhao, and T. J. Cui, 2020, Adv. Mater. Technol. **5**, 1900767.

Zhou, Y. J., Q. X. Xiao, and B. Jia Yang, 2015, Sci. Rep. **5**, 14189.

Zhou, Y. Jin, Q. Jiang, and T. Jun Cui, 2011, Appl. Phys. Lett. **99**, 111904.

Zhu, W., A. Agrawal, A. Cui, G. Kumar, and A. Nahata, 2011, IEEE J. Sel. Top. Quantum Electron. **17**, 146.

Zhu, W., A. Agrawal, and A. Nahata, 2008, Opt. Express **16**, 6216.